NASA TECHNICAL NOTE

NASA TN D-6028

NASA TN D-6028

HEAT-TRANSFER RATE AND PRESSURE MEASUREMENTS OBTAINED DURING APOLLO ORBITAL ENTRIES

by Dorothy B. Lee, John J. Bertin, and Winston D. Goodrich

Manned Spacecraft Center
Houston, Texas 77058

NATIONAL AERONAUTICS AND SPACE ADMINISTRATION • WASHINGTON, D. C. • OCTOBER 1970

1. REPORT NO.	2. GOVERNMENT ACCESSION NO.	3. RECIPIENT'S CATALOG NO.
NASA TN D-6028		

4. TITLE AND SUBTITLE	5. REPORT DATE
HEAT-TRANSFER RATE AND PRESSURE MEASUREMENTS OBTAINED DURING APOLLO ORBITAL ENTRIES	October 1970
	6. PERFORMING ORGANIZATION CODE
7. AUTHOR(S)	8. PERFORMING ORGANIZATION REPORT NO.
Dorothy B. Lee, John J. Bertin, and Winston D. Goodrich, MSC	MSC S-159
9. PERFORMING ORGANIZATION NAME AND ADDRESS	10. WORK UNIT NO.
Manned Spacecraft Center Houston, Texas 77058	914-11-20-10-72
	11. CONTRACT OR GRANT NO.
12. SPONSORING AGENCY NAME AND ADDRESS	13. REPORT TYPE AND PERIOD COVERED
National Aeronautics and Space Administration Washington, D.C. 20546	Technical Note
	14. SPONSORING AGENCY CODE

15. SUPPLEMENTARY NOTES

16. ABSTRACT

Measurements of local pressures and heating rates were made on the Apollo command module during entry from orbital velocities at Mach numbers from 28.6 to 11.5 on Apollo mission 1 and from 31.2 to 2.2 on Apollo mission 3. Flight pressure measurements were found to compare well with wind-tunnel results. Comparisons showed that laminar and turbulent heat-transfer theories augmented by wind-tunnel data can be used to predict the heating rates to the conical section of the spacecraft. Analysis of the heat-transfer-rate measurements indicated that transition to turbulent flow occurred on the conical section at local Reynolds numbers between 20 000 and 102 000, based on distance from the stagnation point. No valid heat-transfer data were obtained on the blunt entry face.

17. KEY WORDS (SUPPLIED BY AUTHOR)	18. DISTRIBUTION STATEMENT
*Heat Transfer Rate *Apollo Flight Data *Aerothermodynamics	Unclassified - unlimited

19. SECURITY CLASSIFICATION (THIS REPORT)	20. SECURITY CLASSIFICATION (THIS PAGE)	21. NO. OF PAGES	22. PRICE *
None	None	90	$3.00

*For sale by the Clearinghouse for Federal Scientific and Technical Information
Springfield, Virginia 22151

CONTENTS

TABLE

FIGURES

HEAT-TRANSFER RATE AND PRESSURE MEASUREMENTS OBTAINED DURING APOLLO ORBITAL ENTRIES

By Dorothy B. Lee, John J. Bertin,
and Winston D. Goodrich
Manned Spacecraft Center

SUMMARY

Measurements of local pressures and heating rates were made on the Apollo command module during entry from orbital velocities at Mach numbers from 28.6 to 11.5 on Apollo mission 1 and from 31.2 to 2.2 on Apollo mission 3. Flight pressure measurements compared well with wind-tunnel results. Comparisons showed that laminar and turbulent heat-transfer theories augmented by wind-tunnel data can be used to predict the heating to the conical section of the spacecraft. Analysis of the heat-transfer-rate measurements indicated that transition to turbulent flow occurred on the conical section at local Reynolds numbers between 20 000 and 102 000, based on distance from the stagnation point. No valid heat-transfer data were obtained on the blunt entry face.

INTRODUCTION

The design of the thermal protection system for the Apollo command module was based on theory augmented by wind-tunnel data. Final qualification of the system to withstand entry from orbital missions required flight tests of the command module. During the entry portion of the tests, local pressure and heat-transfer measurements were obtained on the spacecraft. The trajectories for the flight tests were so chosen as to subject the vehicles to a high heating-rate environment and to a high heat-load entry. The first flight test, Apollo mission 1, was conducted with spacecraft 009 on the Saturn IB launch vehicle. The spacecraft was launched from Cape Kennedy, Florida, on February 26, 1966. After a flight of approximately 37 minutes, the command module landed near Ascension Island, and recovery was achieved approximately 3 hours later. The second flight test was conducted with spacecraft 011 on Apollo mission 3. This high heat-load test was launched with the Saturn IB vehicle on August 25, 1966, and later recovered in the Pacific Ocean near Wake Island.

Measurements of local pressure and heating rates were obtained with pressure transducers and surface-mounted calorimeters installed on the command module. Data were obtained at free-stream relative velocities between 25 300 and 12 000 ft/sec on spacecraft 009 and between 27 300 and 2080 ft/sec on spacecraft 011. Histories of the measured pressures and heating rates compared with theoretical predictions and with

wind-tunnel results are presented in this report. Data from some of the wind-tunnel tests are given in references 1 to 6.

SYMBOLS

h	enthalpy, Btu/lb
M	Mach number
Pr	Prandtl number
p	pressure, psia
p_t	total pressure behind normal shock, psia
$\dot{q}$	heating rate, Btu/ft^2-sec
$\dot{q}_{t, \alpha=0}$	stagnation-point heating rate at zero angle of attack, Btu/ft^2-sec
R	command module maximum radius measured from the X_c-axis, 6.417 ft
$R_{\ell, x}$	local Reynolds number based on distance from flight stagnation point
S	distance measured from center of aft compartment, ft
t	time, sec
V	velocity, ft/sec
X_c, Y_c, Z_c	command module body coordinates, in.
x	distance measured from flight stagnation point, ft
α	angle of attack, deg
θ	angle about the command module X_c-axis, deg
μ	viscosity, lb/ft-sec
ρ	density, lb/ft^3

Subscripts:

aw	adiabatic wall
CW	cold wall
D	diameter
fp	flat plate
lam	laminar
turb	turbulent
WB	with blowing
w	wall
ℓ	local
∞	free stream

SPACECRAFT CONFIGURATION AND FLIGHT TEST

Entry Vehicle

The general configuration of the Apollo command module is shown in figure 1. The heat shield or thermal protection system, which covers the entire vehicle, is divided into three parts: the aft compartment, the crew compartment, and the forward compartment (fig. 1(a)). The aft compartment is a segment of a sphere with a radius of curvature of 184.8 inches. A toroidal section with a 7.7-inch radius forms the fairing between the spherical segment and the crew compartment. As shown in figure 1(b), the crew compartment extends from the toroid-conical tangency point at X_c = 23.2 inches to X_c = 81 inches. The forward compartment extends from X_c = 81 inches to X_c = 133.5 inches and is blunted to a 9.1-inch radius. The maximum body diameter of the command module is 154 inches and the axial length is 133.5 inches.

Instrumentation

Pressure transducers and surface-mounted calorimeters were installed on the command module to measure the local pressures and the heat-transfer rates on the vehicle. The locations and ranges of these sensors, which were the same for both spacecraft, are given in table I and are shown in figure 1(c). Sensors that did not operate or that gave questionable data are indicated by solid symbols in figure 1(c) for spacecraft 009 and in figure 1(d) for spacecraft 011.

Two types of calorimeters were used to measure heating rates on the spacecraft. Asymptotic calorimeters, designed to measure heating rates less than 50 Btu/ft^2-sec, were located on the conical section. The design of these instruments is shown schematically in figure 2(a) and the principle of operation is discussed in reference 7. High-range slug calorimeters, developed specifically for the Apollo Program, were located on the aft compartment to measure heating rates greater than 50 Btu/ft^2-sec. These slug calorimeters consist of several graphite wafers that are stacked to allow continuous heating measurements during recession of the surrounding ablator. The detail of one such wafer is shown schematically in figure 2(b). The wafer temperature and the rate of change of temperature are used to determine the heat flux to the surface. The operation and design of these calorimeters are discussed in reference 8.

Flight measurements were recorded on magnetic tape on board the spacecraft. A malfunction occurred in the electrical power subsystem on spacecraft 009 that resulted in permanent loss of heating-rate data approximately 86 seconds after initiation of entry. Heating data were obtained for the entire entry time of spacecraft 011.

Entry Trajectory

The desired high-heating-rate entry was achieved with spacecraft 009 entering the atmosphere at a flight-path angle of -9.03° and at a velocity of 25 173 ft/sec measured relative to the earth. Initial entry conditions, assumed to occur at an altitude of 400 000 feet, correspond to 1565.6 seconds after launch. The histories of altitude and velocity for spacecraft 009 are given in figure 3(a), and the atmospheric density used in the data analysis is given in figure 3(b). The calculated Mach number and total pressure are shown in figure 3(c).

The high-heat-load entry was achieved with spacecraft 011 entering the atmosphere at a relatively shallow flight-path angle of -3.53° and at a velocity of 27 200 ft/sec measured relative to the earth. Initial entry conditions occurred at 4348 seconds after launch. The trajectory parameters and the ambient conditions during entry of spacecraft 011 are shown in figure 4.

RESULTS AND DISCUSSION

Flow Patterns of Spacecraft 009

Asymmetric flow patterns were observed on spacecraft 009 because of the rolled attitude of the vehicle. Accelerometer data showed that spacecraft 009 entered at an angle of attack of 19.7° to 21.3° until 1649 seconds after launch, when the vehicle began rolling rapidly. For an angle of attack of 20°, wind-tunnel tests indicated that the spacecraft stagnation point should be located approximately 50 inches from the center of the aft compartment on the +Z-coordinate axis at $\theta = 90°$ (fig. 1(c)). However, postflight examination of the streak pattern on the aft compartment of spacecraft 009 (fig. 5) revealed a rotation of approximately 10° in the flight pitch plane which may have been caused by a lateral offset position of the center of gravity. Thus, the stagnation point was presumed to be in the $+Z_c$ to $+Y_c$ quadrant at $\theta \approx 80°$.

The effect of the rolled attitude on the conic: ection of spacecraft 009 can be seen in figures 6(a) to 6(d). Examination of the char interface in the yaw plane (evident in figs. 6(a) and 6(d)) reveals the asymmetry of the char pattern on the spacecraft. A composite drawing from these photographs (fig. 7) illustrates the char pattern on the conical section. The shaded area represents the surface which was charred during entry. Because the forward compartment was jettisoned before parachute deployment and was not recovered intact, the region of charring is not defined for this compartment. As seen in figure 7, the char pattern is rotated approximately 11° toward the +Y-axis when measured at various points along the char interface. This angular displacement corresponded to the flight pitch plane at $\theta \approx 79°$, which is consistent with the flow patterns in figure 5.

In figure 7, the shaded areas on either side of the umbilical housing were found to consist mostly of scorched paint and not of charred ablator material. A photograph of this pattern is shown in figure 8.

Spacecraft 011 entered at an angle of attack of 18° and did not appear to have experienced off-nominal roll. The ablator on the conical section of spacecraft 011 was not charred since the flow was separated over the entire conical region because of the low angle-of-attack attitude during entry.

Pressure

Pressure distributions over the basic command module have been measured at various angles of attack in several wind-tunnel facilities. Selected data have been presented in reference 2 as the ratio of the measured pressure to the calculated total pressure behind a normal shock. Faired curves of these pressure ratios are shown in figure 9 for angles of attack of 18° and 20°. Estimates of flight pressures were made by using these ratios and normal-shock calculations of total pressure for actual flight conditions.

Spacecraft 009. - Flight-test data were obtained from 19 pressure transducers (10 on the aft heat shield and nine on the conical section) on spacecraft 009. Histories of the measured values are shown in figure 10. The measured pressures have not been corrected for possible zero shifts, although it is evident that such corrections are appropriate for several of the sensors. There is very good agreement between the flight measurements and the estimates based on the wind-tunnel data for the aft heat shield (figs. 10(a) to 10(j)).

The pressures on the conical section of spacecraft 009 (figs. 10(k) to 10(m)) were measured with 3-psia transducers (minimum range available in suitable flight-qualified sensors), although the maximum pressure was anticipated to be between 0.5 and 1.0 psia. As a result of the low magnitude of the measurements, the quantitative and qualitative analyses of the data are limited. The pressure history measured immediately downstream of the windward scimitar antenna is shown in figure 10(k). The irregular behavior of this pressure measurement suggests strong local influence of the scimitar antenna on the flow. In figure 11, which displays the flow pattern around the antenna, the sensor is indiscernible.

The pressure histories for most of the sensors on the toroid and conical sections (figs. 10(l) and 10(m)) are in reasonable agreement with wind-tunnel predictions if corrections for zero shift are considered.

The irregular drop in pressure that occurred at approximately 1635 seconds at each measurement location on spacecraft 009 coincides with a drop in signal strength noted on oscillograph records. Although full signal strength returned shortly after 1635 seconds, the signal faded again. As a result, the data obtained after 1660 seconds were considered questionable and were subsequently discarded.

The flight pressure measurements shown in figure 10 were corrected for the estimated zero shift and then divided by the maximum pressure measured at $S/R = 0.72$ in the stagnation region. The resultant pressure distribution is shown as bars in figure 12. The bars show the range of data in the Mach number interval $M = 21.9$ to 11.5 where the measured values were at least 50 percent of the full-scale reading. The flight measurements are compared with wind-tunnel data obtained at a Mach number of 10 (ref. 2) for angles of attack of 20° and 25°. The flight measurements fall between the two wind-tunnel curves, which differ most near the leeward corner. Although the difference in the wind-tunnel curves was as much as 20 percent, only a 5-percent difference resulted in the calculated Reynolds numbers based on local conditions.

Spacecraft 011. - Flight-test data were obtained from 10 of the 12 pressure transducers on the aft compartment of spacecraft 011 and from one transducer located on the toroid. No discernible pressure rise was detected and, in some cases, no data were obtained on the conical section until just before parachute deployment.

The maximum pressure was measured at $S/R = 0.775$, which is in the stagnation region. The excellent agreement between this measurement and the calculated total pressure is evident in figure 13. Pressure distributions for the pitch and yaw planes of spacecraft 011 are shown in figure 14. The flight data have been normalized by the maximum pressure measurement and compared with wind-tunnel distributions for the Apollo command module at 18° and 20° angles of attack. The spacecraft changed angle of attack during entry (ref. 9), and thus the two fairings are presented to illustrate the small angle-of-attack effect on the pressure distribution. The comparison of the flight data with the wind-tunnel pressure distribution is good considering the accuracy associated with these measurements. This accuracy was assumed to be ± 3 percent of full scale, which resulted in a p/p_t uncertainty as high as 0.20.

Heating Rates

Wind-tunnel heat-transfer-rate measurements obtained on the smooth-body configuration of the Apollo command module at various angles of attack are described in references 1 and 2. Figure 15 shows wind-tunnel data obtained at $\alpha = 18°$ and 20° referenced to the measured zero angle-of-attack stagnation-point value. These measured distributions were used with a stagnation-point theory (ref. 10) to predict the cold-wall laminar local heating rates over the surface of the command module during entry. Turbulent heating to the aft compartment, the toroid, and the leeward conical section

was estimated using the theory advanced by Van Driest in reference 11 where the ratio of turbulent to laminar heating is expressed as

$$\frac{\dot{q}_{turb}}{\dot{q}_{lam}} = 0.055\left(\frac{\rho_\ell V_\ell x}{\mu_\ell}\right)^{0.301} \tag{1}$$

Turbulent heating to the windward conical section was estimated with the flat-plate theory and expressed as

$$\dot{q}_{turb,\,fp} = \frac{0.030\rho_\ell V_\ell \left(h_{aw} - h_w\right)}{Pr^{2/3}\left(R_{\ell,x}\right)^{1/5}} \tag{2}$$

The local Reynolds number was calculated with the assumption of an isentropic expansion from the stagnation conditions behind the normal shock to the local pressure obtained from figure 9. For the predictions of flight heat-transfer rates, transition from laminar to turbulent flow was assumed to occur at a local Reynolds number of 150 000 in attached flow and at a local Reynolds number of 20 000 in separated flow.

Aft compartment heating rates. - Six of the high-range calorimeters located on the aft compartment of spacecraft 009 were operational, and temperatures of the outermost wafers were measured for approximately 54 seconds from the initial entry time. An attempt was made to deduce heat-transfer rates from these measured temperatures and from the thermal properties of the sensor. However, calibration tests showed that heat losses to subsequent wafers and surrounding material were so large that analysis was impossible when only the temperature of the top wafer was monitored. Therefore, no results from these sensors are presented.

Numerous malfunctions were observed in the wafer temperature measurements on spacecraft 011. No meaningful data were obtained because of thermocouple shorting and premature switching from each recording wafer.

Spacecraft 009 conical-section heating rates. - Histories of the heating rates measured with the asymptotic calorimeters on the conical section are shown in figure 16. Predictions of heating rates based on theory and on wind-tunnel data are included for comparison with the experimental flight data. The local Reynolds number is shown above the heating-rate history.

The heating-rate histories shown in figures 16(a) to 16(f) show an apparently irregular increase in heating between 1580 and 1595 seconds. All these sensors shared a common recording circuit. Because the increase did not occur for the two sensors (figs. 16(g) and 16(h)) that were connected to a different recording circuit, it is believed that an electrical disturbance in this circuit may have caused the irregular increase. Some of the sensors indicated significant heating rates before entry when the

heating rate is known to be low. Because these rates approached values near zero after the aforementioned irregularity, no corrections for zero shift were made. At the time of maximum heating (1635 seconds), the main electrical buses began to show transient excursions from nominal values. The excursions continued until approximately 1650 seconds, when an electrical short resulted in loss of data.

When the ablator is subjected to sufficiently high heating rates to cause charring, local mass injection or outgassing must be considered in the data analysis. A charring and ablation computer program, designated STAB II (ref. 12), was used to calculate the heat-transfer rates adjusted for blowing $\dot{q}_{WB}$. These adjusted data are compared with the flight data in figure 16. Where warranted, the data have been corrected for discontinuous mass injection as presented in reference 13 and for nonisothermal wall effects as discussed in reference 14. The corrections were 6 to 12 percent near the toroid and 2 to 4 percent near the apex. Although the scatter of the data prevents precise comparisons for most calorimeters, both flight measurements and theory show similar characteristics at most locations.

The heating analysis for the spacecraft conical section can be classified according to three areas: the windward and the toroid sections (both of which are in attached flow) and the leeward conical section (which is in separated flow). On the windward conical section (figs. 16(a) to 16(f)), the laminar cold-wall predictions adequately describe the flight data during the laminar portion of the flight. The flat-plate turbulent theory (eq. (2)) adjusted for local blowing overpredicts the measurements obtained near the scimitar antenna (figs. 16(a) and 16(b)) but is in excellent agreement with the data obtained farther downstream (fig. 16(d)). Transition was observed at a local Reynolds number as low as 40 000 in this attached-flow region. The low level of heating at the apex suggests that the flow is separated when the command module is at a 20° angle of attack.

The toroid is in a region of rapidly accelerating flow and experiences severe pressure and heating gradients. Histories of the measured heating rates for the toroid area are shown in figures 16(g) and 16(h). The slope change observed in the measurements is presumed to be caused by the onset of transition and corresponds to a local Reynolds number of approximately 30 000 at both locations. The temporary loss of data indicated in figure 16(h) occurred when the heating rates exceeded the sensor design limit of 10 Btu/ft^2-sec.

The leeward conical section, which was in separated flow, remained uncharred. Therefore, the cold-wall predictions shown in figures 16(i) to 16(p) were not adjusted for blowing. At all of the locations except the one near the apex (fig. 16(p)), the laminar predictions based on 2 percent of the stagnation-point theory adequately describe the flight data. Where the data exceed the laminar predictions, the turbulent theory (eq. (1)) is adequate for the separated-flow region. The flat-plate turbulent theory (eq. (2)), even when lowered by 60 percent to account for separated flow, yielded heating rates that were 3 to 4 times the measurements. Curves obtained from the two theories are shown in figure 16(i). Transition on the leeward conical section was observed to occur at local Reynolds numbers varying from 40 000 to 102 000. No transition was observed at some measurement stations even though local Reynolds numbers were as high as 270 000. The higher heating near the apex (fig. 16(p)) may be due to crossflow or wake effects.

Spacecraft 011 conical-section heating rates. - Histories of the heating rates measured on the conical section of spacecraft 011 are shown in figure 17. The low magnitude of the measurements at all locations suggests that the flow was separated over the entire conical section. The spacecraft entered at an angle of attack of 18°, which is consistent with the possibility that the windward side was at the threshold of flow attachment. The wind-tunnel data shown in figure 18 as a function of angle of attack illustrate the effect of separated and attached flow on the heating. The dashed line at 18° denotes the extent of measured separated flow as a function of angle of attack. The separated-flow laminar predictions of 3.5 and 4 percent of stagnation-point theory are in excellent agreement with the measurements on the windward conical section (figs. 17(a) to 17(f)) during the first heat pulse. The flat-plate turbulent theory adjusted for separated flow agrees closely with measured values during the second pulse. Transition was assumed to occur at a local Reynolds number of 20 000. The spacecraft changed angle of attack during entry, increasing from 18° to 20°, which may have caused the flow to attach to the windward conical section after the peak of the second heat pulse. A history of the total angle of attack obtained from the accelerometer data (ref. 9) is shown in figure 19.

The measured values shown in figure 17(g) were obtained on the windward side of the conical section. Although the wind-tunnel-based prediction of 3 percent of stagnation-point theory is twice the measured value during the first heat pulse, the wind-tunnel data are of the same magnitude as the flight data during the second heat pulse.

The measured values obtained on the toroid (figs. 17(h), 17(i), and 17(n)) indicate the flow remained laminar throughout the heating portion of the entry. The cold-wall laminar predictions agree very well with the flight data. The temporary loss of data noted in figure 17(i) occurred when the heating rates exceeded the sensor design limit of 3 Btu/ft^2-sec.

All of the leeward conical measurements, with the exception of the one near the apex (fig. 17(s)), fall below the predicted values based on 2 percent of stagnation-point theory. In general, the measurements were less than or equal to 1 percent of the stagnation-point theory during the first pulse. The turbulent theory of equation (1) adequately describes the heating rates that exceed the laminar theory. The flat-plate theory of equation (2) adjusted to account for separated flow was found to be conservative. The theoretical assessment of the leeward conical heating is illustrated in figure 20, which shows representative data from both spacecraft as a function of local Reynolds number. A transition Reynolds number criterion is not immediately discernible from figure 20. However, examination of the data for discrete locations reveals that transition could occur at local Reynolds numbers as low as 20 000 and as high as 52 000. The scatter in the data shown in figure 20 may be due to the use of the wetted-length Reynolds number when the separated-flow pattern obviously does not follow the spacecraft surface. Thus, such a Reynolds number length may be inappropriate.

Effects of reaction control system on heating. - The heating-rate spikes that can be observed in the leeward measurements on spacecraft 011 were found to correspond to the times of the reaction control subsystem (RCS) firings. During entry, the RCS performed several roll maneuvers to control and guide the spacecraft to a predetermined landing target. The momentary response of the asymptotic calorimeters on

spacecraft 011 showed heating rates as high as 5 times that measured between firings. The momentary increase amounted to only a 10-percent increase in the heat load. The control firings performed on spacecraft 009 during the heating portion of the entry were negligible.

CONCLUSIONS

Local pressure and heat-transfer measurements were obtained on the Apollo command module during entry from orbital velocities. Comparisons of the flight measurements with theoretical predictions and with wind-tunnel measurements yield the following conclusions.

1. Flight data verify that wind-tunnel measurements provide a good description of the pressure variations on the aft and conical section of the command module during entry.

2. Heating rates measured with asymptotic calorimeters on the conical section agreed with wind-tunnel measurements extrapolated on the basis of laminar theory.

3. Interpretation of heating rates measured in the charred regions of the ablator requires consideration of local blowing or mass injection.

4. The turbulent heating rates are described adequately by the flat-plate theory for the windward conical section and by Van Driest's theory for the leeward conical section.

5. The data suggest that the transition Reynolds number may be appreciably lower in attached-flow regions than the preflight predictions of 150 000.

6. The firings of the reaction control rocket engines located on the entry vehicle were found to raise the heating rates momentarily to as much as 5 times the no-firing condition; however, because the total firing times are short, the heat load was increased by only 10 percent.

Manned Spacecraft Center
National Aeronautics and Space Administration
Houston, Texas, July 3, 1970
914-11-20-10-72

REFERENCES

1. Bertin, John J.: Wind-Tunnel Heating Rates for the Apollo Spacecraft. NASA TM X-1033, 1965.

2. Bertin, John J.: The Effect of Protuberances, Cavities, and Angle of Attack on the Wind-Tunnel Pressure and Heat-Transfer Distribution for the Apollo Command Module. NASA TM X-1243, 1966.

3. Jones, Jim J.; and Moore, John A.: Shock-Tunnel Heat-Transfer Investigation on the Afterbody of an Apollo-Type Configuration at Angles of Attack up to 45° (U). NASA TM X-1042, 1964.

4. Jones, Robert A.: Experimental Investigation of the Overall Pressure Distribution, Flow Field, and Afterbody Heat-Transfer Distribution of an Apollo Reentry Configuration at a Mach Number of 8 (U). NASA TM X-813, 1963.

5. Jones, Robert A.: Measured Heat-Transfer and Pressure Distributions on the Apollo Face at a Mach Number of 8 and Estimates for Flight Conditions. NASA TM X-919, 1964.

6. Marvin, Joseph G.; and Kussoy, Marvin: Experimental Investigation of the Flow Field and Heat Transfer Over the Apollo-Capsule Afterbody at a Mach Number of 20 (U). NASA TM X-1032, 1965.

7. Grimaud, John E.; and Tillian, Donald J.: Heat Transfer Rate Measurement Techniques In Arc-Heated Facilities. Paper presented to ASME 88th Winter Annual Meeting and 2nd Energy Systems Exposition, Pittsburgh, Pa., Nov. 12-17, 1967.

8. Yanswitz, Herbert; and Beckman, Paul: A Heat-Flux Gage for Use on Recessive Surfaces. ISA Transactions, vol. 6, no. 3, July 1967, pp. 188-193.

9. Hillje, Ernest R.: Entry Flight Aerodynamics From Apollo Mission AS-202. NASA TN D-4185, 1967.

10. Detra, R. W.; Kemp, N. H.; and Riddell, F. R.: Addendum to "Heat Transfer to Satellite Vehicles Re-entering the Atmosphere." Jet Propulsion, vol. 27, no. 12, Dec. 1957, pp. 1256-1257.

11. Van Driest, E. R.: On Skin Friction and Heat Transfer Near the Stagnation Point. NAA Rep., AL-2267, Mar. 1, 1956.

12. Curry, Donald M.: An Analysis of a Charring Ablation Thermal Protection System. NASA TN D-3150, 1965.

13. Hearne, L. F.; Chin, J. H.; and Woodruff, L. W.: Study of Aerothermodynamic Phenomena Associated With Reentry of Manned Spacecraft. NASA CR-65368, May 1966.

14. Woodruff, L. W.; Hearne, L. F.; and Keliher, T. J.: Interpretation of Asymptotic Calorimeter Measurements. AIAA, vol. 5, no. 4, Apr. 1967, pp. 795-797.

TABLE I. - LOCATIONS AND RANGES OF PRESSURE SENSORS AND CALORIMETERS

(a) Aft compartment

Pressure sensor				Calorimeter		
Y_c, in.	Z_c, in.	Range, psia		Y_c, in.	Z_c, in.	Range, Btu/ft^2-sec
		Spacecraft 009	Spacecraft 011			
0	75	0 to 10	0 to 5	1.3	74.7	300
2.25	-71.8	0 to 10	0 to 3	4.75	-71.8	200
2.25	70.5	0 to 17.5	0 to 5	4.0	71.8	300
71.8	-.8	0 to 15	0 to 3	71.8	-3.25	200
0	58.4	0 to 17.5	0 to 5	4.75	58.4	300
0	54.4	0 to 17.5	0 to 5	-2.0	56.3	200
-2.1	35.2	0 to 17.5	0 to 5	4.0	33.3	250
0	-35.0	0 to 15	0 to 3	-2.7	-35.0	200
34.3	-2.1	0 to 15	0 to 5	39.0	4.6	200
-36.7	-3.8	0 to 15	0 to 5	-38.6	-5.7	200
6.0	-2.5	0 to 15	0 to 5	-.2	.6	250
42.4	45.9	0 to 10	0 to 5	41.1	44.4	300

TABLE I. - LOCATIONS AND RANGES OF PRESSURE SENSORS

AND CALORIMETERS - Concluded

(b) Conical section - Concluded

Pressure sensor			Calorimeter		
X_c, in.	θ, deg	Range, psia	X_c, in.	θ, deg	Range, Btu/ft^2-sec
26.5	91.8	0 to 3.0	26.5	93.7	100
45.5	88.1	0 to 3.0	45.5	85.3	50
62.3	93.4	0 to 3.0	64.8	92.0	50
78.9	118.2	0 to 3.0	78.9	115.0	50
110.0	95.8	0 to 3.0	114.0	83.4	50
25.3	136.1	0 to 3.0	25.3	138.0	50
19.4	271.6	0 to 3.0	19.4	270.0	10
82.6	219.8	0 to 3.0	88.0	182.9	25
19.4	177.0	0 to 3.0	19.4	178.5	25
25.3	223.5	0 to 3.0	25.3	225.5	10
78.9	187.9	0 to 3.0	78.9	191.3	25
37.5	215.3	0 to 3.0	40.0	215.3	10
78.9	263.9	0 to 3.0	78.9	267.8	25
114.0	275.0	0 to 3.0	114.0	265.0	25
45.5	226.0	0 to 3.0	51.7	229.8	10
59.0	142.8	0 to 3.0	61.5	142.8	25
35.0	176.5	0 to 3.0	35.0	178.6	25
57.4	177.6	0 to 3.0	60.0	177.5	25
70.5	271.9	0 to 3.0	70.5	276.4	25
133.0	Apex	0 to 3.0	133.0	Apex	25
58.0	232.0	0 to 3.0	58.0	234.0	25
27.1	253.0	0 to 7.0	27.1	253.0	25
32.6	253.0	0 to 7.0	32.6	253.0	50
32.6	253.0	0 to 7.0			

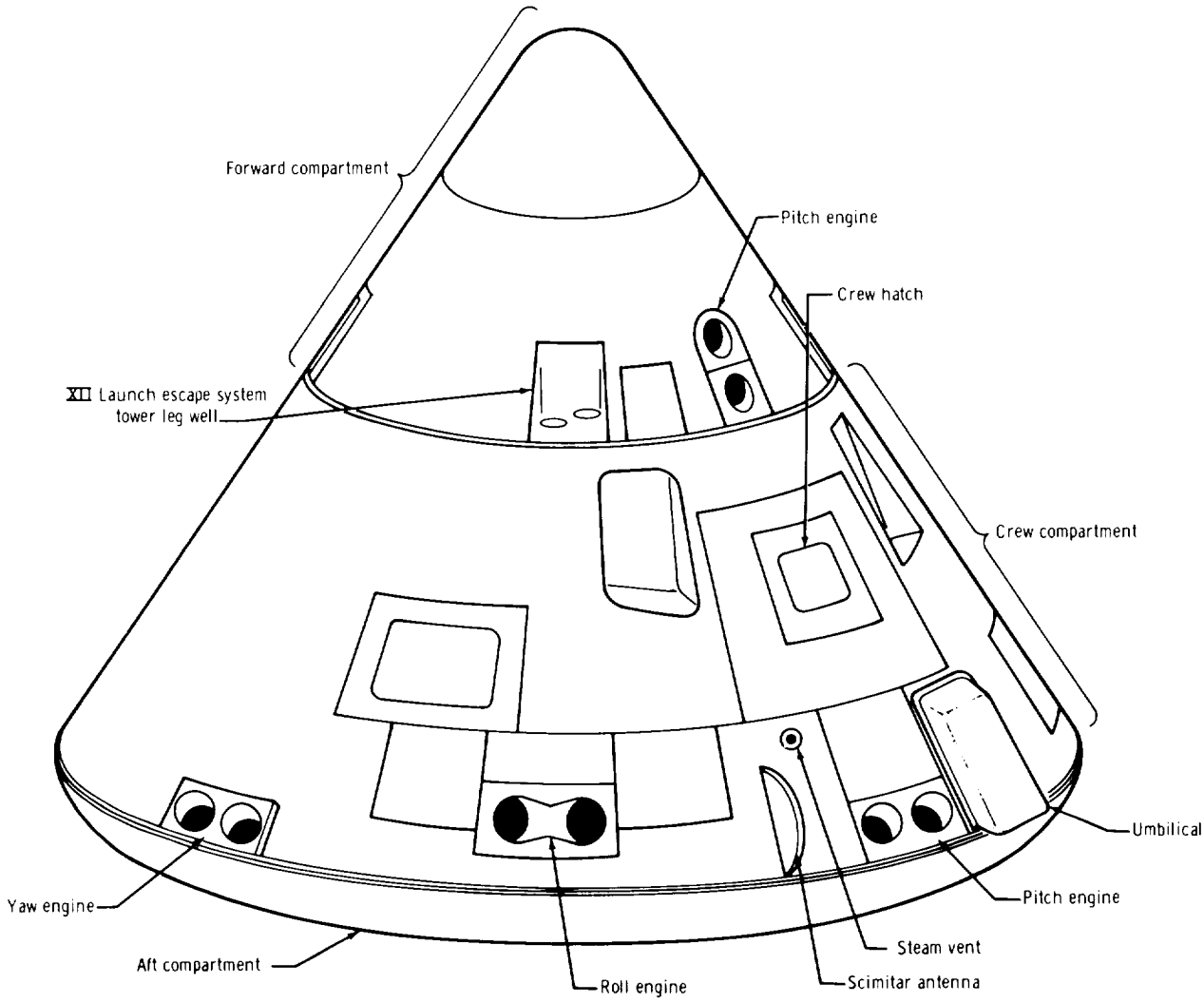

(a) Leeward view of the command module configuration.

Figure 1. - Apollo entry vehicle.

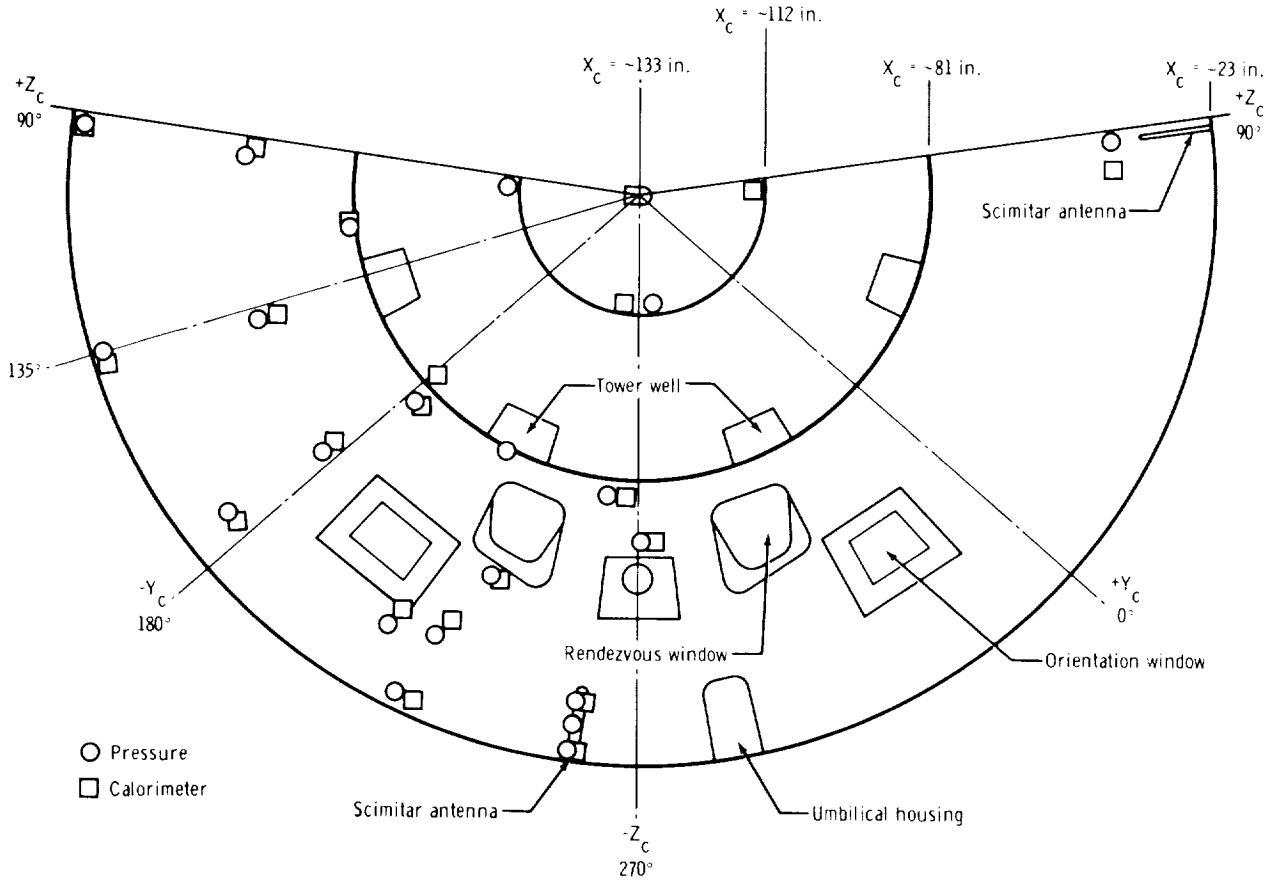

(b) Sketch of forward and crew compartments showing instrumentation location.

Figure 1. - Continued.

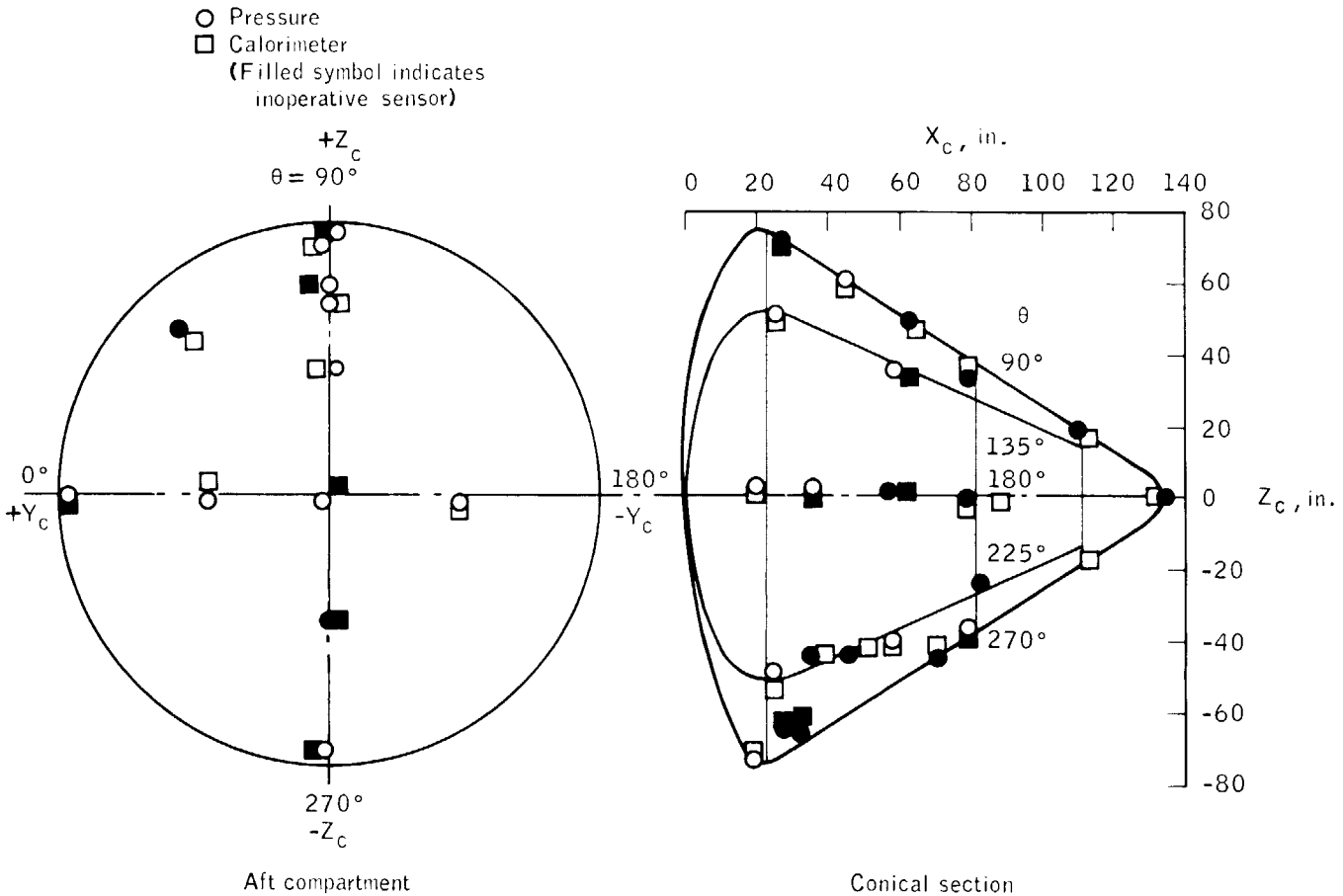

(c) Pressure sensor and calorimeter locations on the aft compartment and conical section of spacecraft 009.

Figure 1. - Continued.

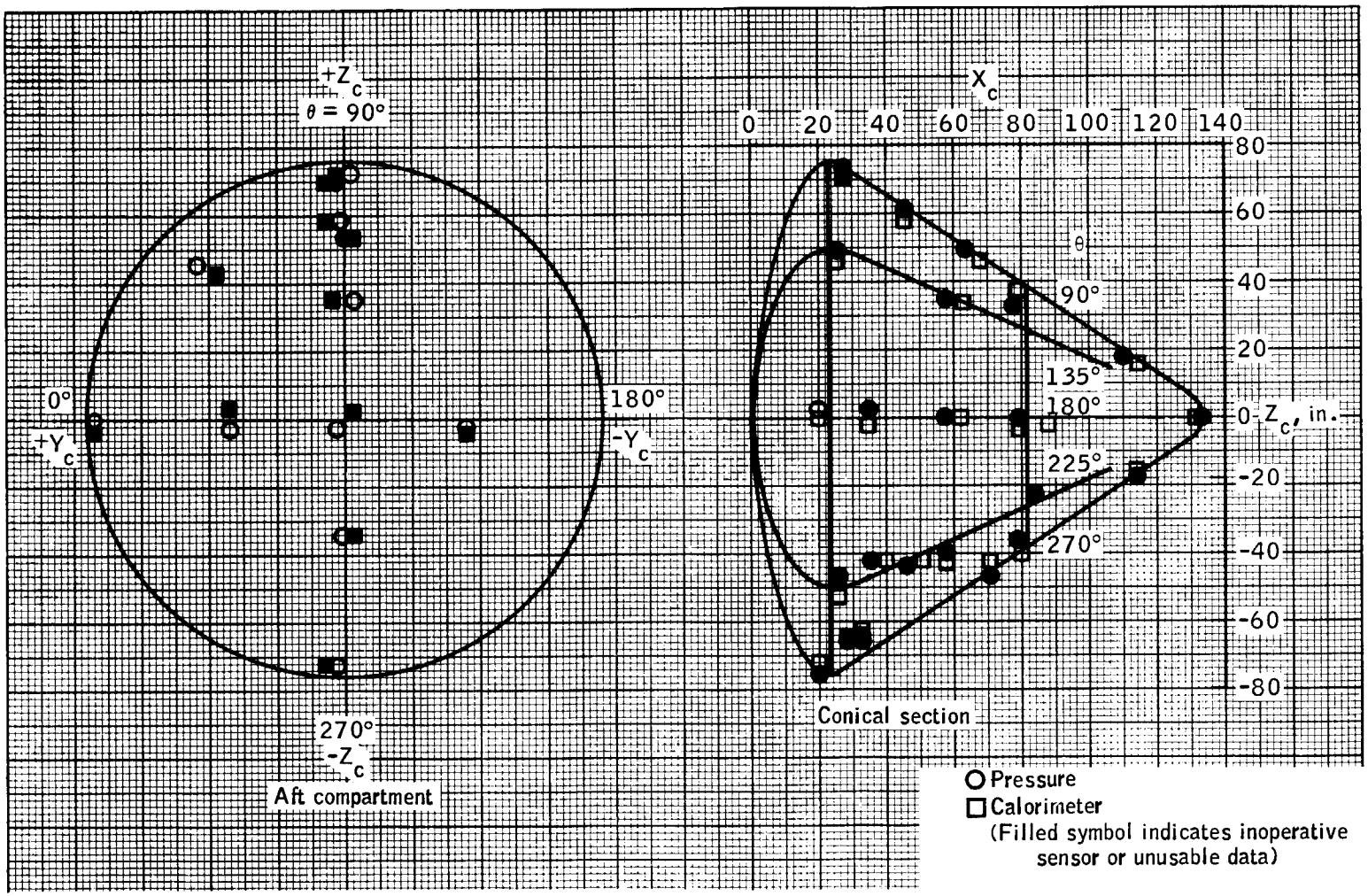

(d) Pressure sensor and calorimeter locations on the aft compartment and conical section of spacecraft 011.

Figure 1. - Concluded.

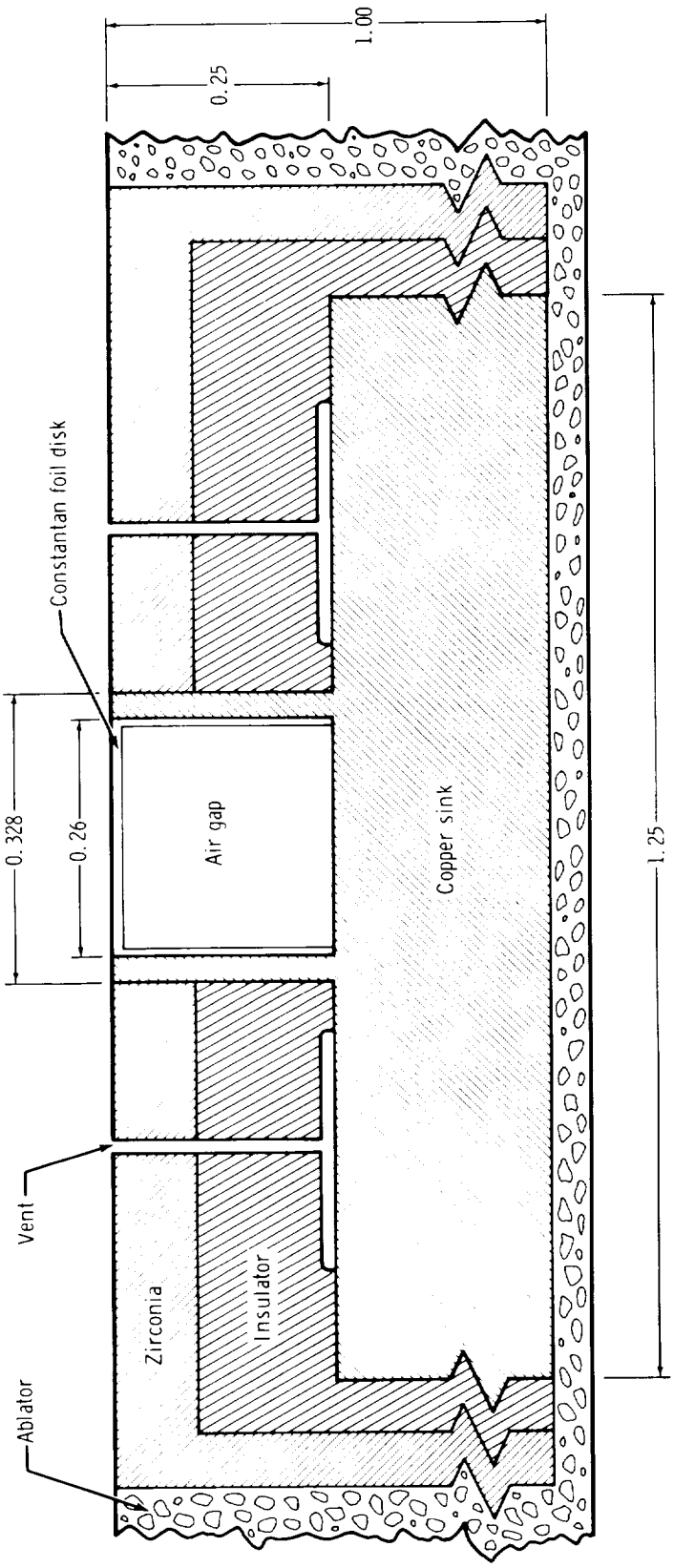

(a) Asymptotic calorimeter.

Figure 2. - Schematic of calorimeters on spacecraft 009 and 011. Dimensions are in inches.

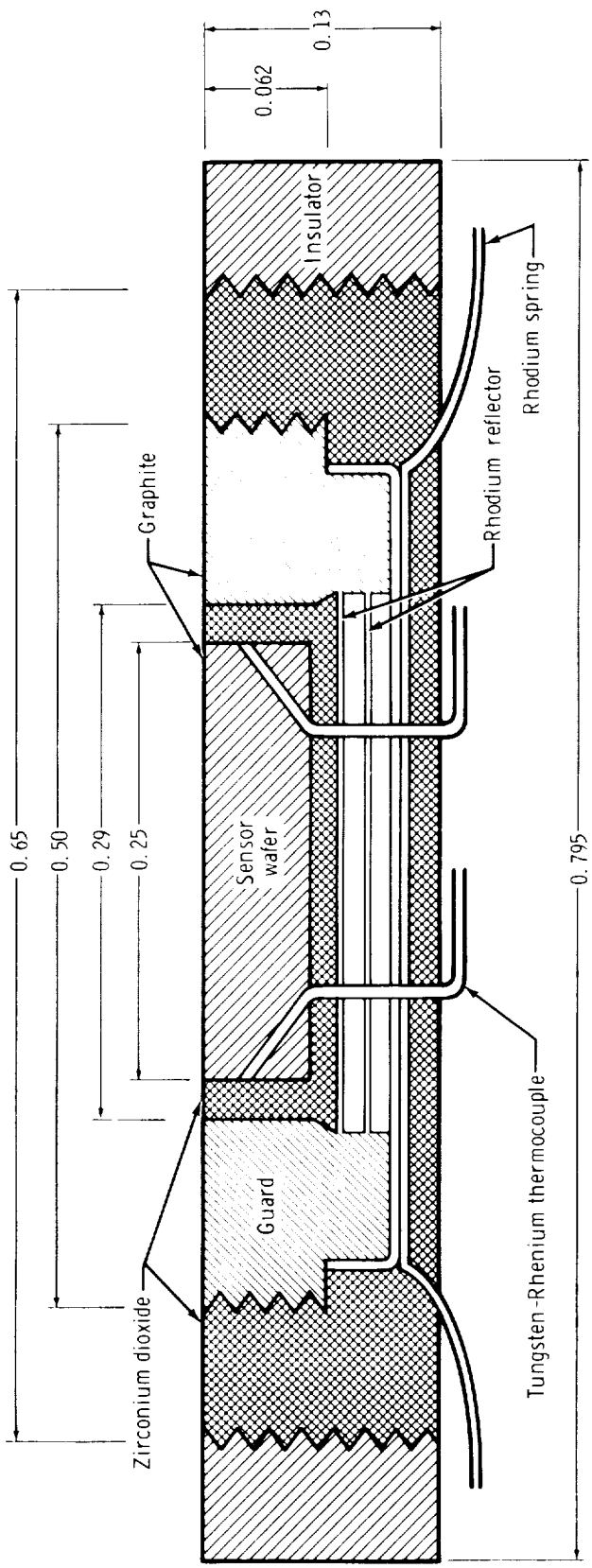

(b) High-range calorimeter wafer assembly.

Figure 2. - Concluded.

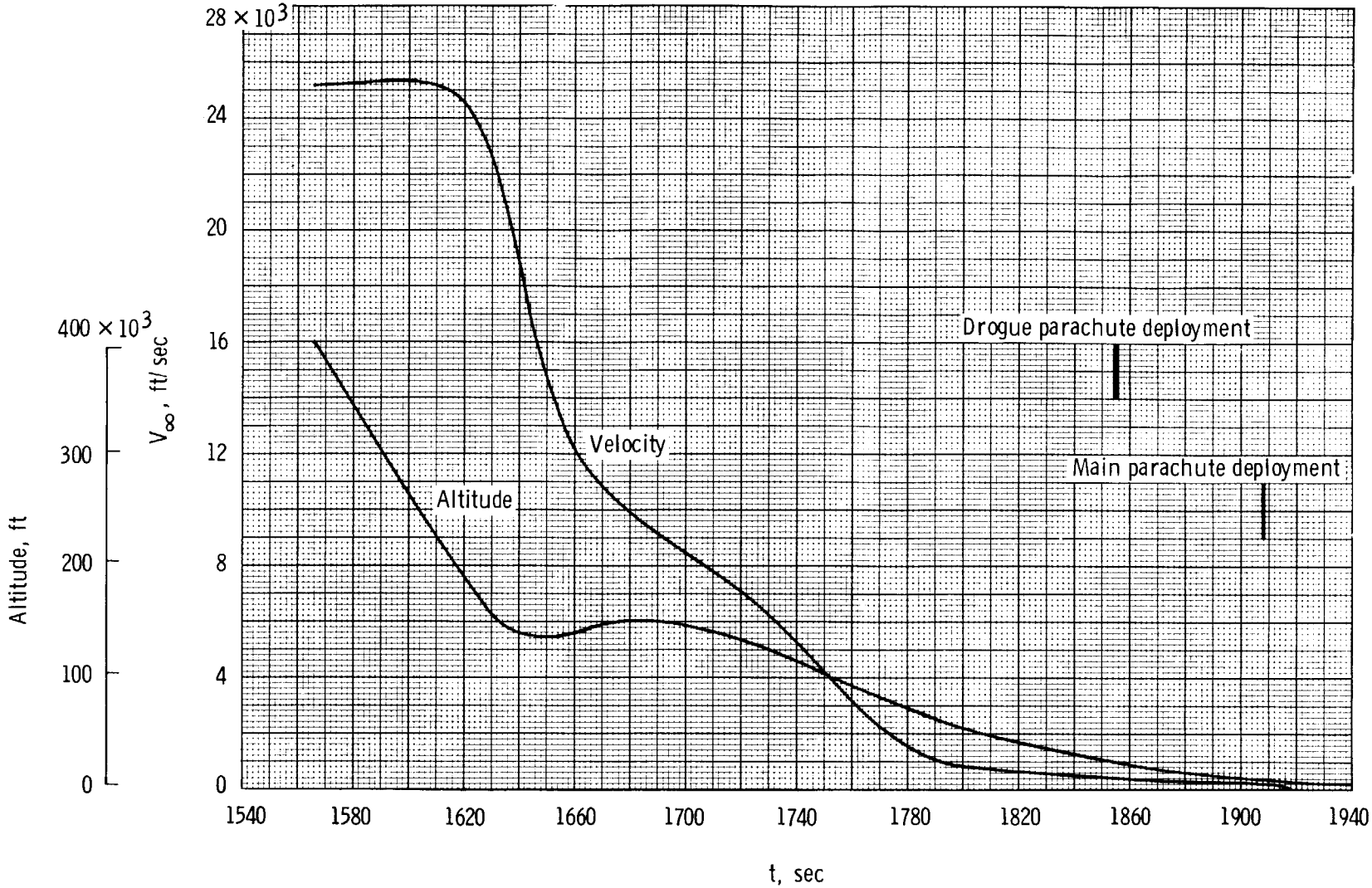

(a) Altitude and relative free-stream velocity.

Figure 3. - Entry conditions of spacecraft 009.

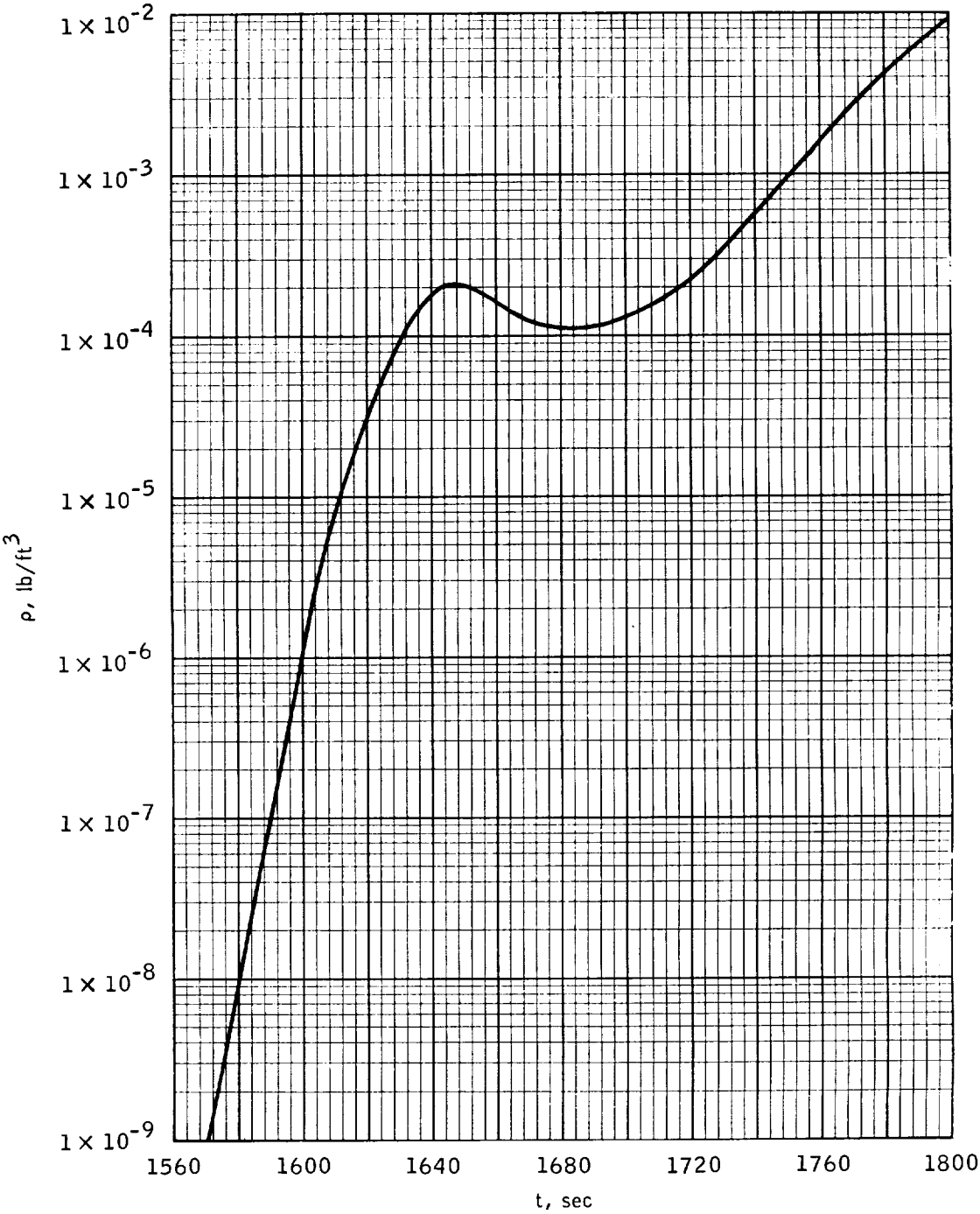

(b) Free-stream density.

Figure 3. - Continued.

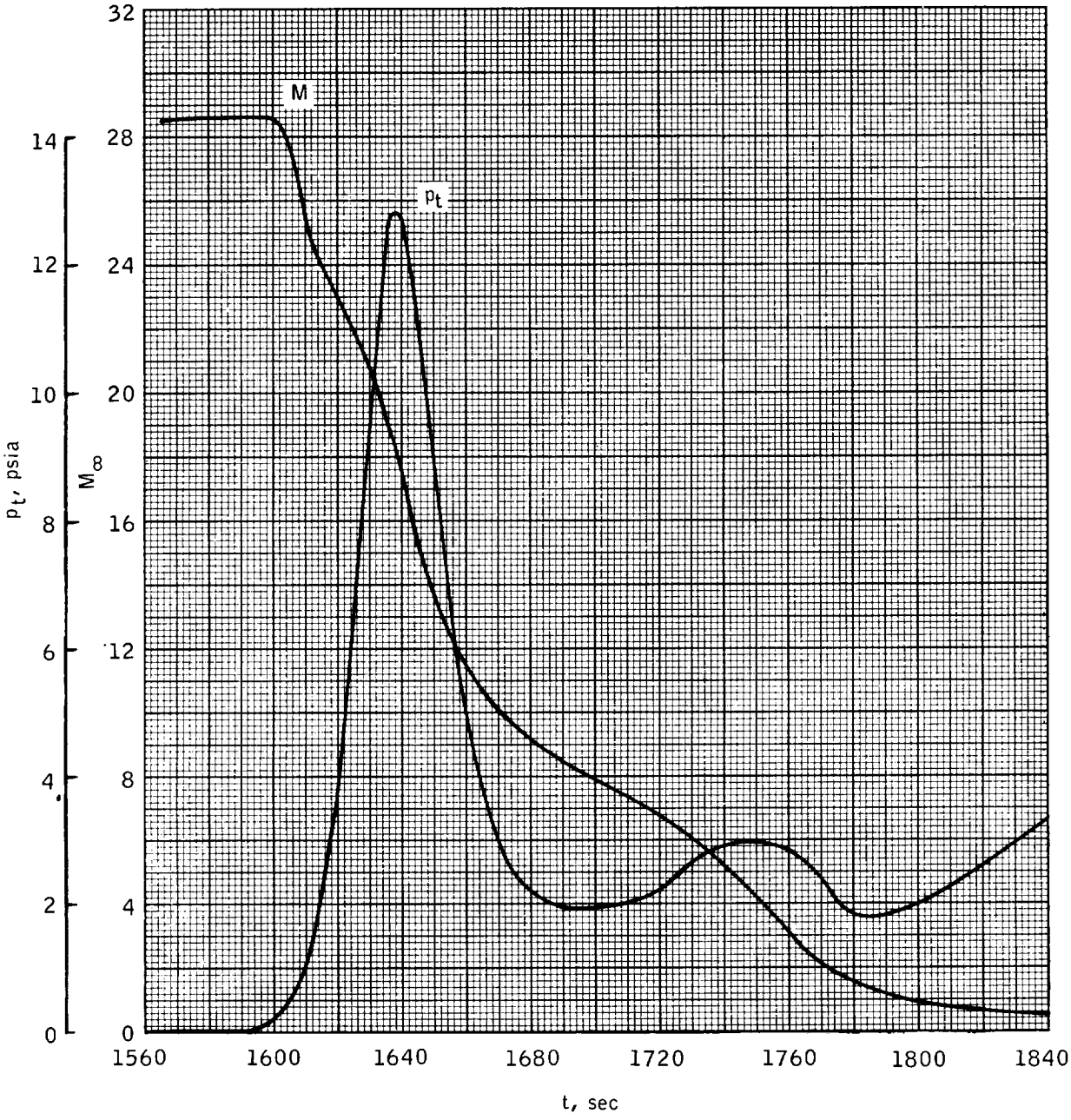

(c) Total pressure and free-stream Mach number.

Figure 3. - Concluded.

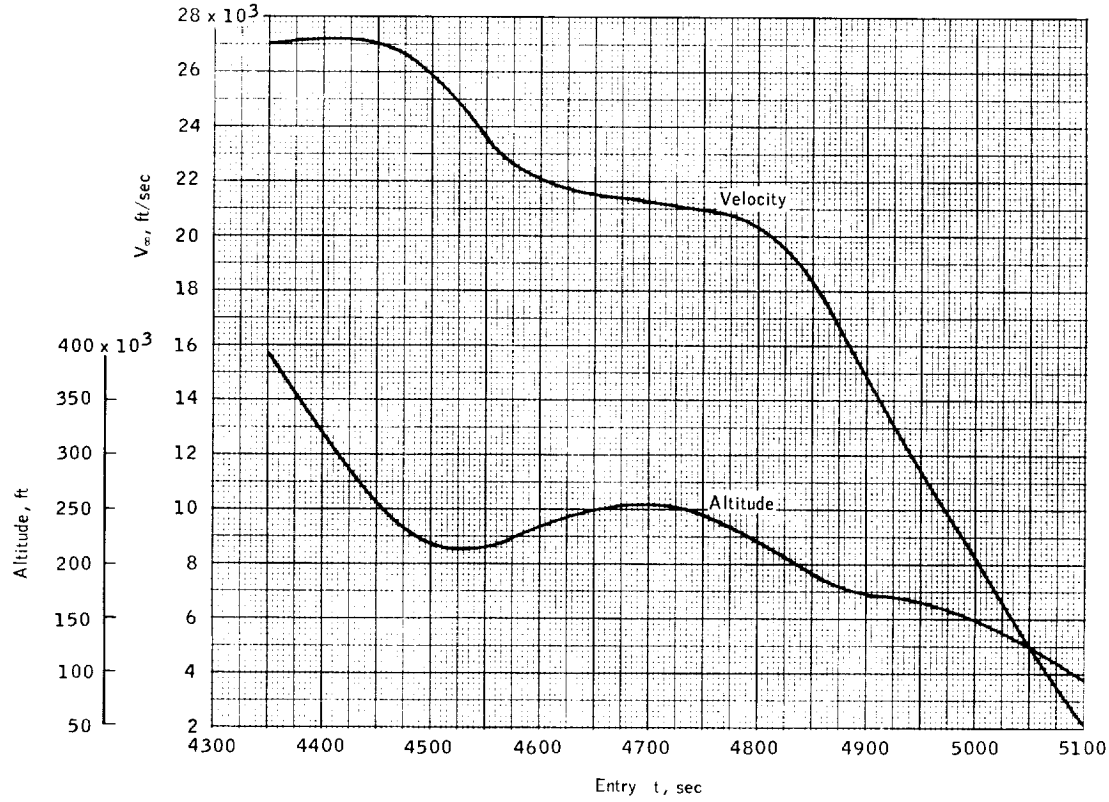

(a) Altitude and relative free-stream velocity.

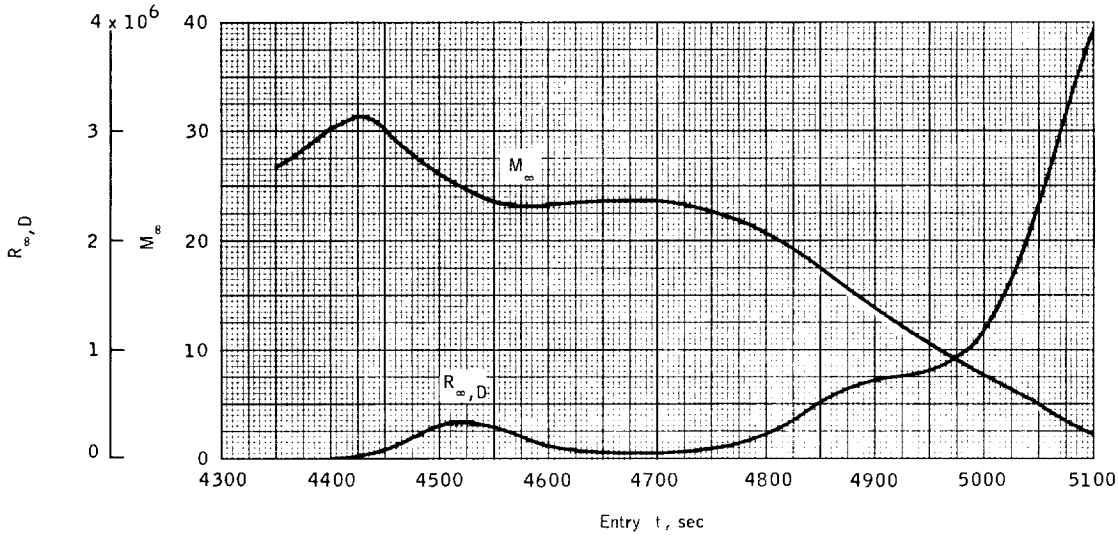

(b) Free-stream Mach number and Reynolds number based on body diameter.

Figure 4. - Entry conditions of spacecraft 011.

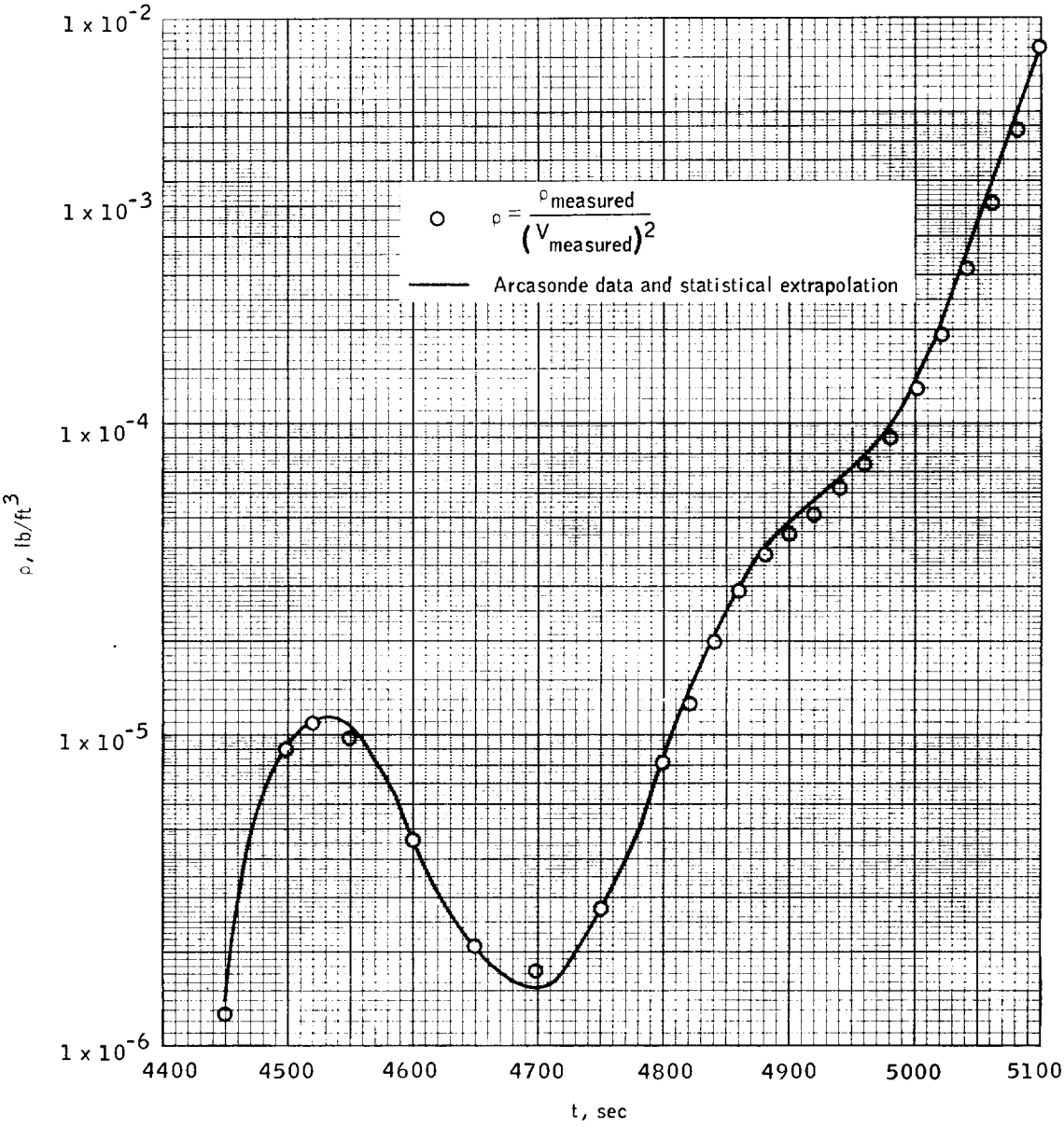

(c) Free-stream density.

Figure 4. - Concluded.

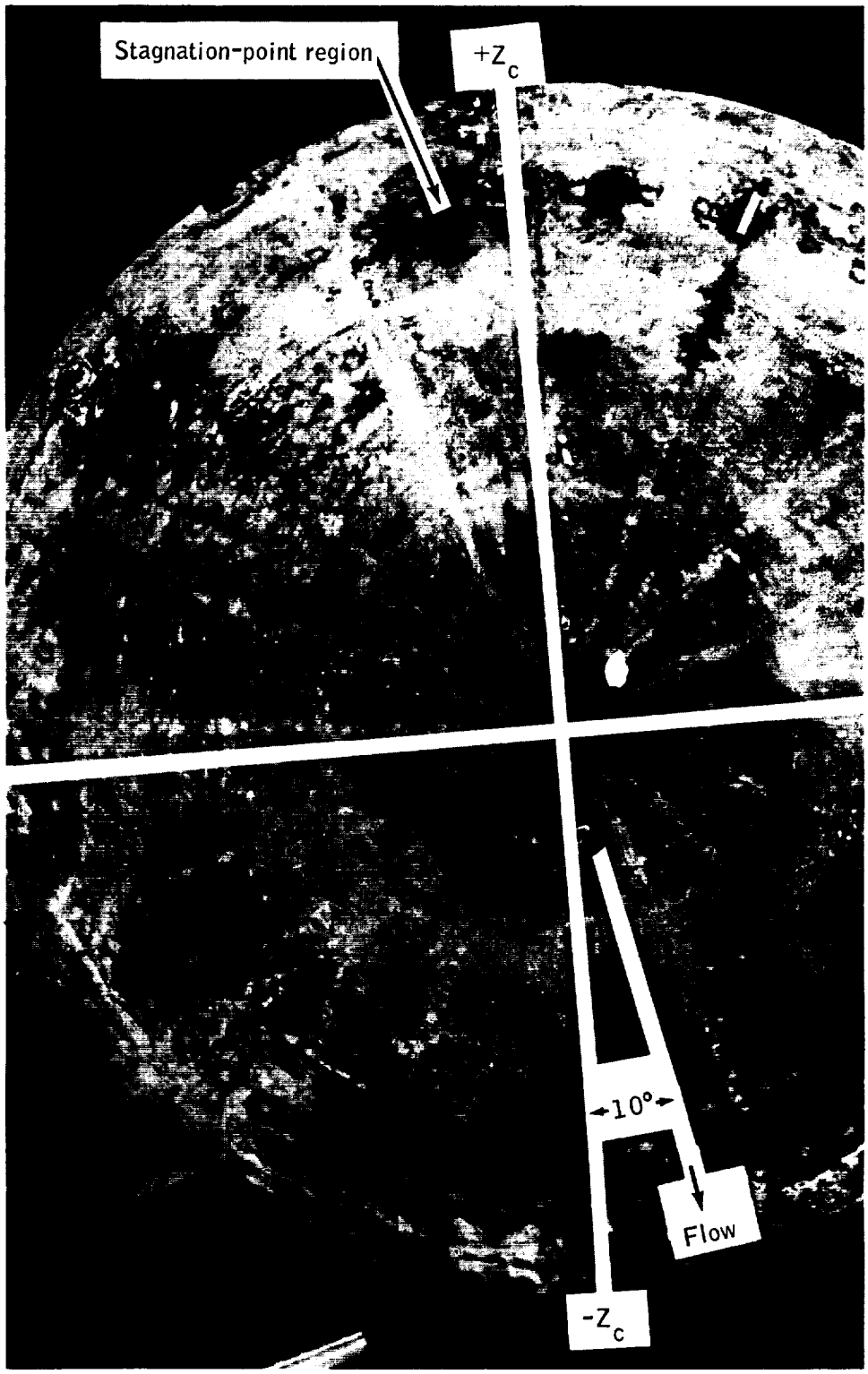

Figure 5. - Photograph showing streak patterns on aft heat shield of spacecraft 009.

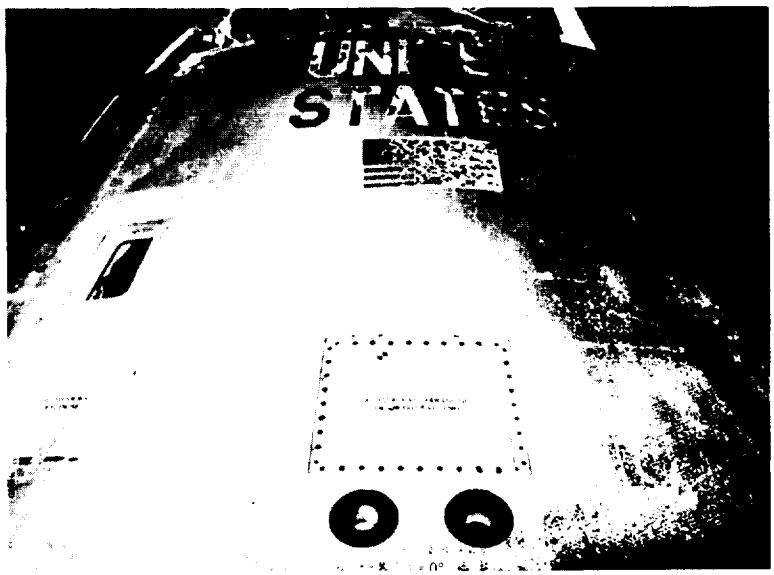

(a) $+Y_c$, $\theta = 0°$.

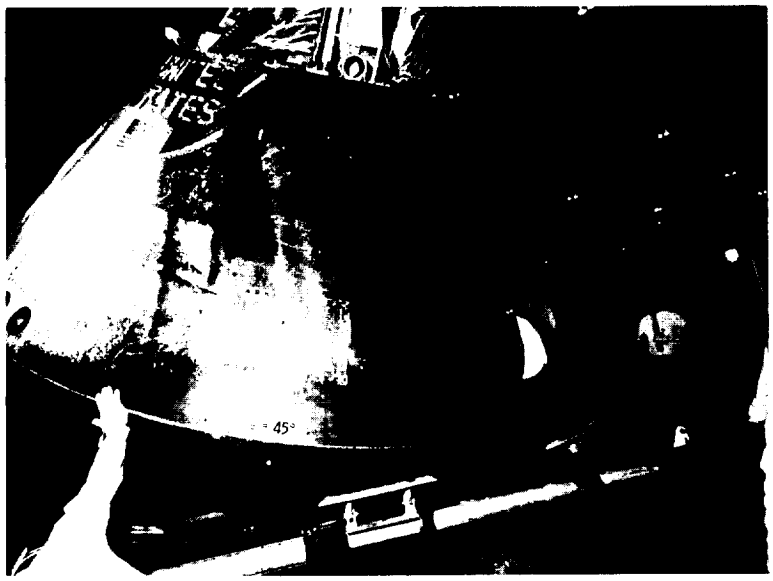

(b) $\theta = 45°$.

Figure 6. - Photograph of conical section showing char demarcation.

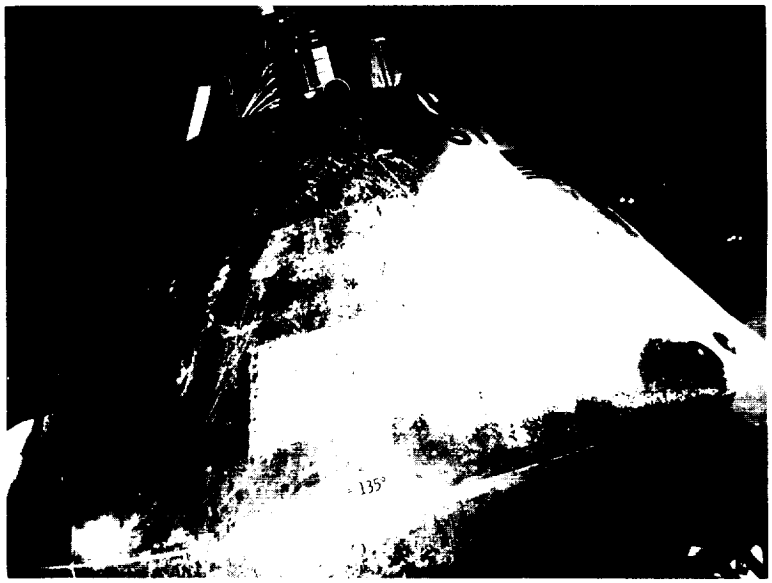

(c) $\theta = 135^{\circ}$.

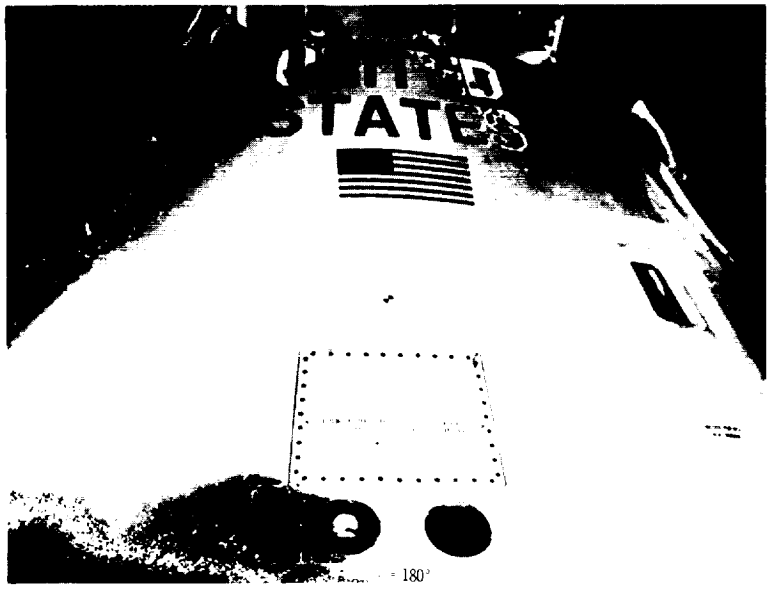

(d) $-Y_c$, $\theta = 180^{\circ}$.

Figure 6. - Concluded.

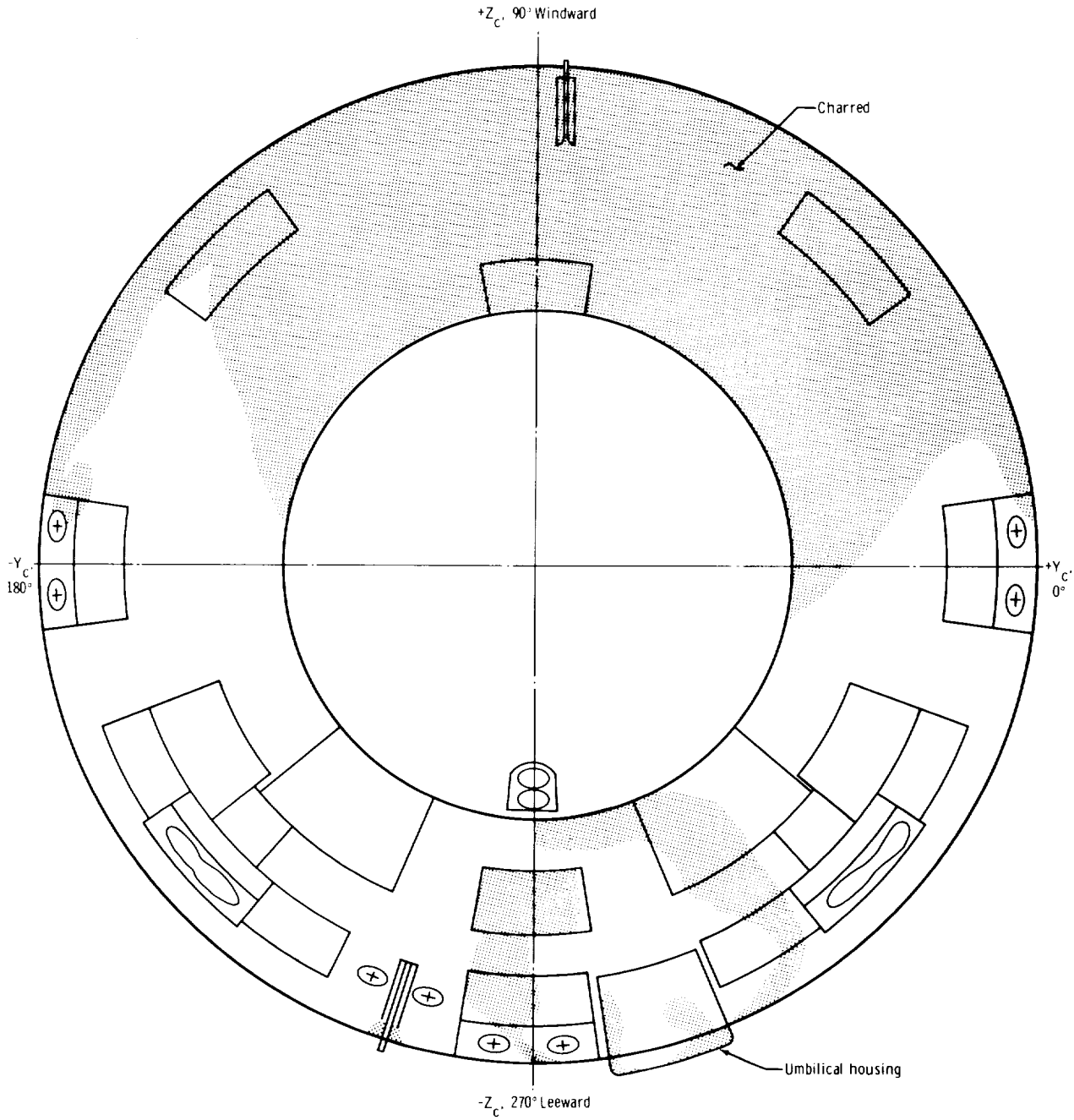

Figure 7. - Illustration of char pattern on conical section.

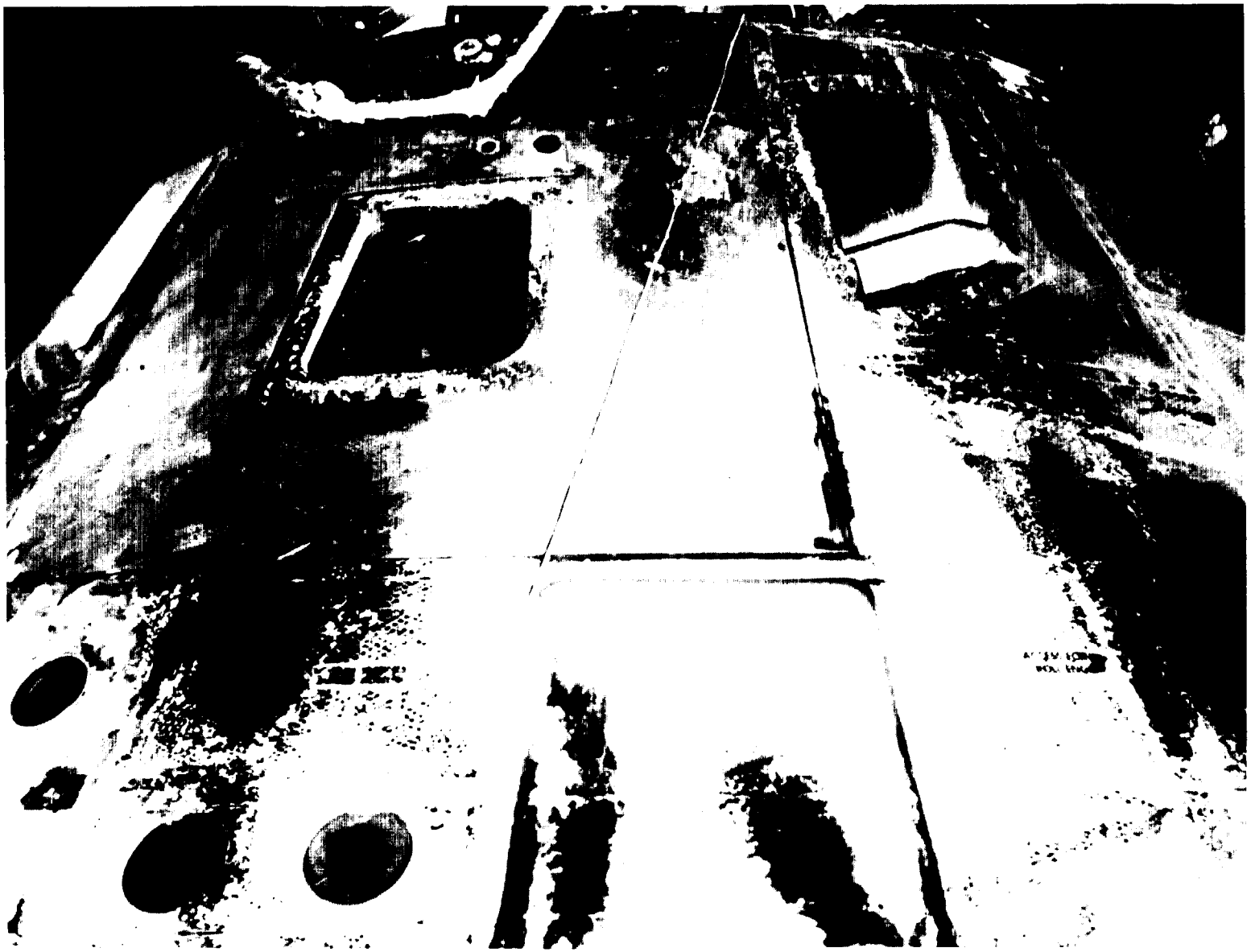

Figure 8. - Photograph of char pattern around the umbilical housing.

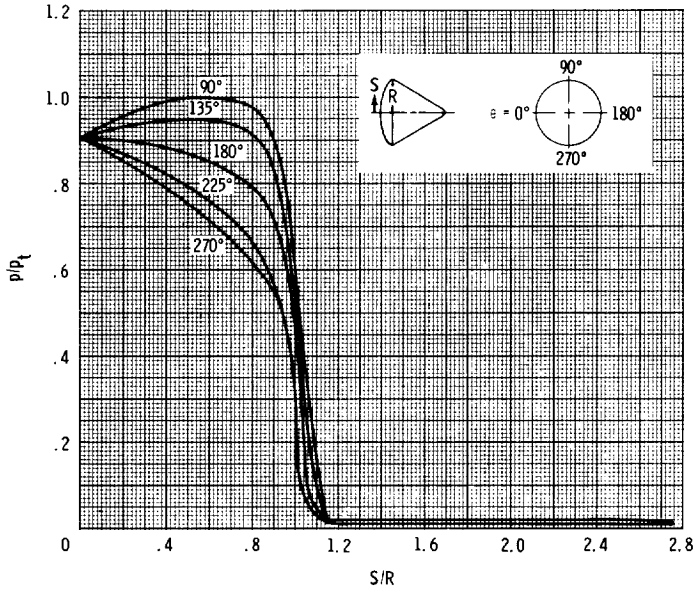

(a) $\alpha = 18^{\circ}$.

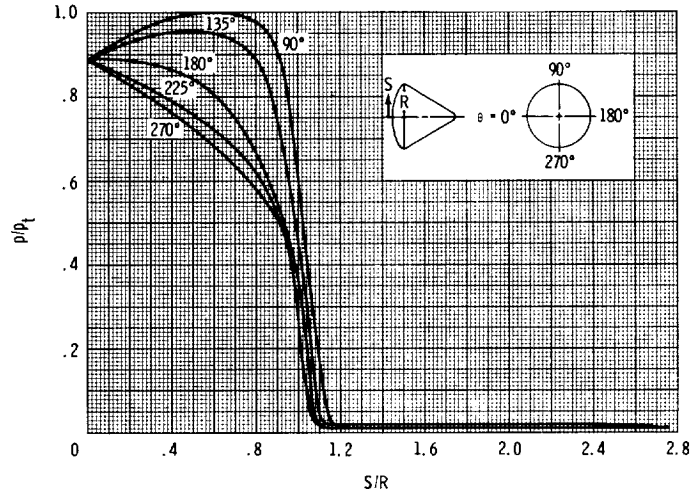

(b) $\alpha = 20^{\circ}$.

Figure 9. - Wind-tunnel distributions of local-to-total pressure ratio.

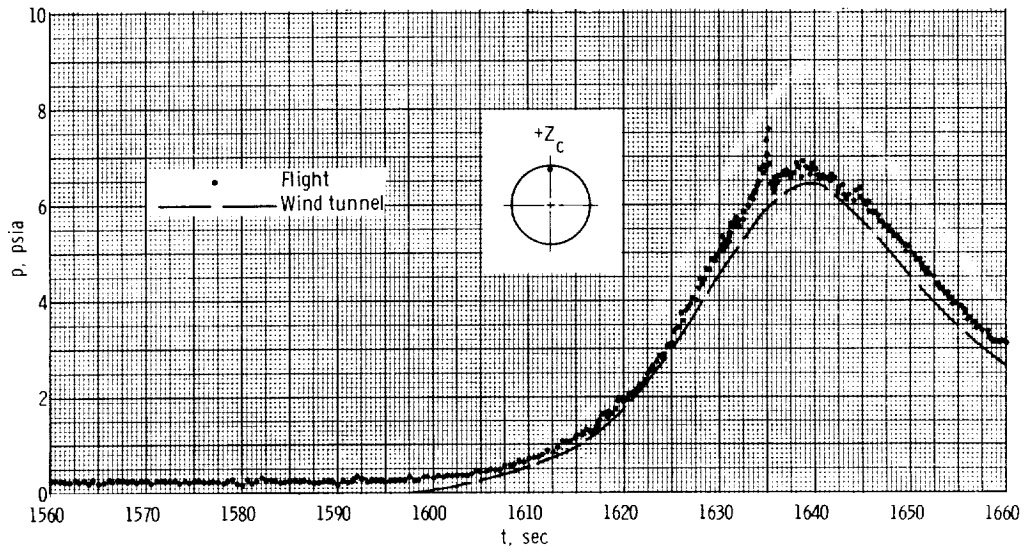

(a) $Y_c = 0, \quad Z_c = 75.$

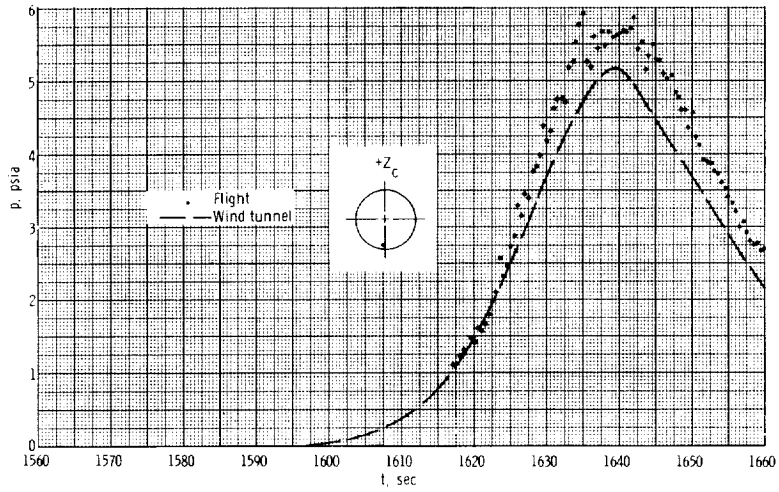

(b) $Y_c = 2.25, \quad Z_c = -71.8.$

Figure 10. - Time histories of pressures measured on spacecraft 009.

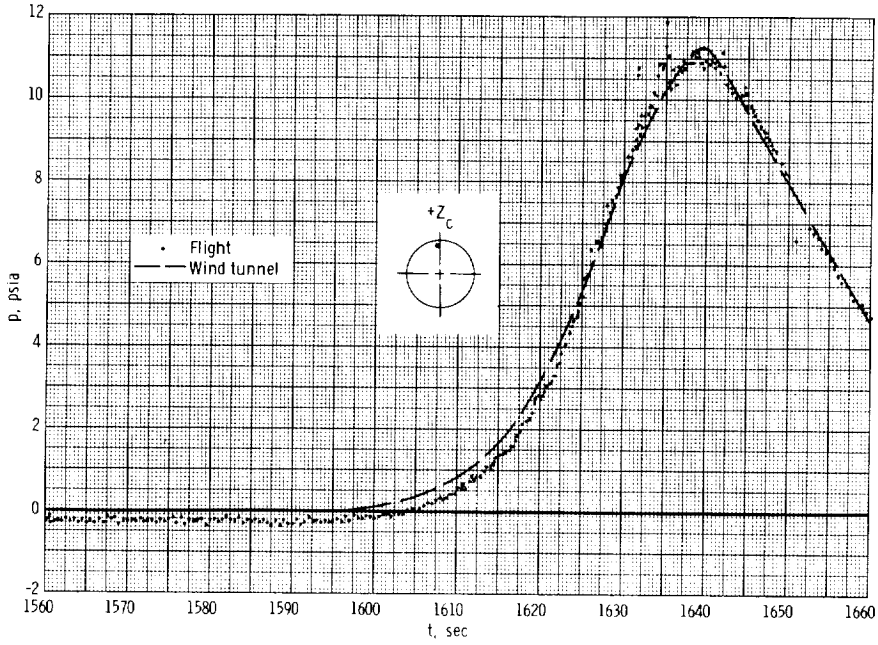

(c) $Y_c = 2.25$, $Z_c = 70.5$, $S/R = 0.94$.

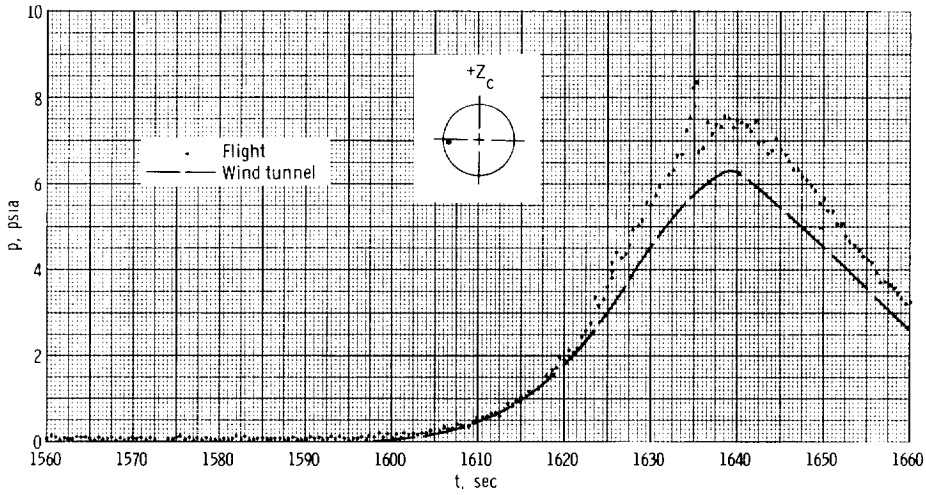

(d) $Y_c = 71.8$, $Z_c = -0.8$.

Figure 10. - Continued.

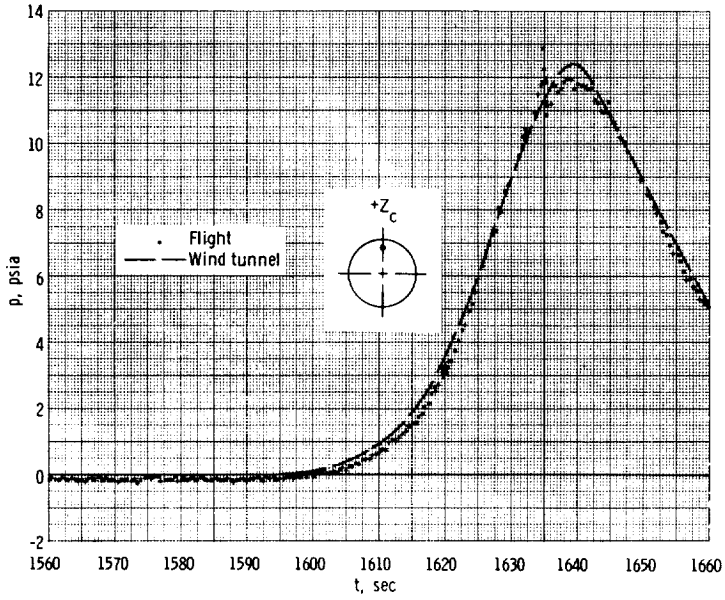

(e) $Y_c = 0, \quad Z_c = 58.4.$

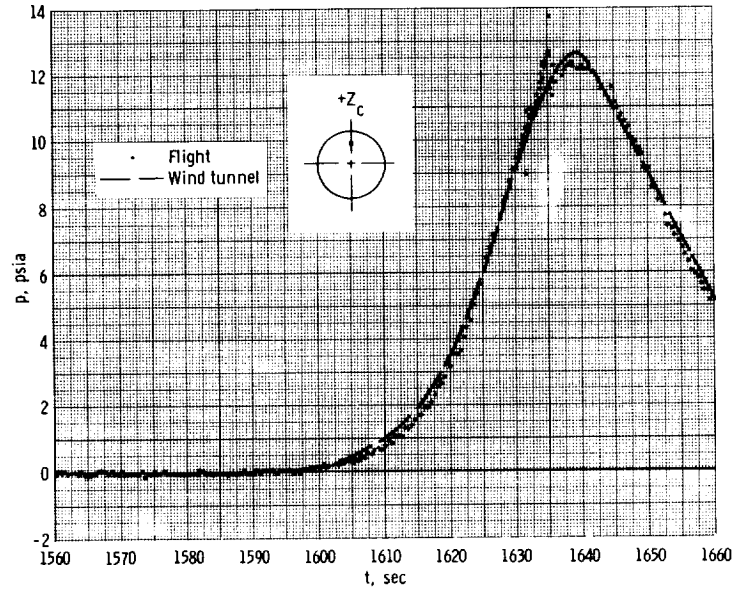

(f) $Y_c = 0, \quad Z_c = 54.4.$

Figure 10. - Continued.

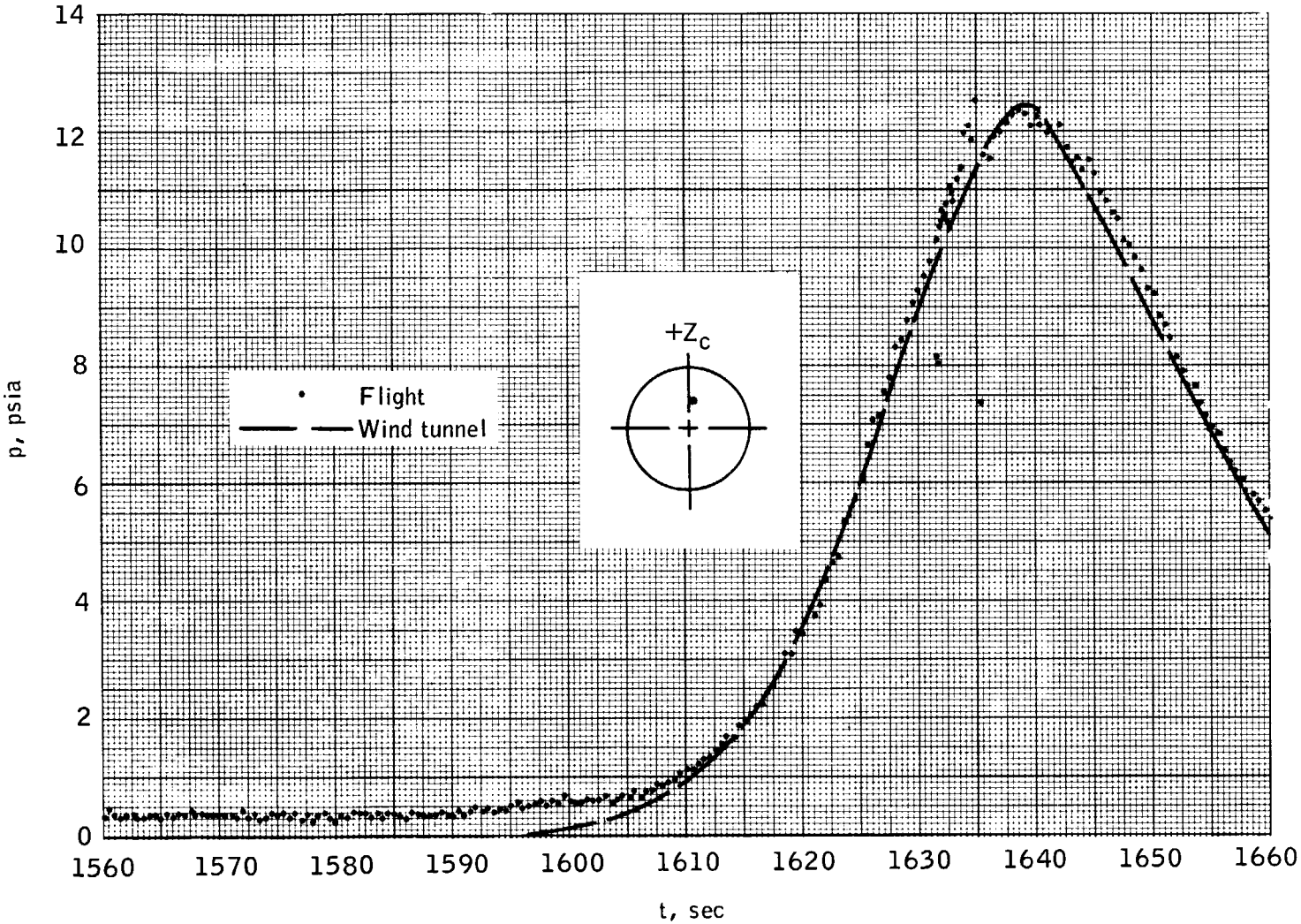

(g) $Y_c = -2.1$, $Z_c = 35.2$.

Figure 10. - Continued.

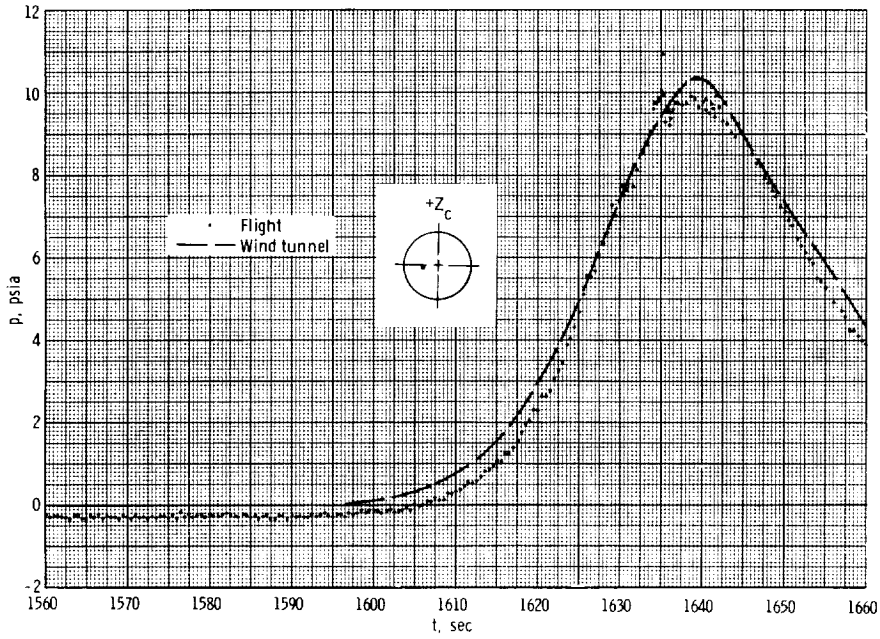

(h) $Y_c = 34.3$, $Z_c = -2.1$.

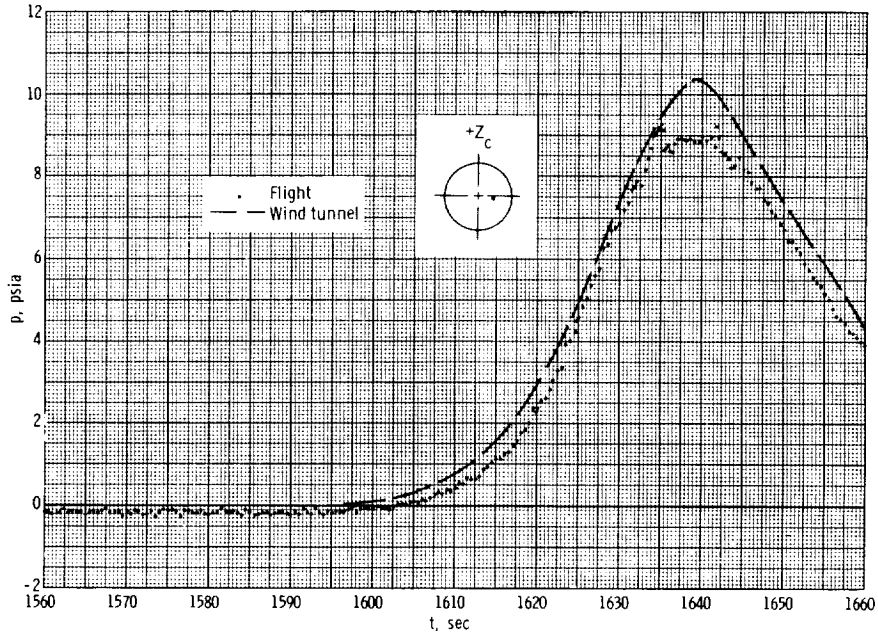

(i) $Y_c = -36.7$, $Z_c = -3.8$.

Figure 10. - Continued.

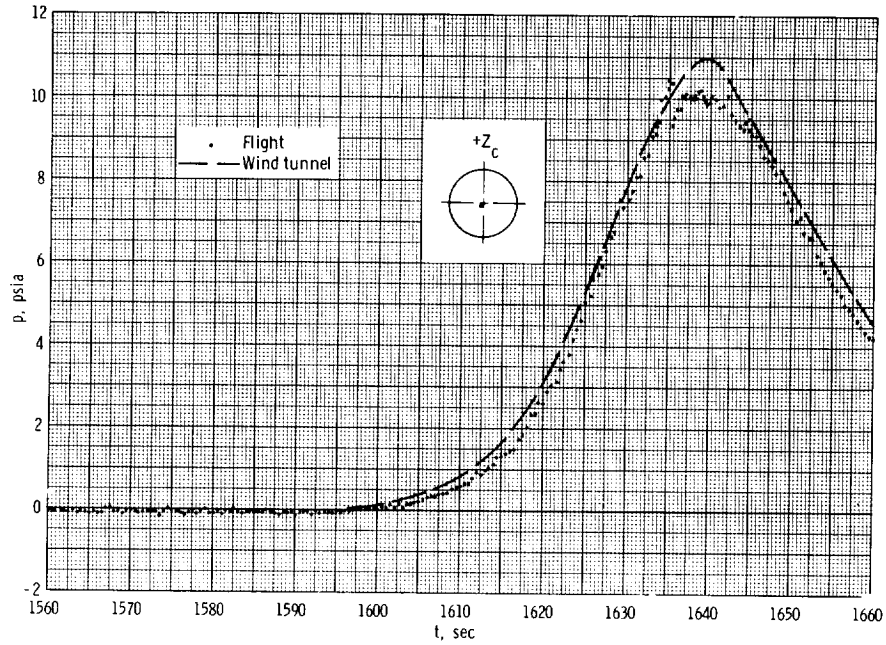

(j) $Y_c = 6.0, \quad Z_c = -2.5.$

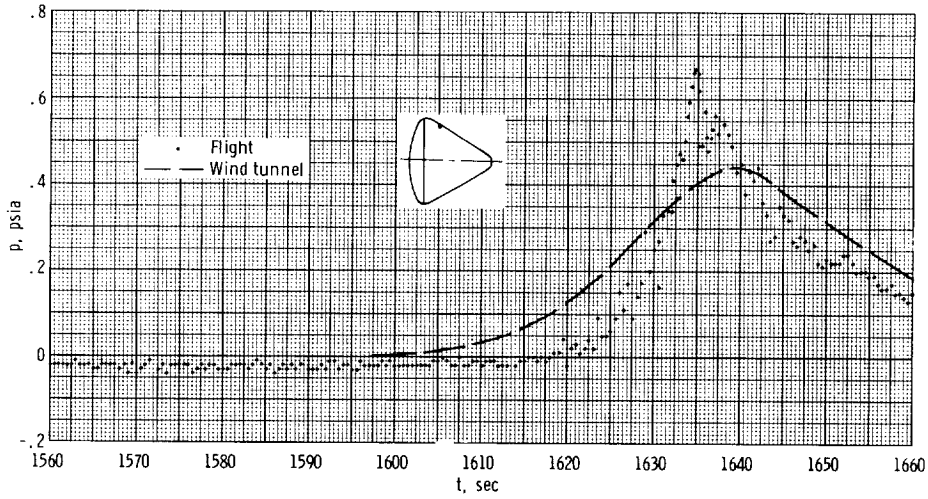

(k) $X_c = 45.5, \quad \theta = 88^\circ, \quad S/R = 1.44.$

Figure 10. - Continued.

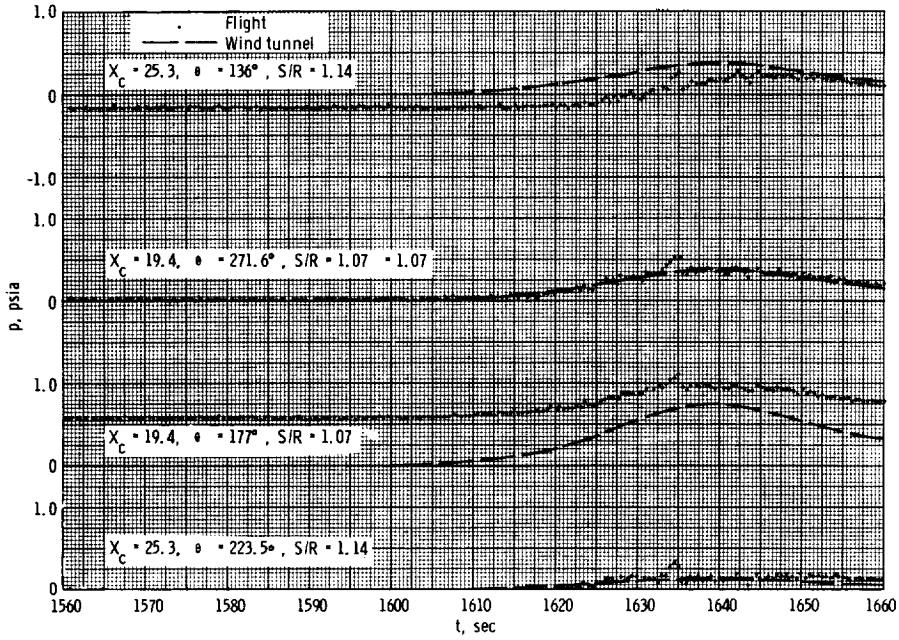

(l) Toroid-conical tangency point.

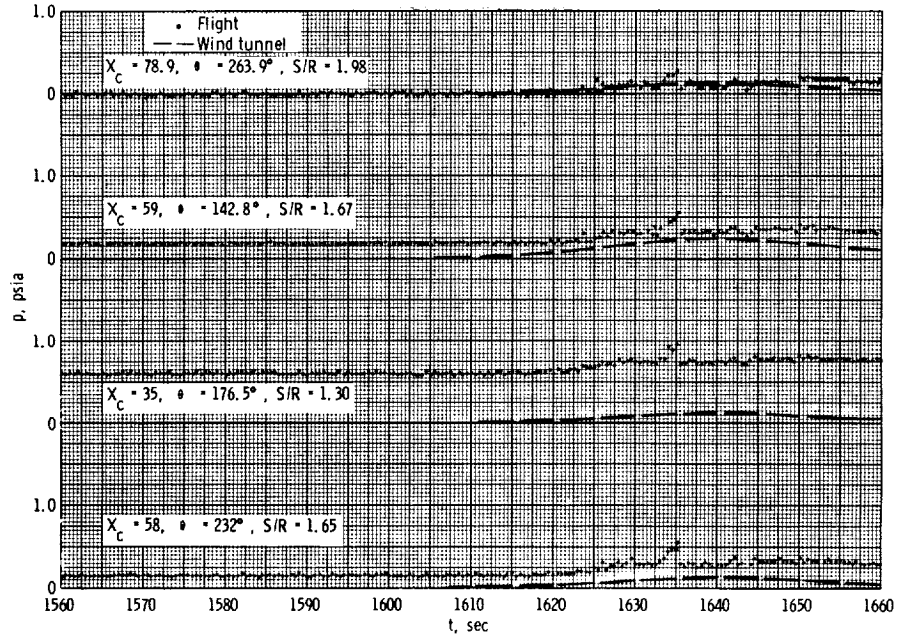

(m) Conical section.

Figure 10. - Concluded.

Figure 11. - Photograph of flow pattern around windward scimitar antenna.

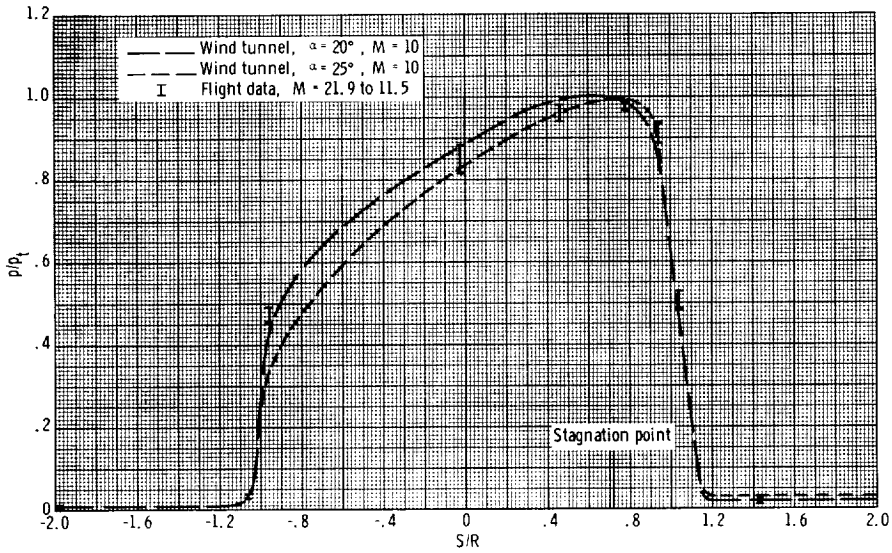

(a) Pitch plane, $-Z_c$ to $+Z_c$.

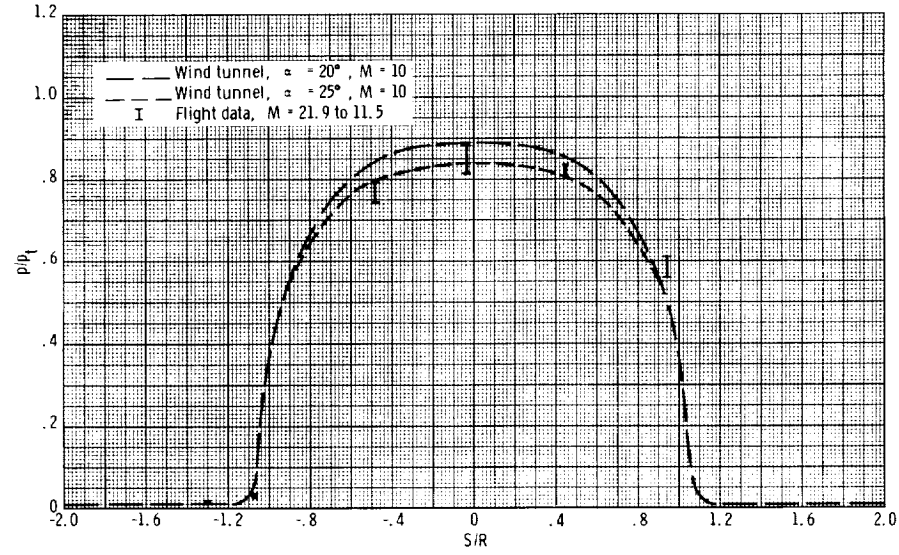

(b) Yaw plane, $-Y_c$ to $+Y_c$.

Figure 12. - Comparison of spacecraft 009 pressure distribution with wind-tunnel results.

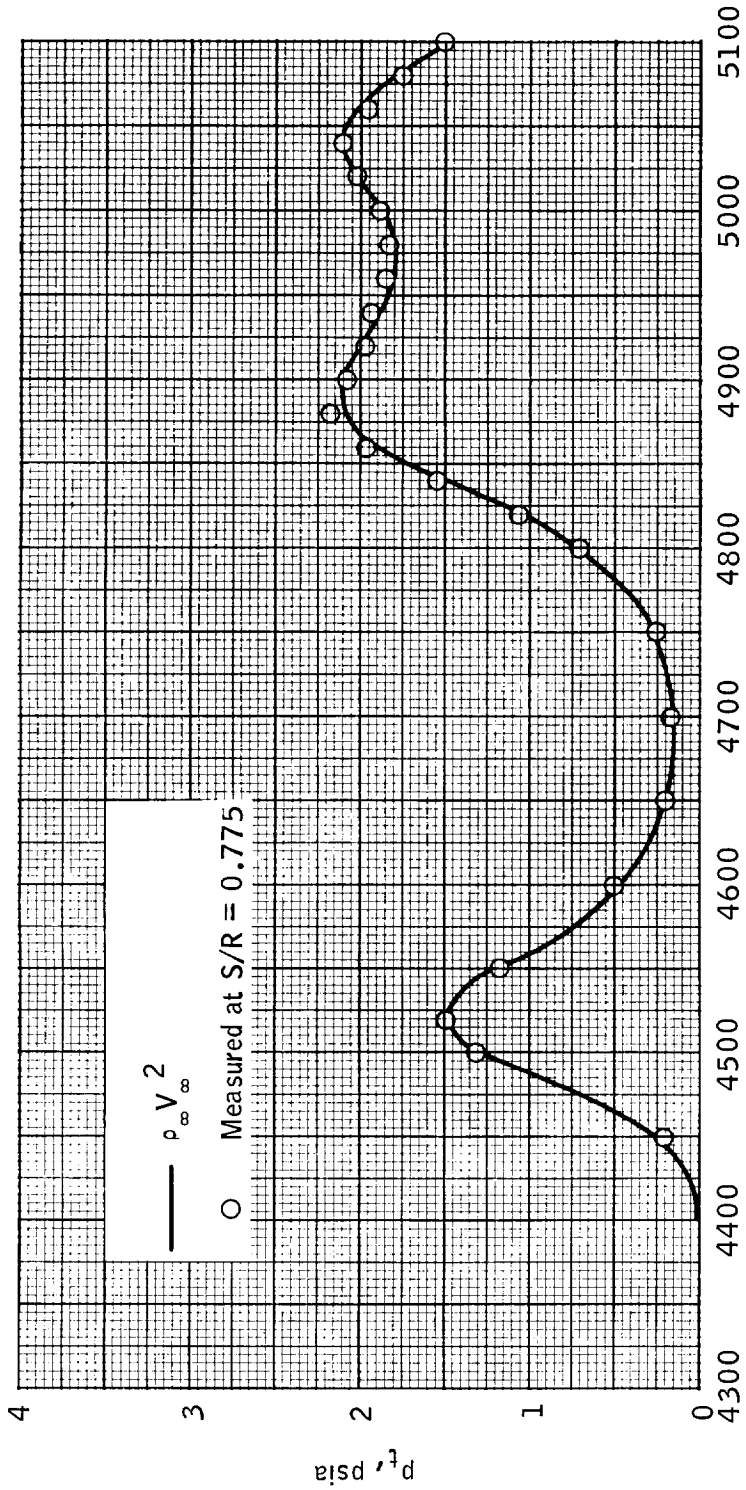

Figure 13. - Stagnation pressure measured on spacecraft 011.

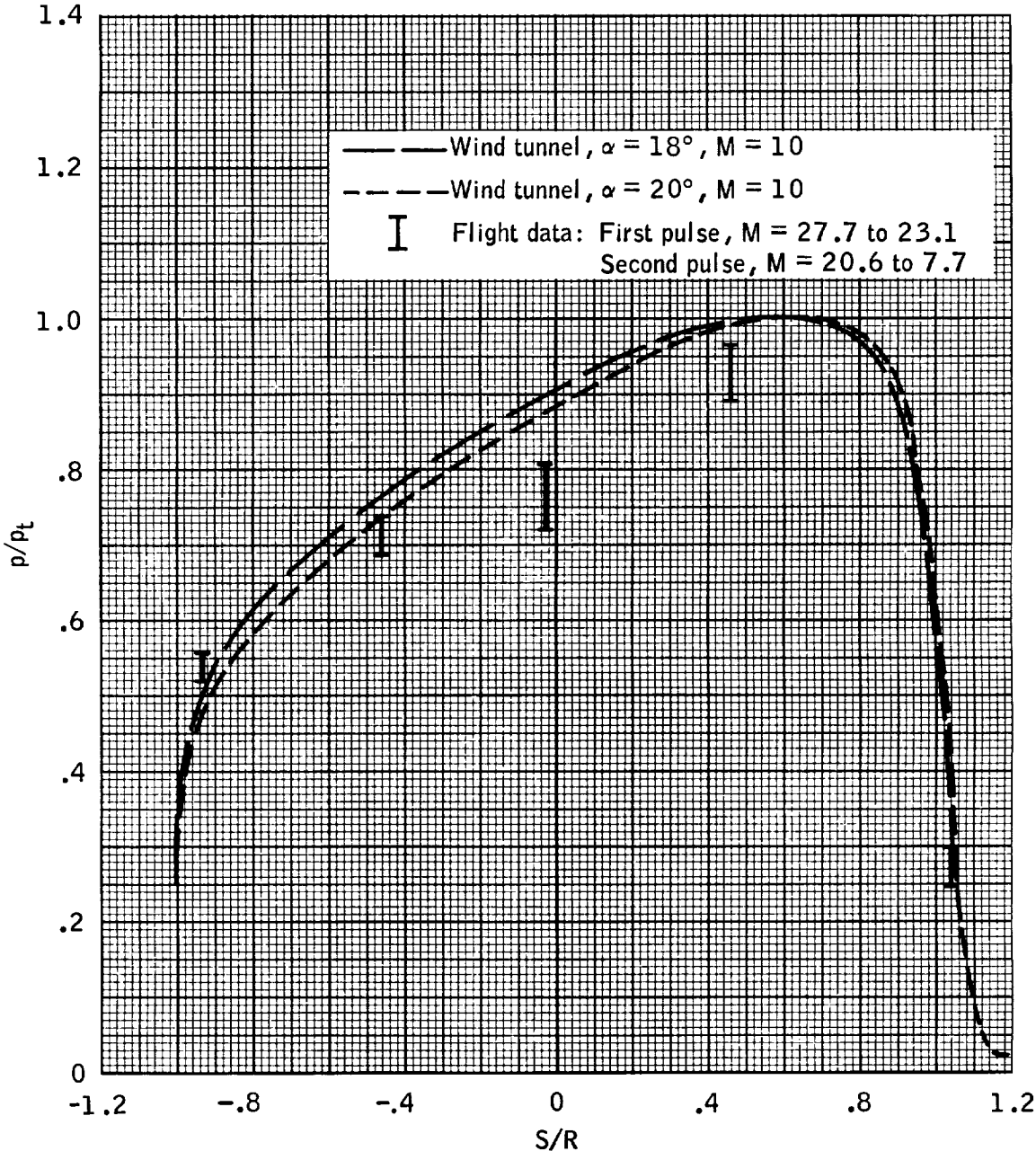

(a) Pitch plane, θ = 90° and 270°.

Figure 14. - Comparison of spacecraft 011 pressure distribution with wind-tunnel results.

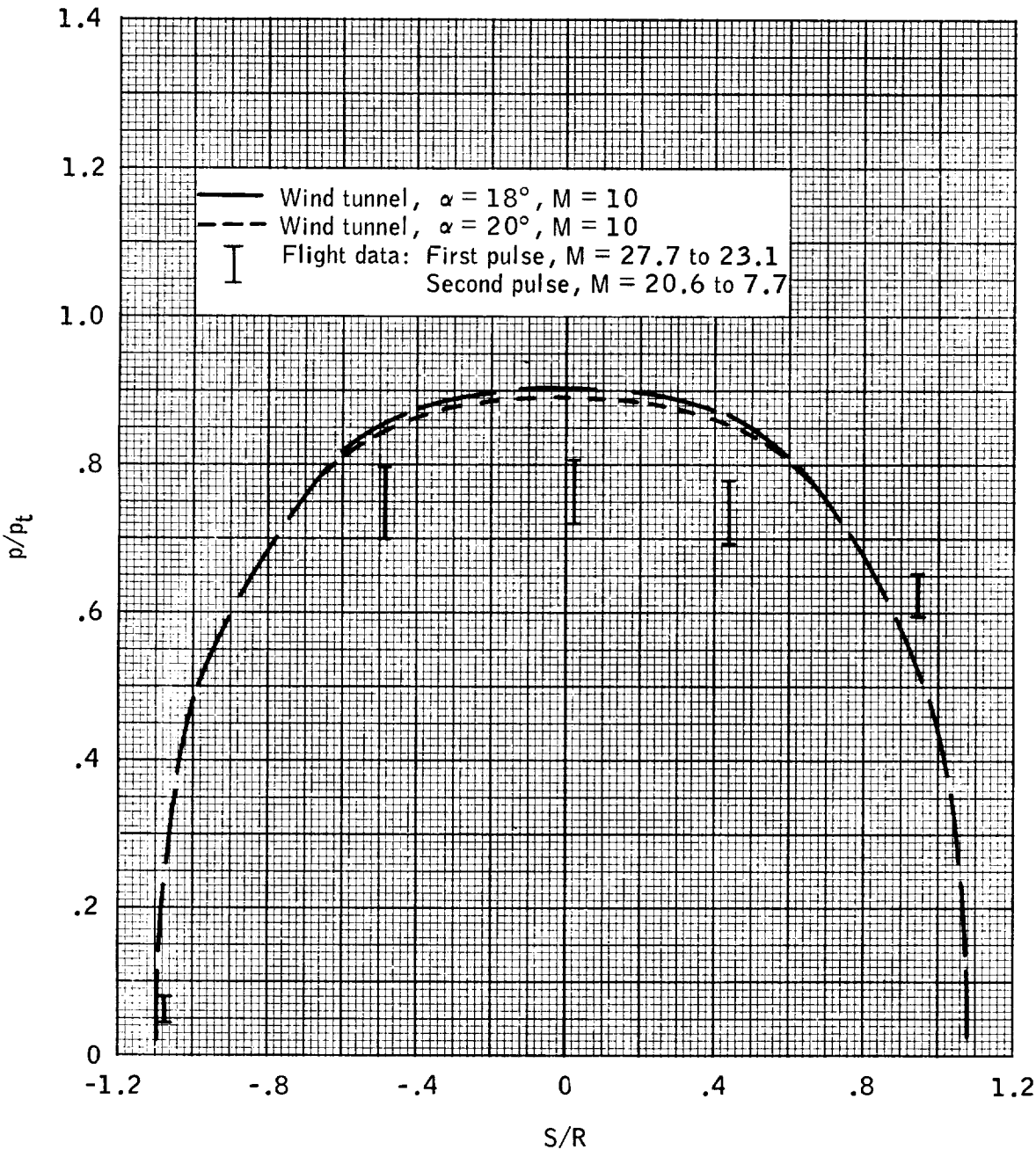

(b) Yaw plane, $\theta = 0^\circ$ and 180°.

Figure 14. - Concluded.

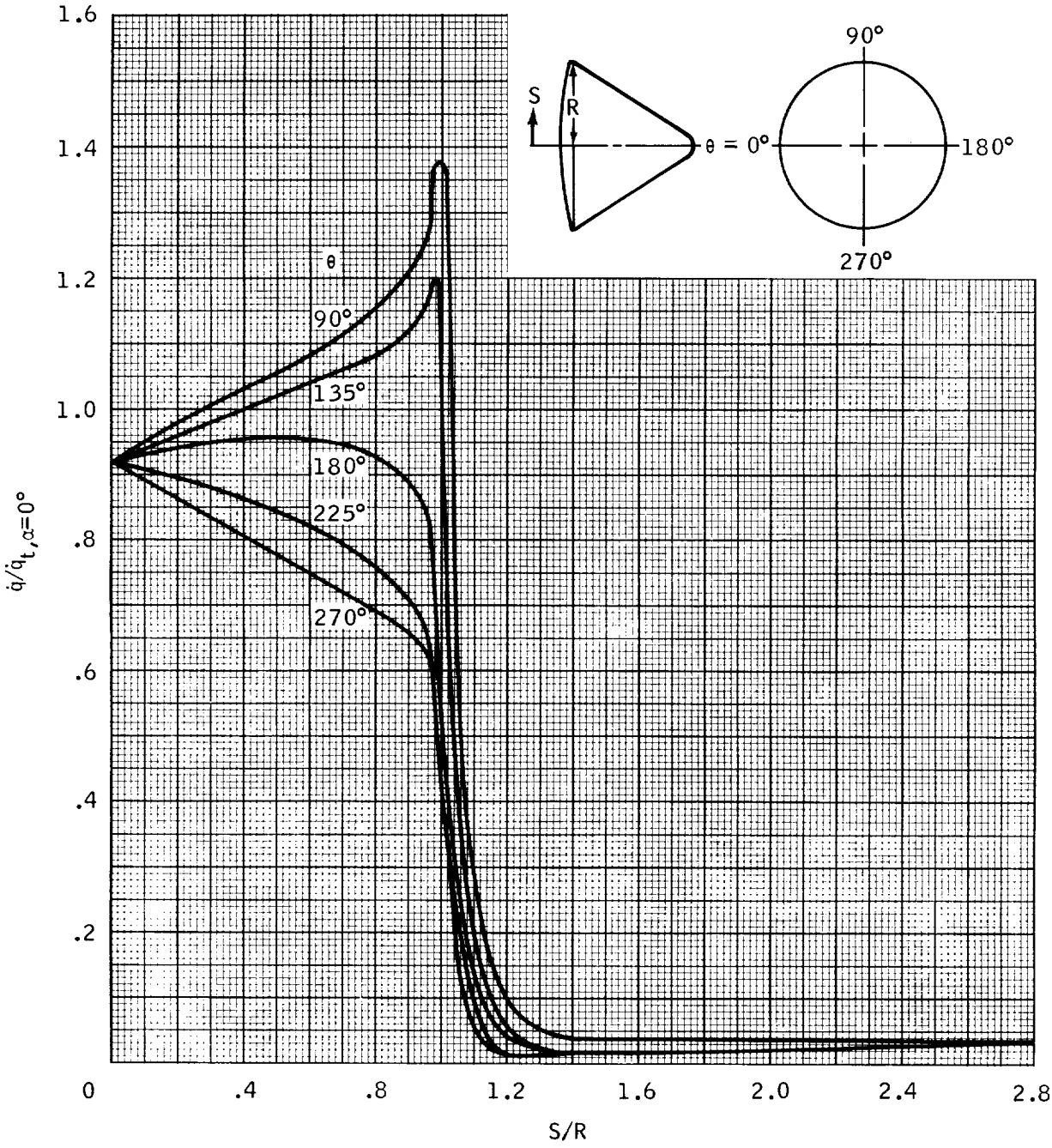

(a) $\alpha = 18°$.

Figure 15. - Wind-tunnel distribution of local heating rate divided by zero angle-of-attack stagnation-point heating rate.

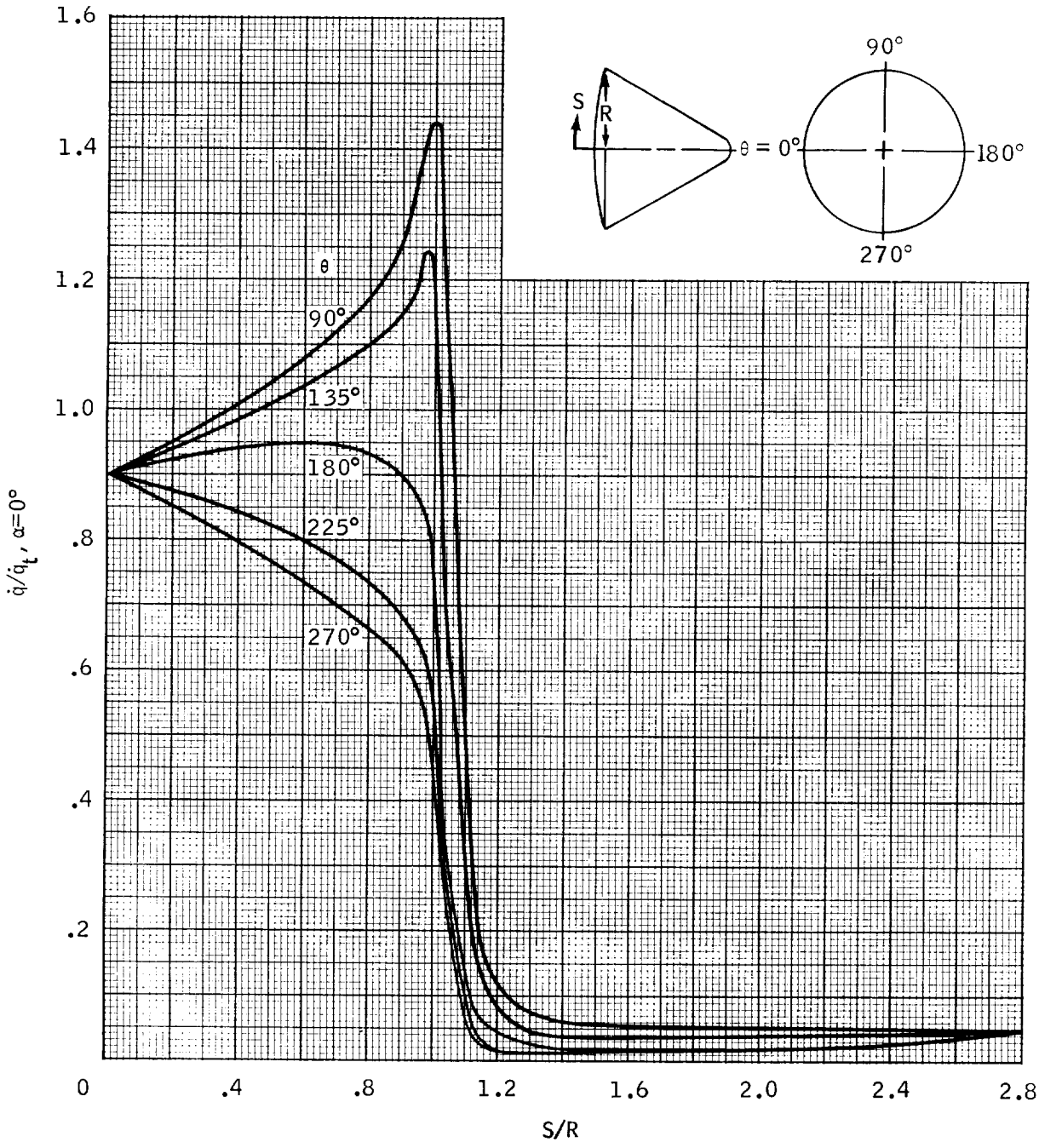

(b) $\alpha = 20^\circ$.

Figure 15. - Concluded.

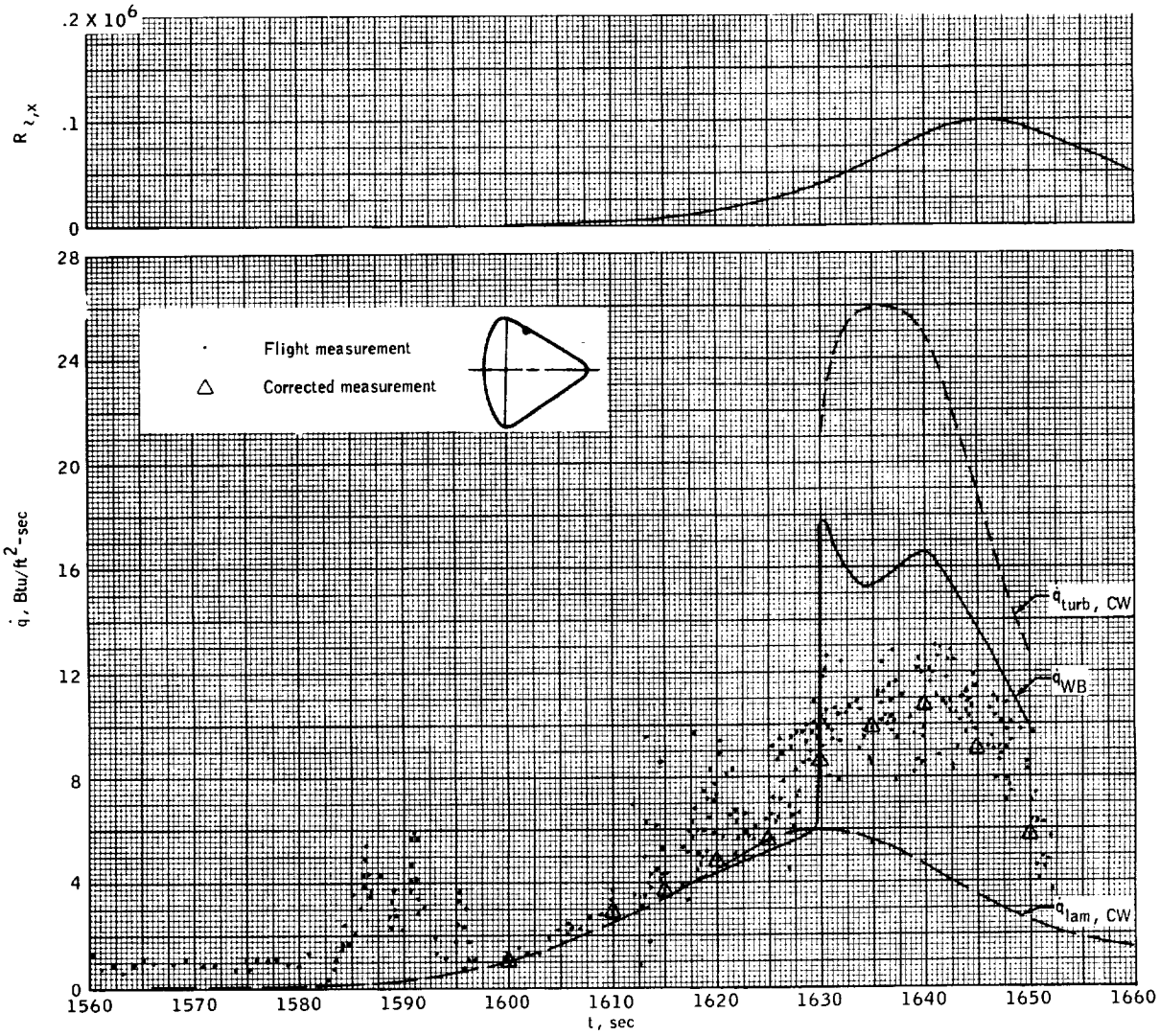

(a) $X_c = 45.5$, $\varphi = 85.3°$, $S/R = 1.475$.

Figure 16. - Histories of local Reynolds number and heating rates on conical section of spacecraft 009.

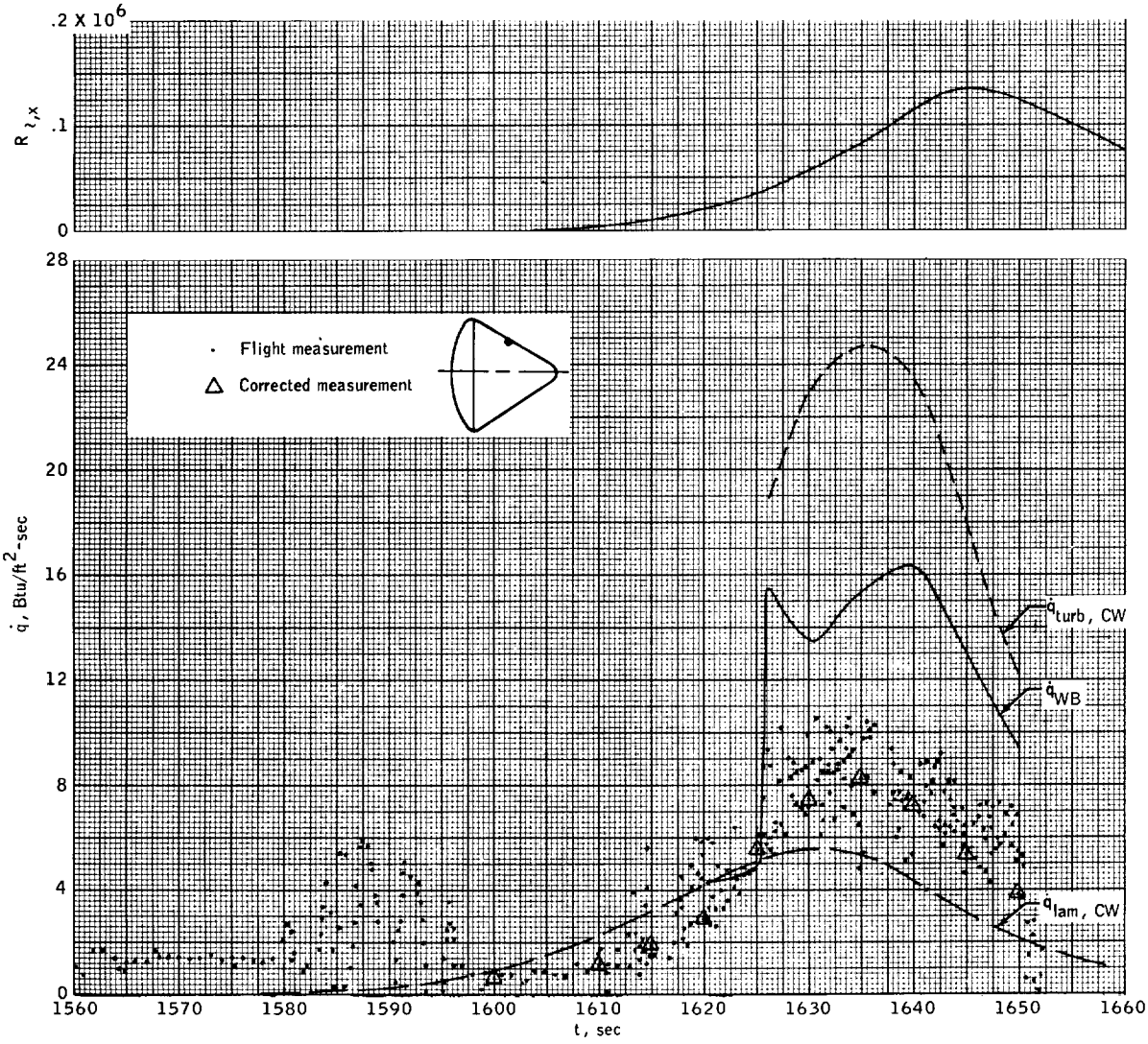

(b) $X_c = 64.8$, $\theta = 92°$, S/R = 1.775.

Figure 16. - Continued.

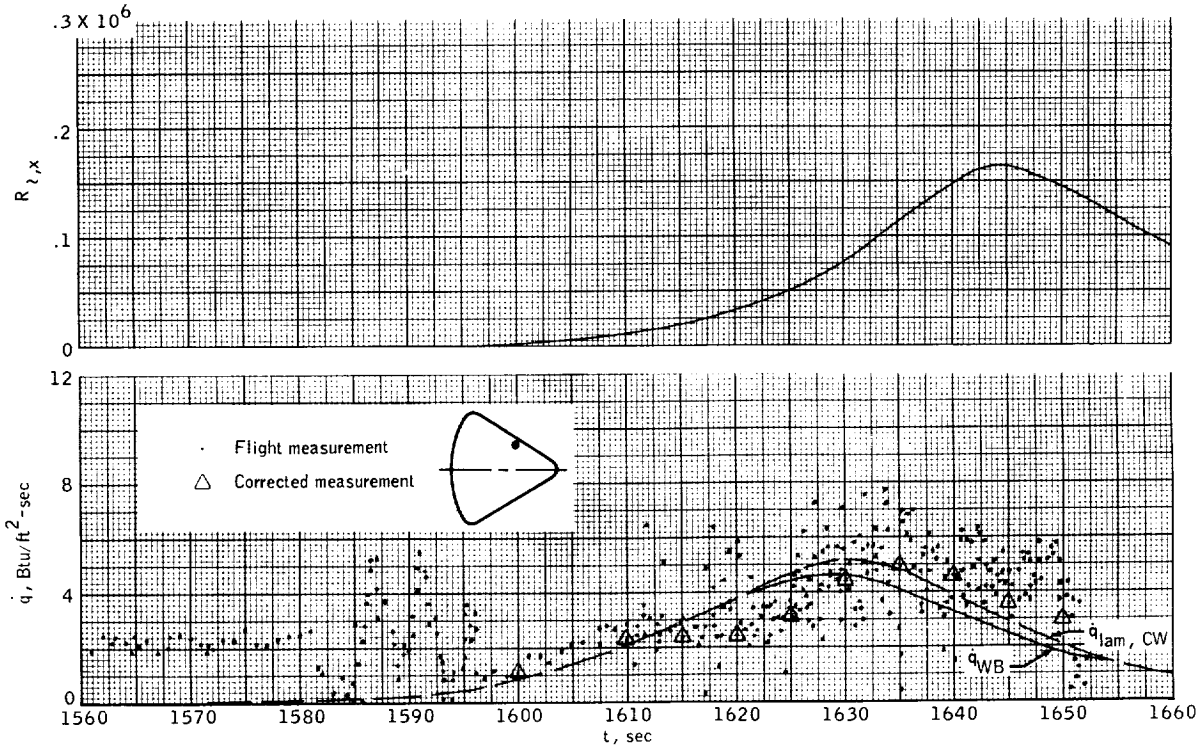

(c) $X_c = 78.9$, $\theta = 115°$, $S/R = 1.99$.

Figure 16. - Continued.

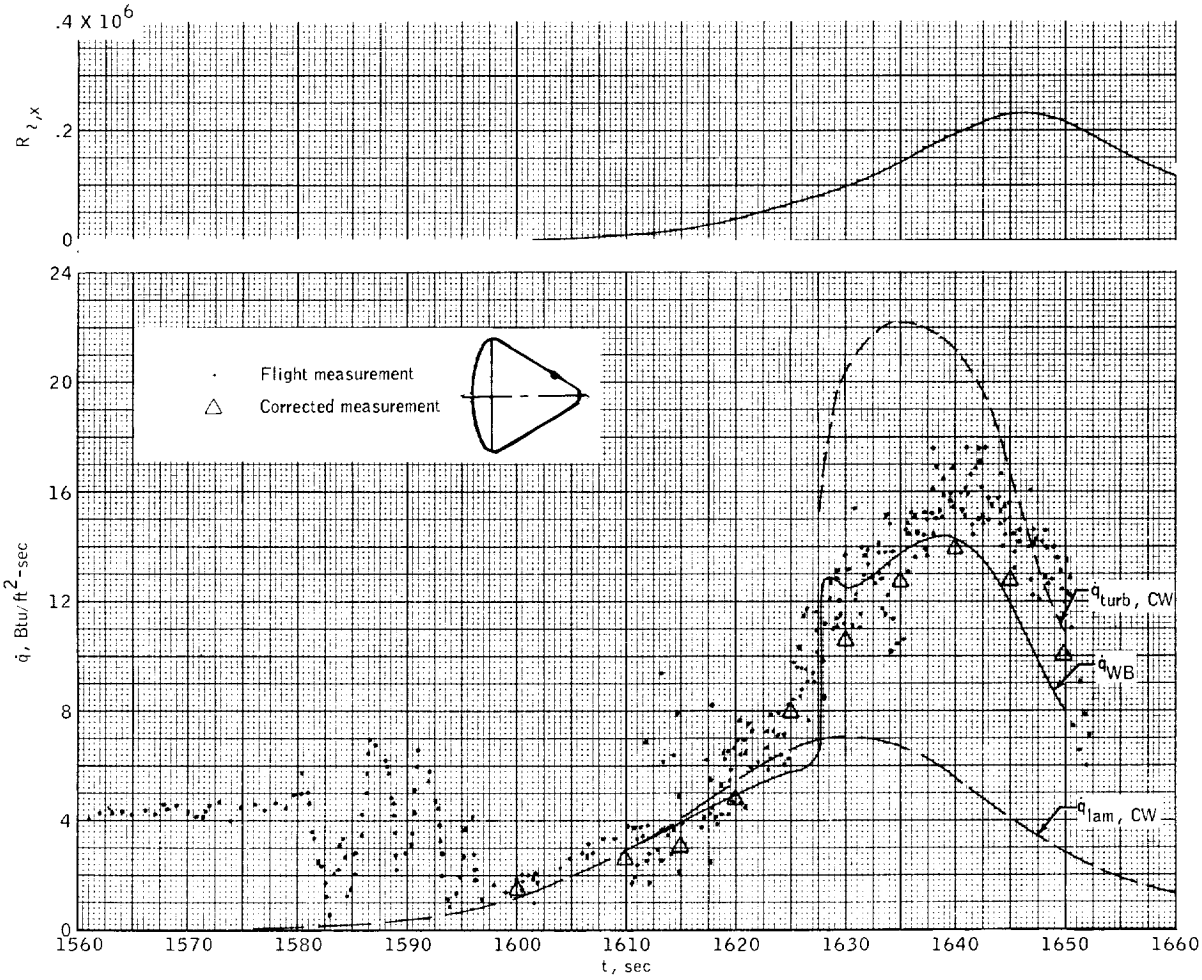

(d) $X_c = 114$, $\theta = 83.4°$, $S/R = 2.5$.

Figure 16. - Continued.

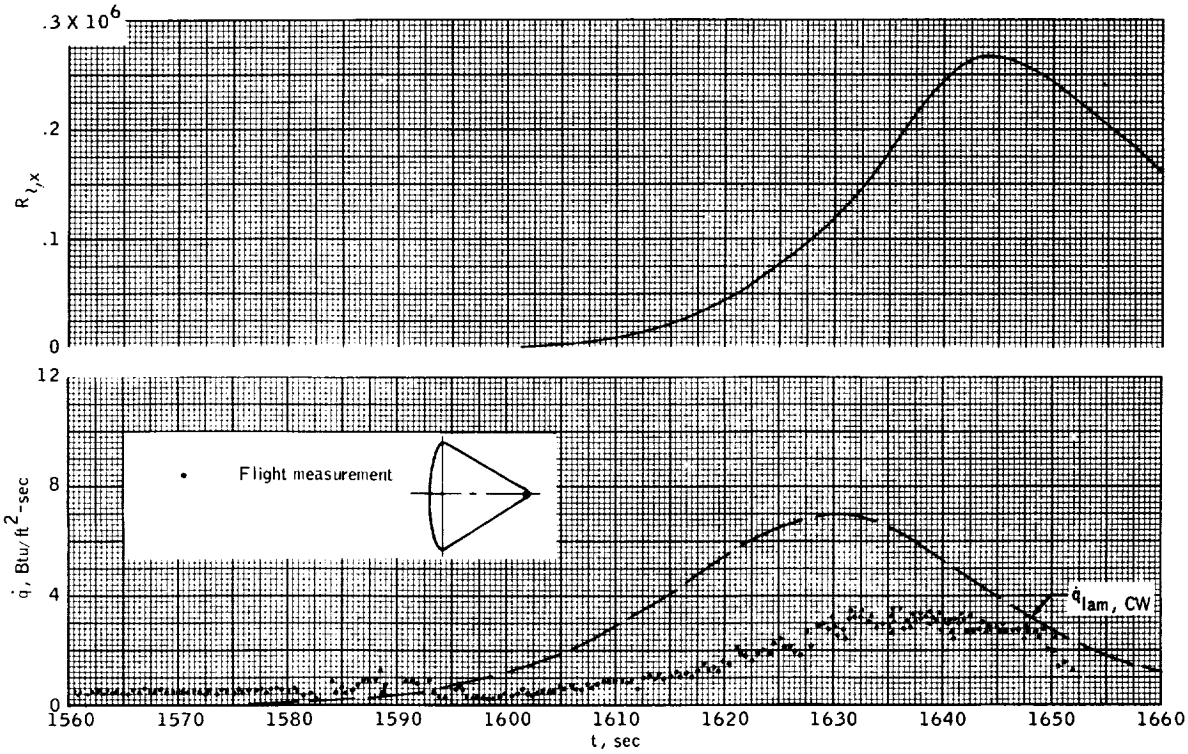

(e) Apex.

Figure 16. - Continued.

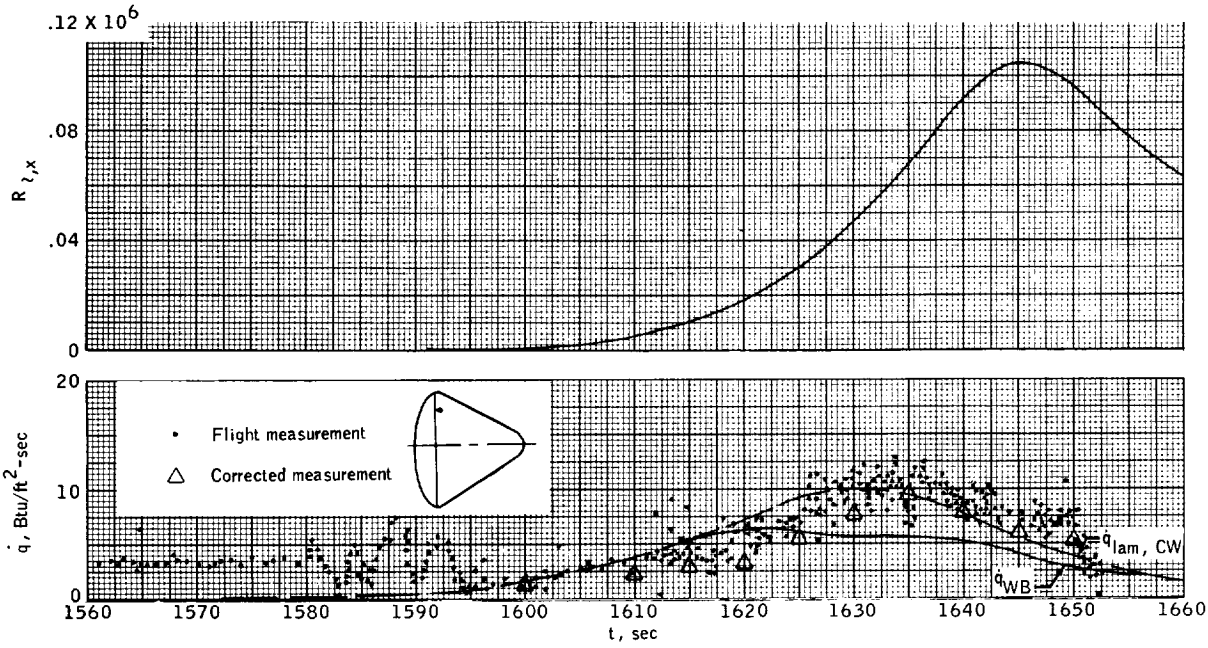

(f) $X_c = 25.3$, $\theta = 138°$, $S/R = 1.16$.

Figure 16. - Continued.

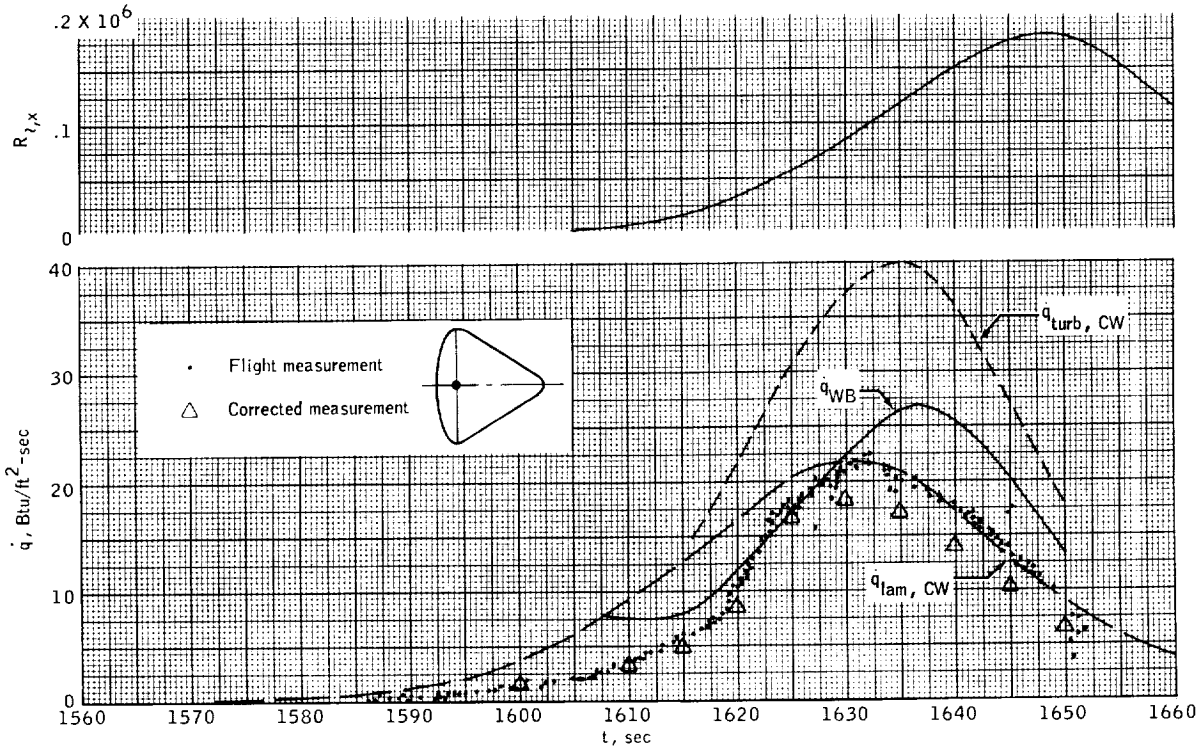

(g) $X_c = 19.4$, $\theta = 178.5°$, $S/R = 1.071$.

Figure 16. - Continued.

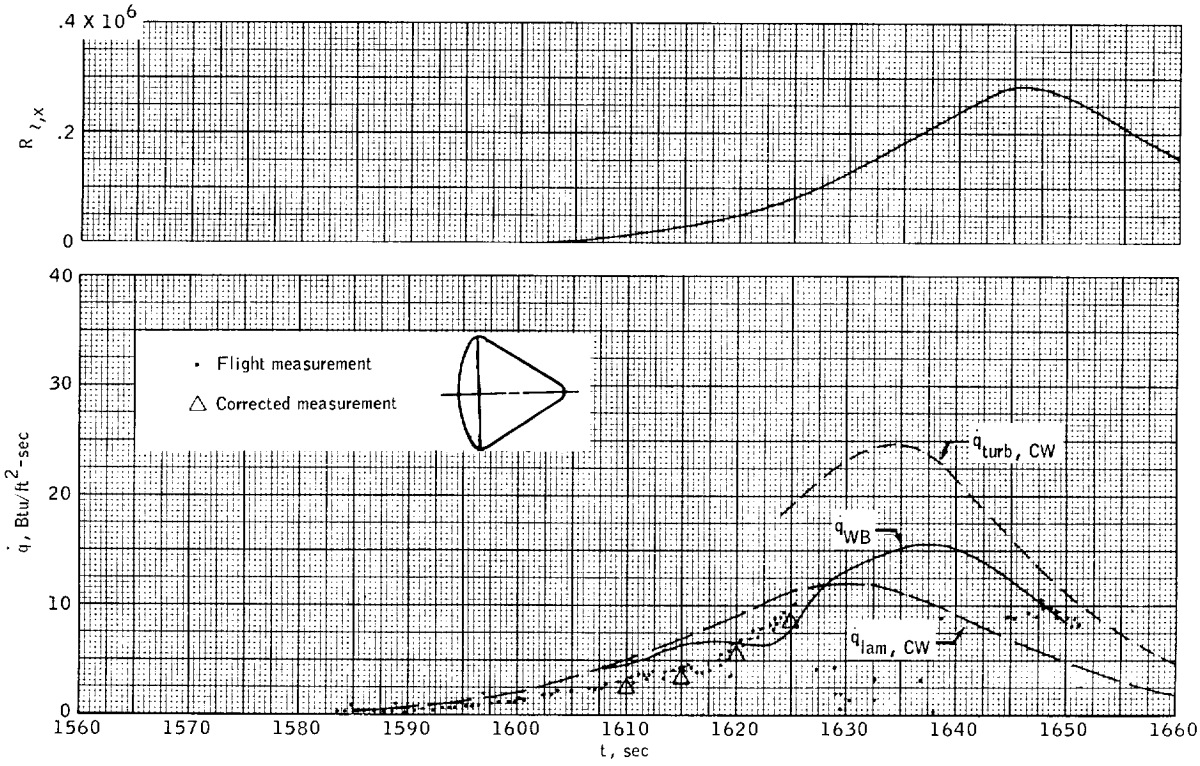

(h) $X_c = 19.4$, $\theta = 270°$, $S/R = 1.071$.

Figure 16. - Continued.

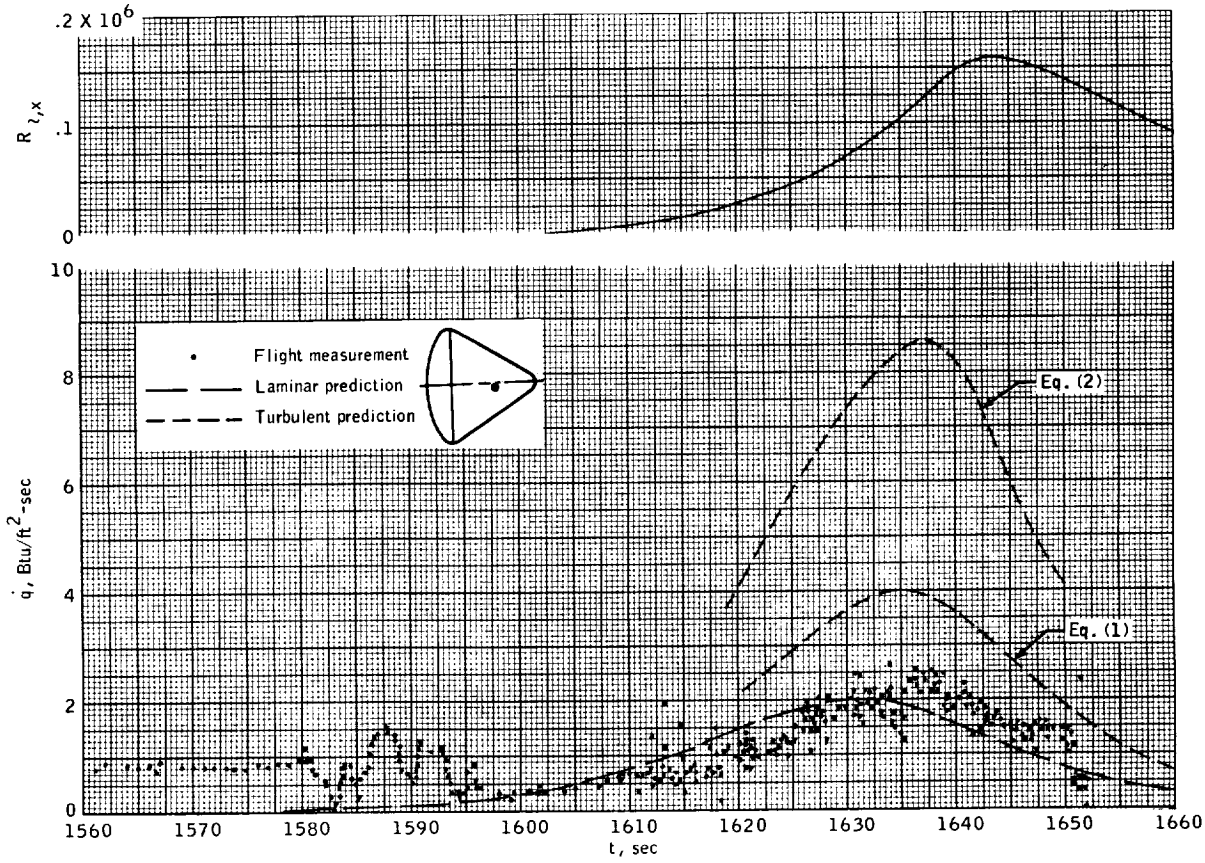

(i) $X_c = 88$, $\phi = 182.9°$, $S/R = 2.135$.

Figure 16. - Continued.

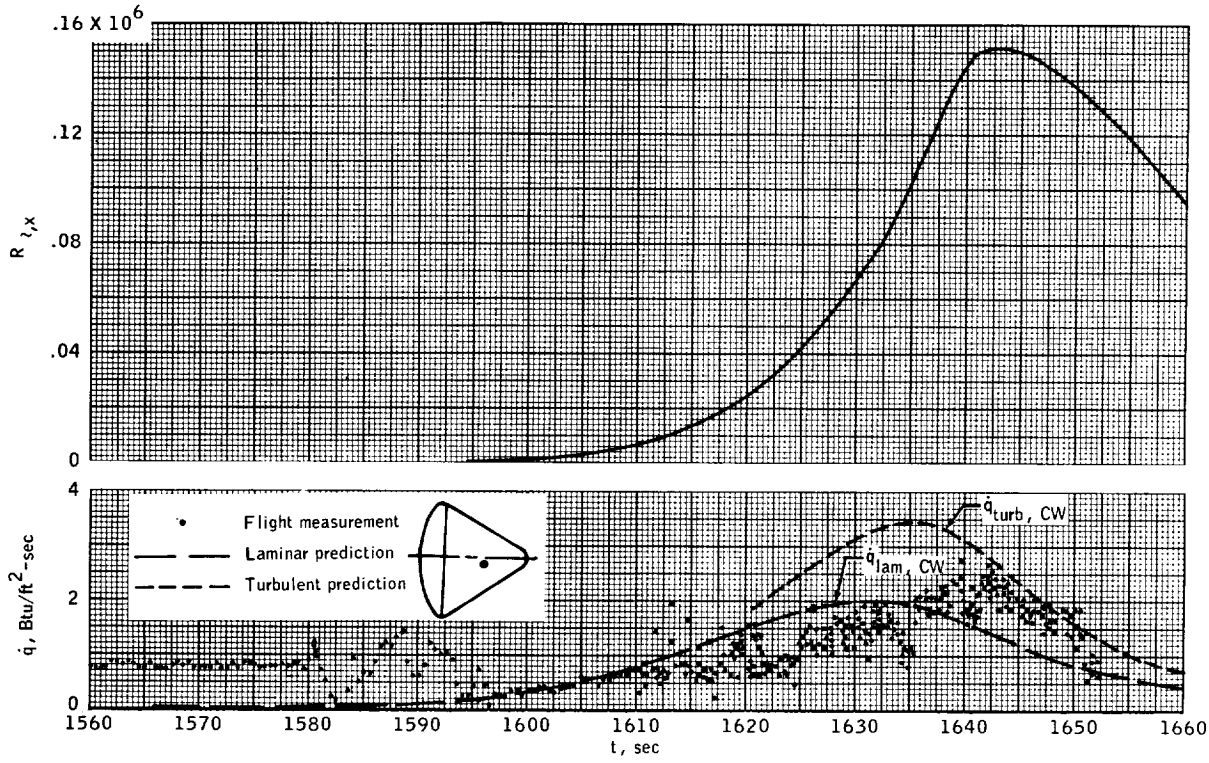

(j) $X_c = 78.9$, $\theta = 191.3°$, $S/R = 1.97$.

Figure 16. - Continued.

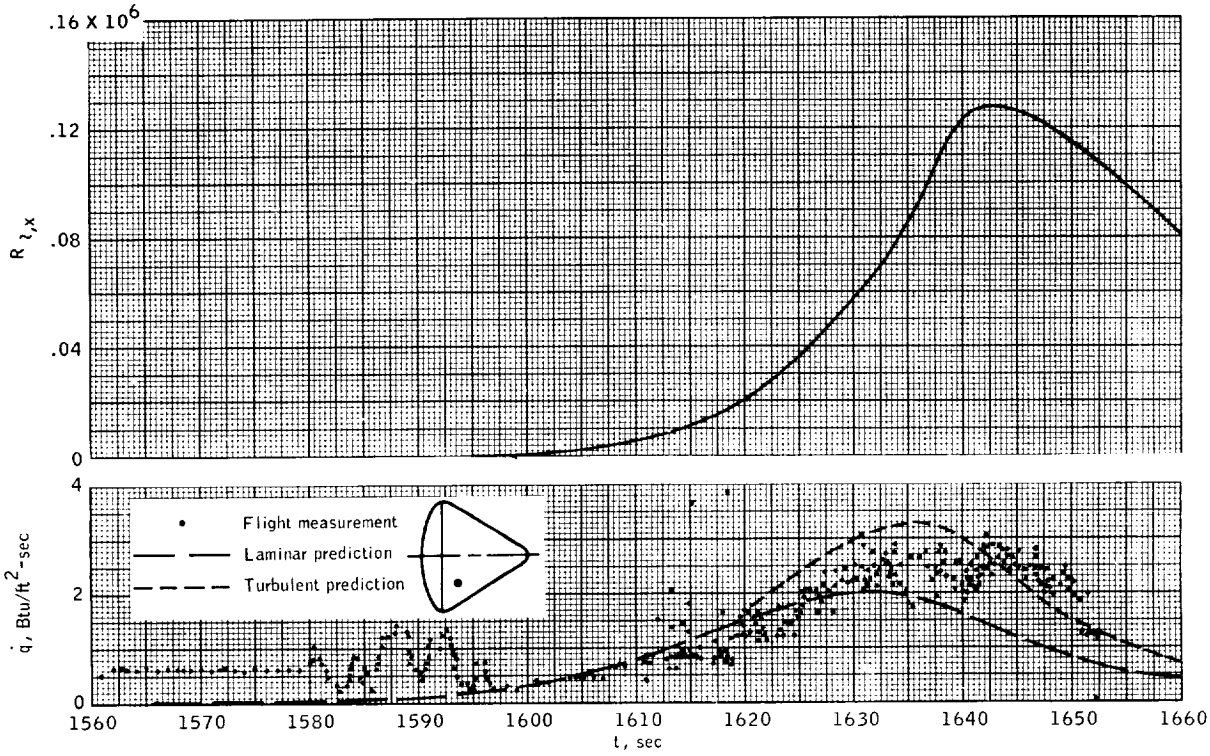

(k) $X_c = 40$, $\theta = 215.3°$, $S/R = 1.39$.

Figure 16. - Continued.

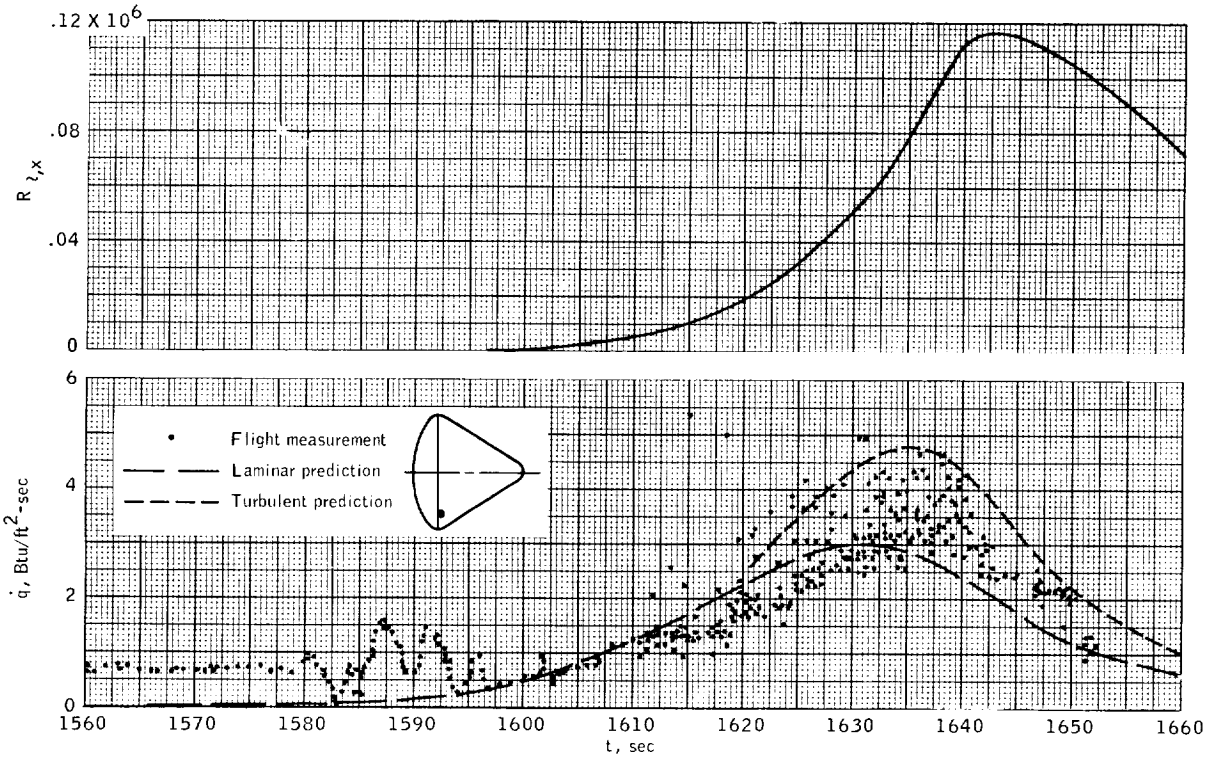

(l) $X_c = 25.3$, $\theta = 225.5°$, $S/R = 1.16$.

Figure 16. - Continued.

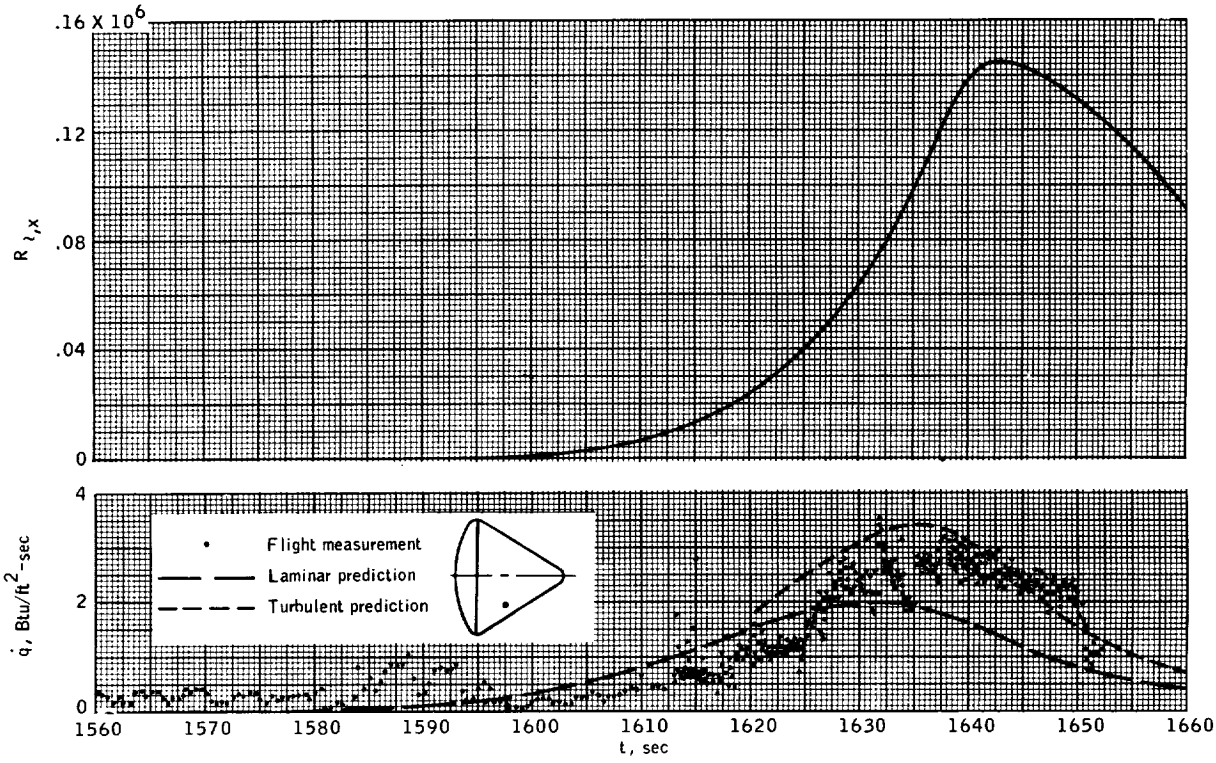

(m) $X_c = 51.7$, $\varphi = 229.8°$, $S/R = 1.57$.

Figure 16. - Continued.

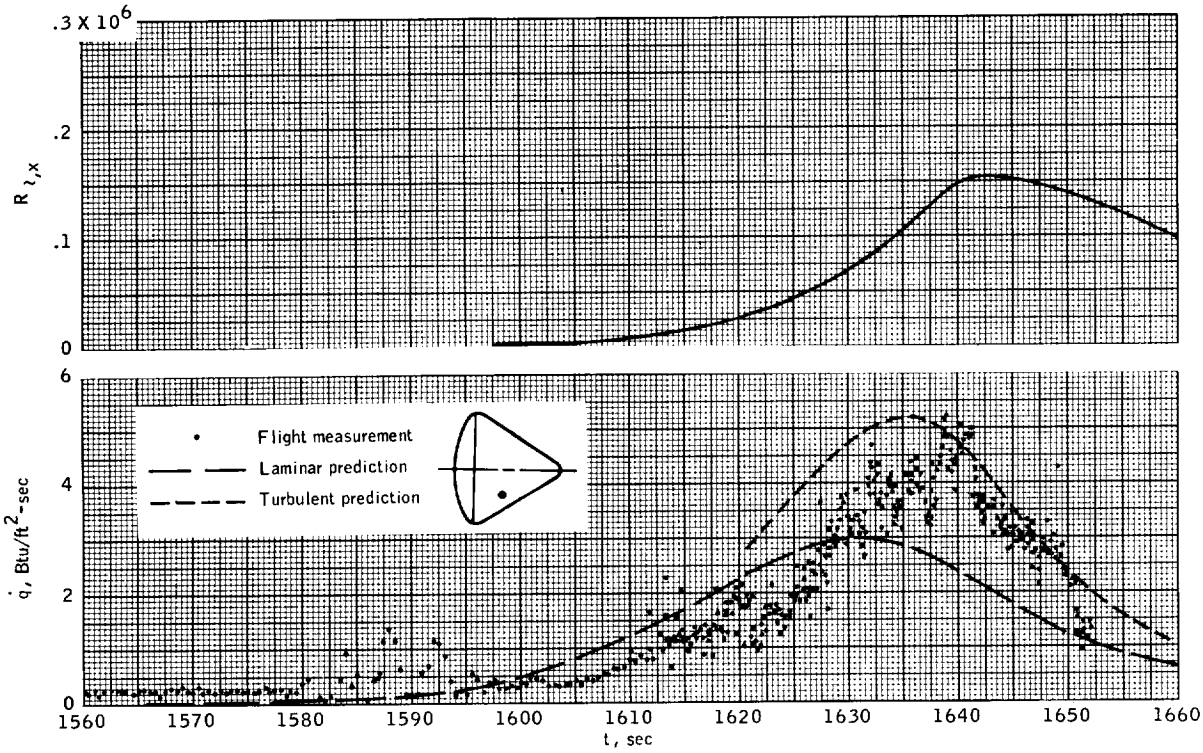

(n) $X_c = 58, \quad \theta = 234°, \quad S/R = 1.67.$

Figure 16. - Continued.

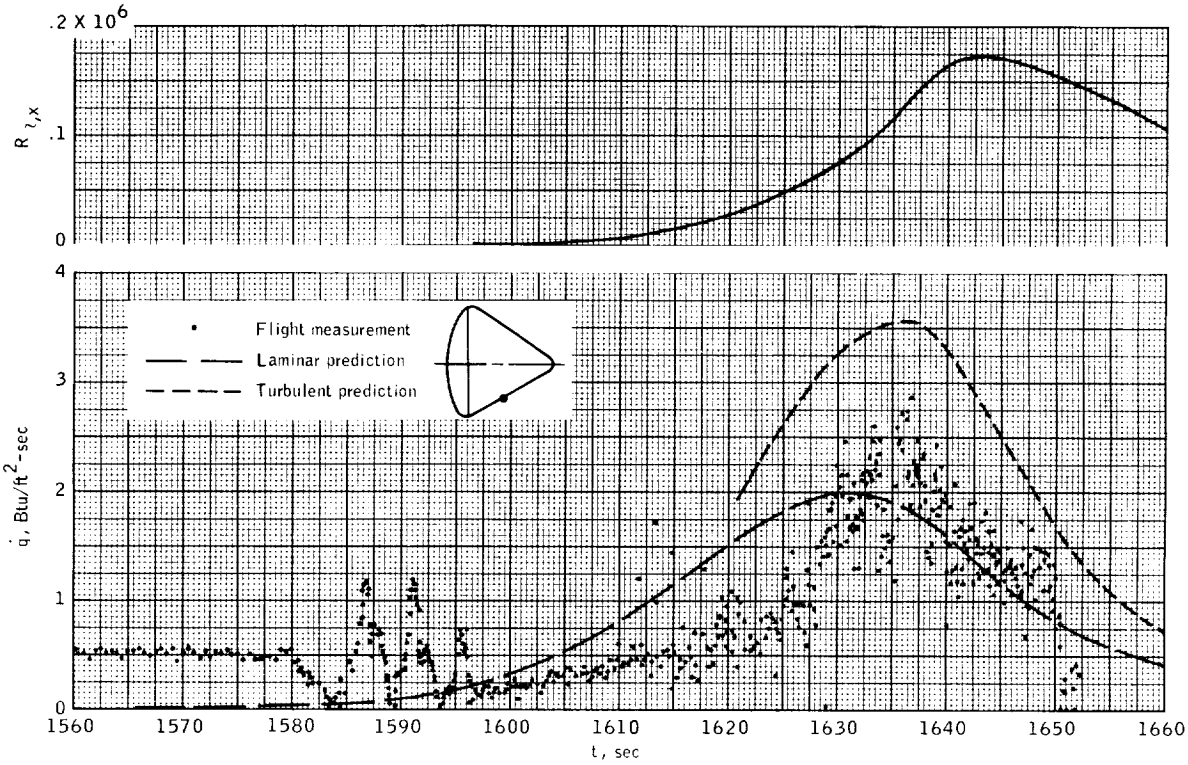

(o) $X_c = 70.5$, $\varphi = 276.4°$, $S/R = 1.865$.

Figure 16. - Continued.

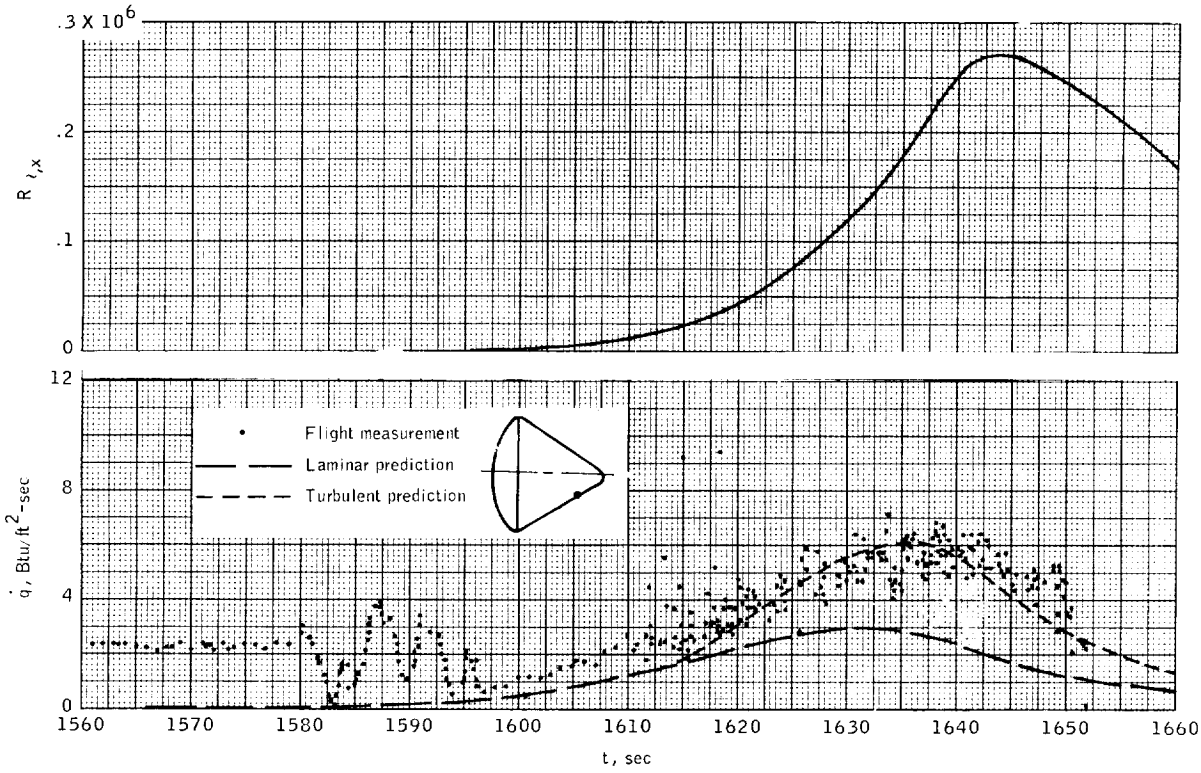

(p) $X_c = 114$, $\phi = 265°$, $S/R = 2.5$.

Figure 16. - Concluded.

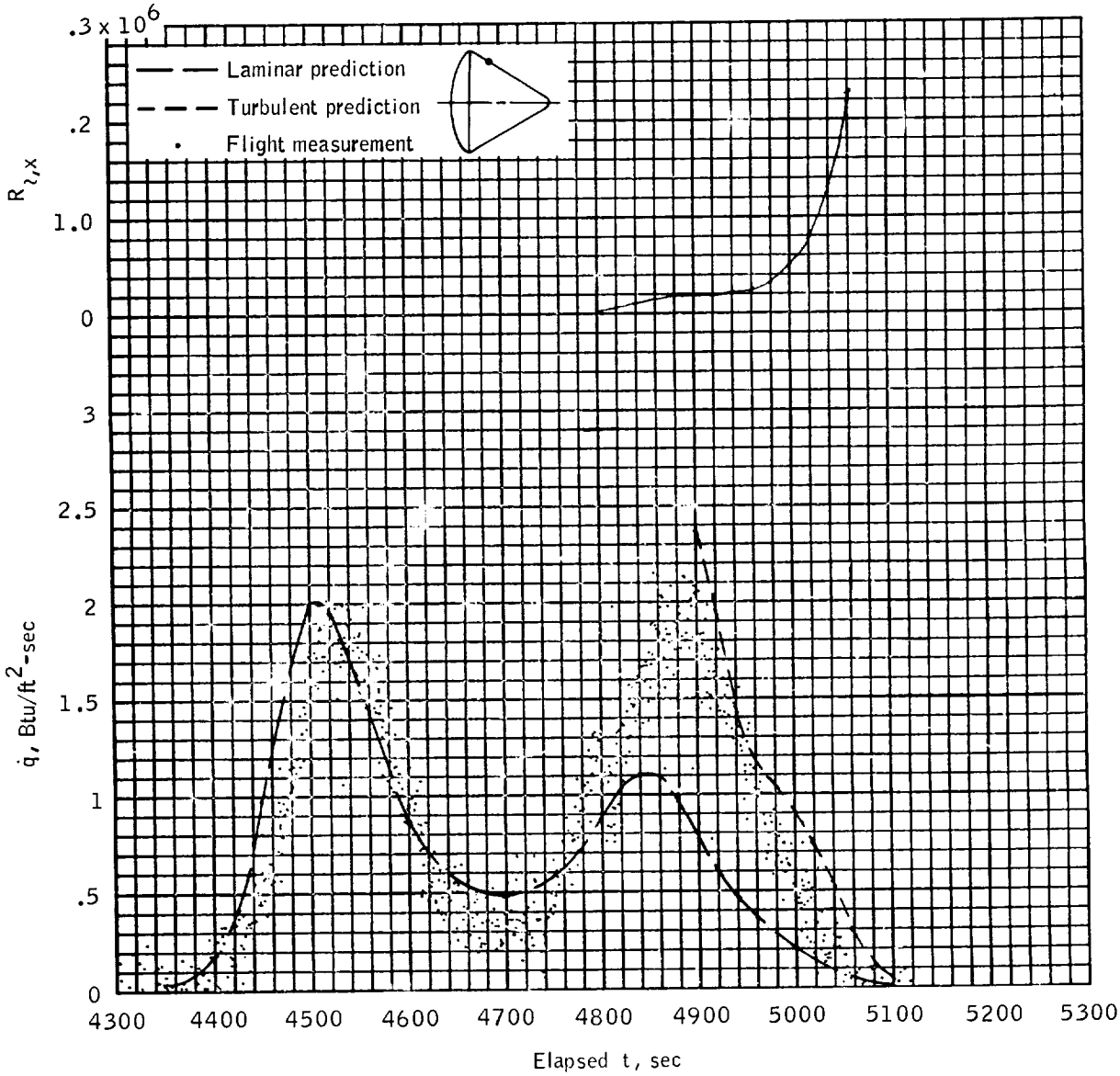

(a) $X_c = 45.5$, $\theta = 85.3°$, $S/R = 1.475$.

Figure 17. - Histories of local Reynolds number and heating rates on conical section of spacecraft 011.

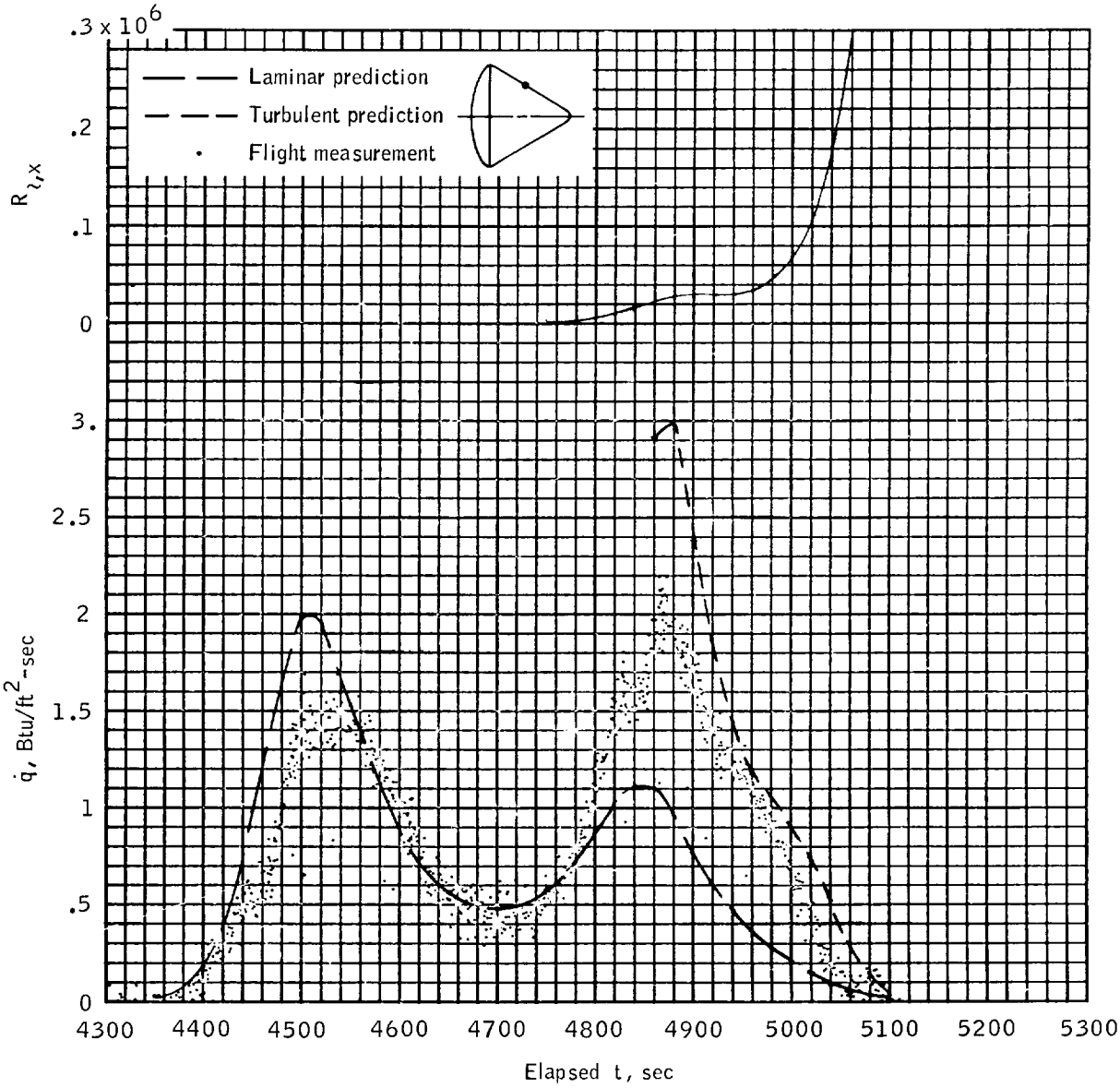

(b) $X_c = 64.8$, $\theta = 92°$, $S/R = 1.775$.

Figure 17. - Continued.

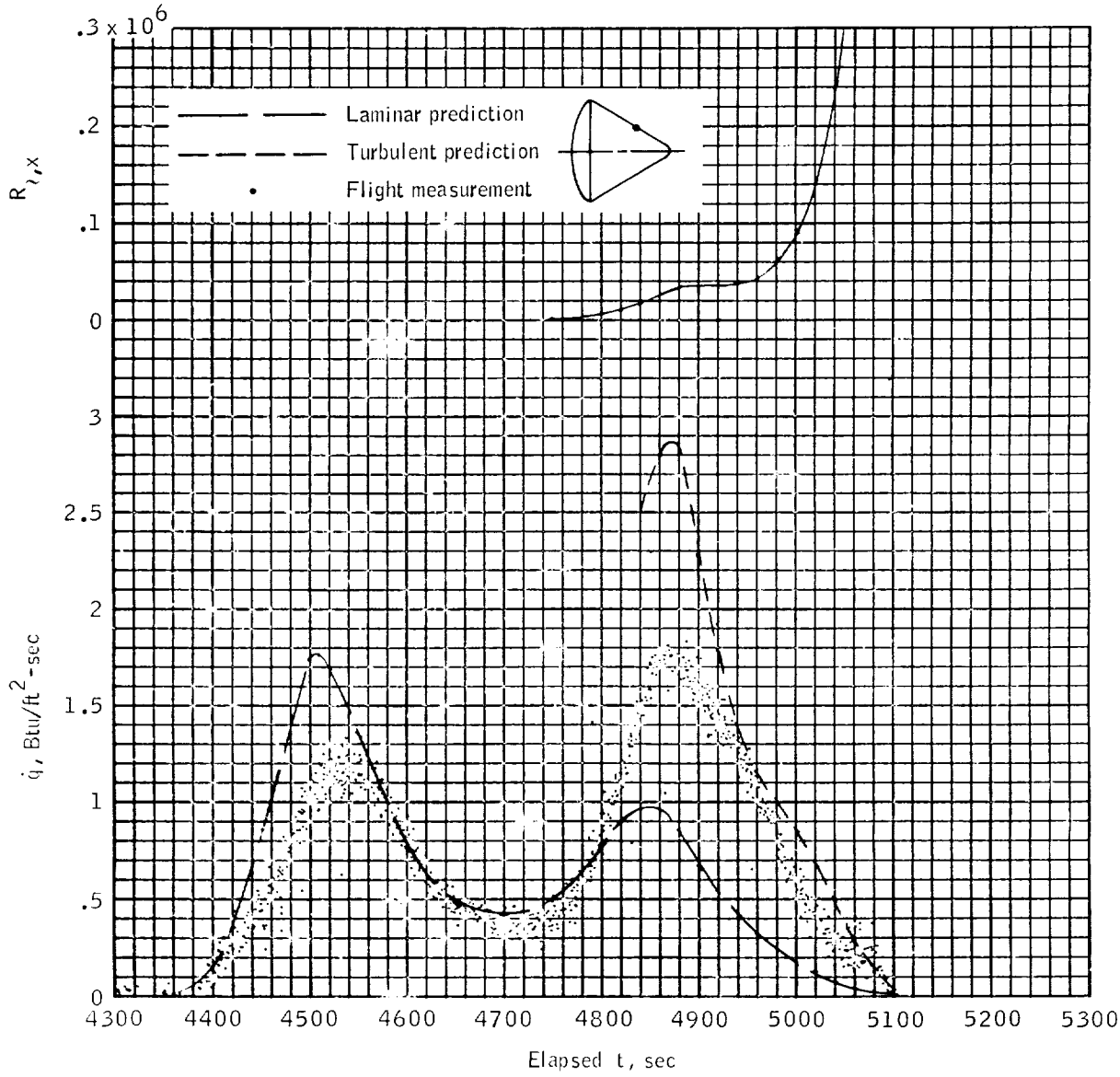

(c) $X_c = 78.9$, $\theta = 115°$, $S/R = 1.99$.

Figure 17. - Continued.

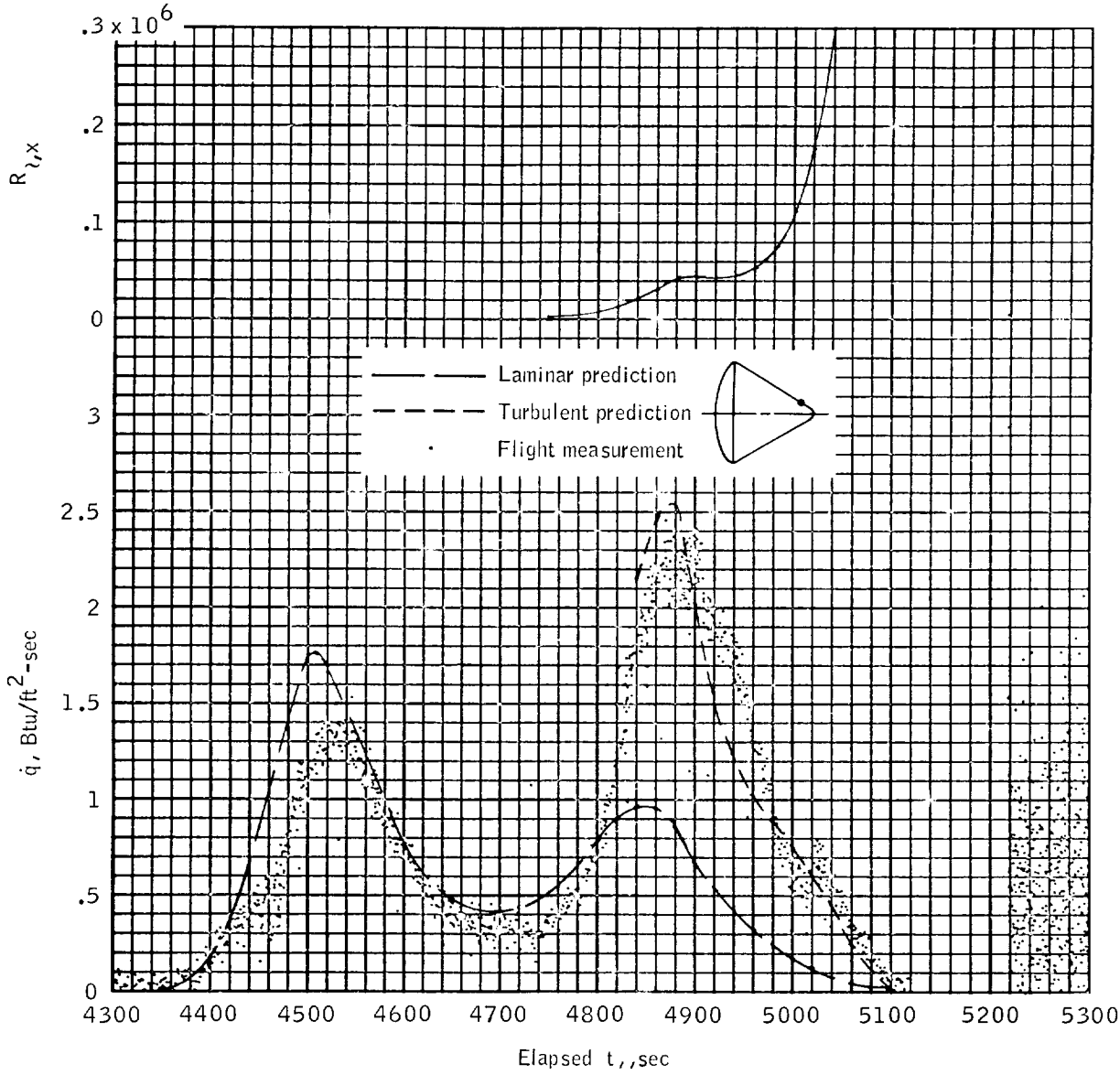

(d) $X_c = 114$, $\theta = 83.4°$, $S/R = 2.5$.

Figure 17. - Continued.

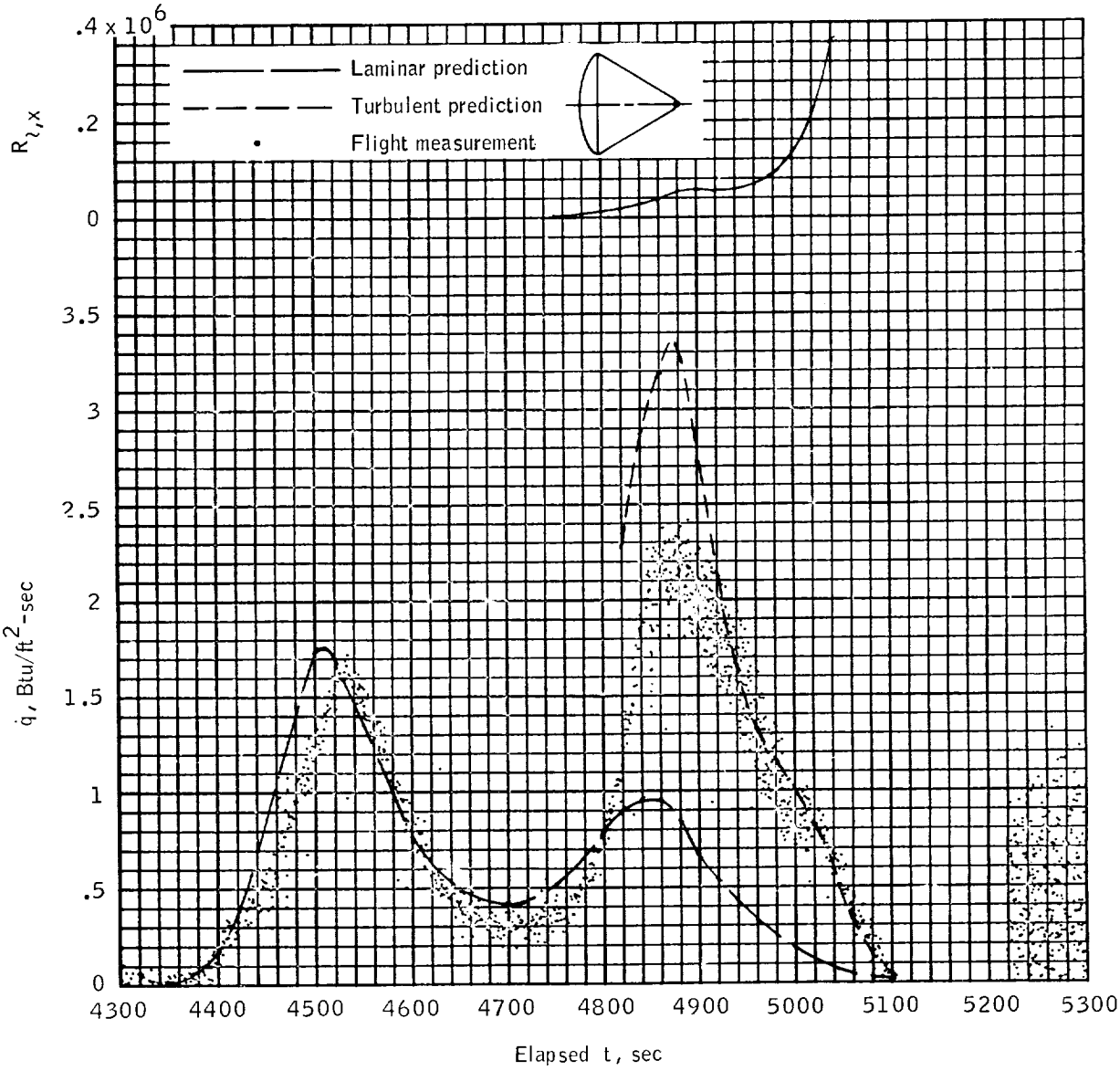

(e) Apex.

Figure 17. - Continued.

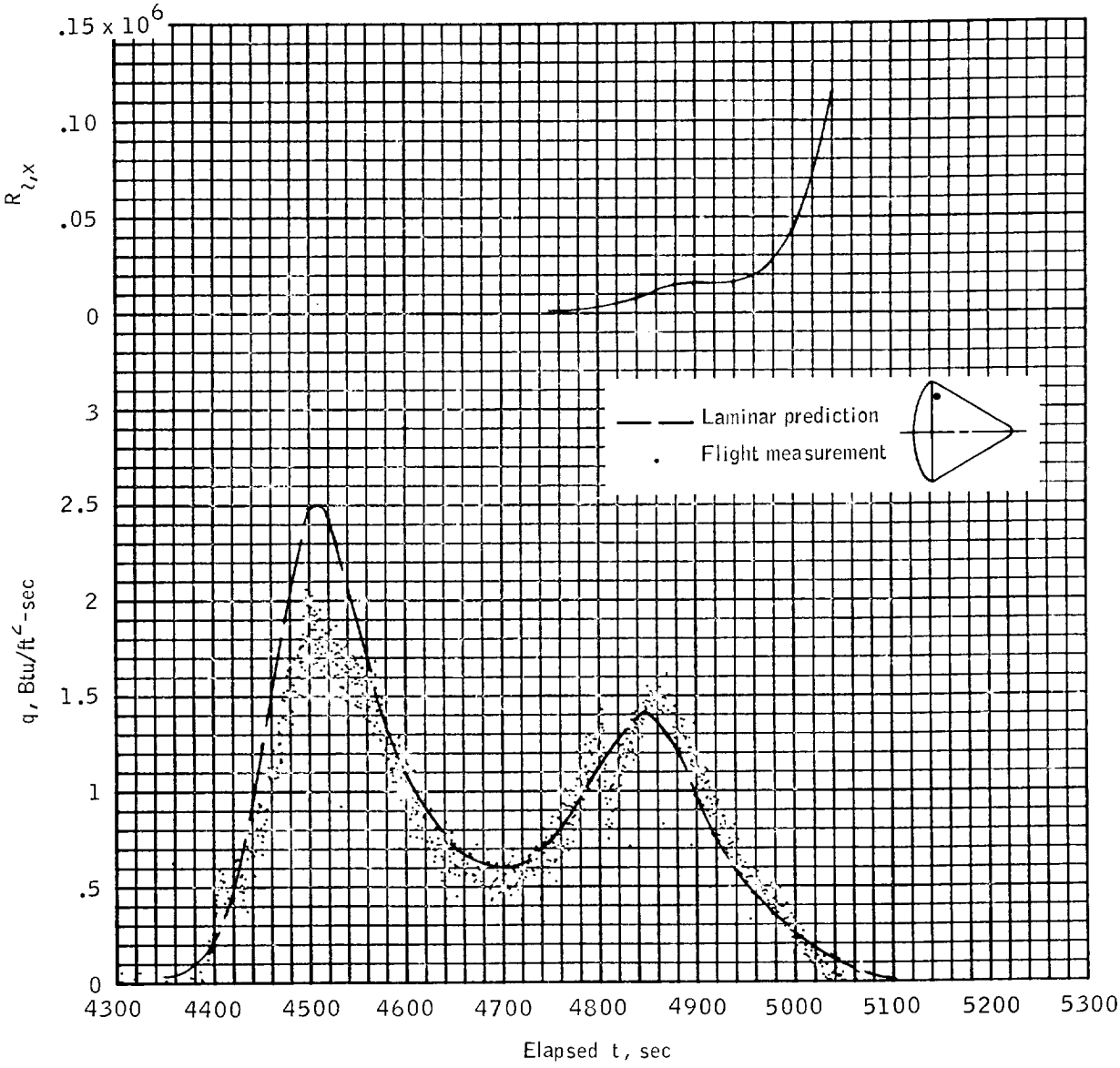

(f) $X_c = 25.3$, $\theta = 138°$, $S/R = 1.16$.

Figure 17. - Continued.

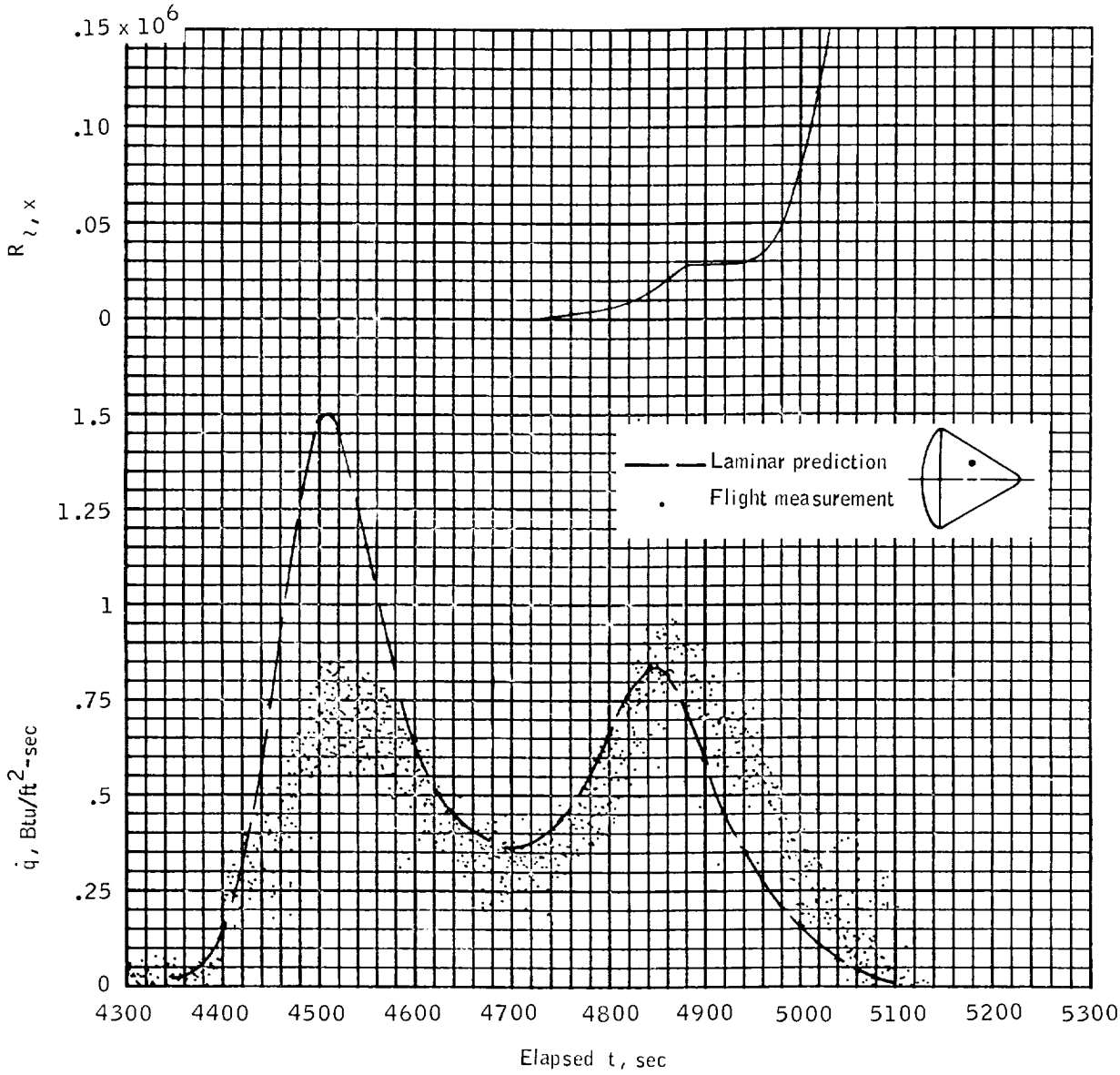

(g) $X_c = 61.5$, $\theta = 142.8°$, $S/R = 1.723$.

Figure 17. - Continued.

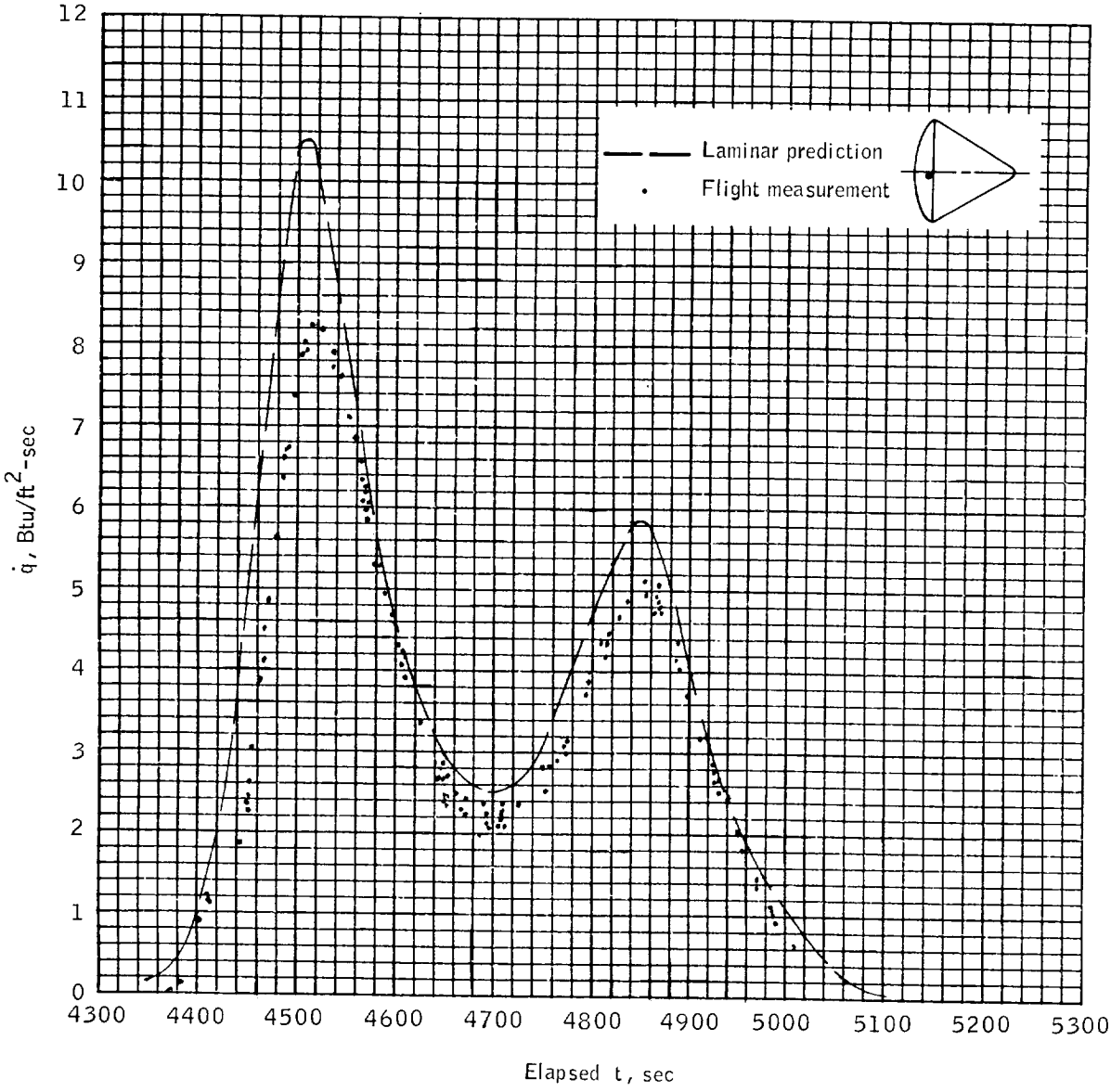

(h) $X_c = 19.4$, $\theta = 178.5°$, $S/R = 1.071$.

Figure 17. - Continued.

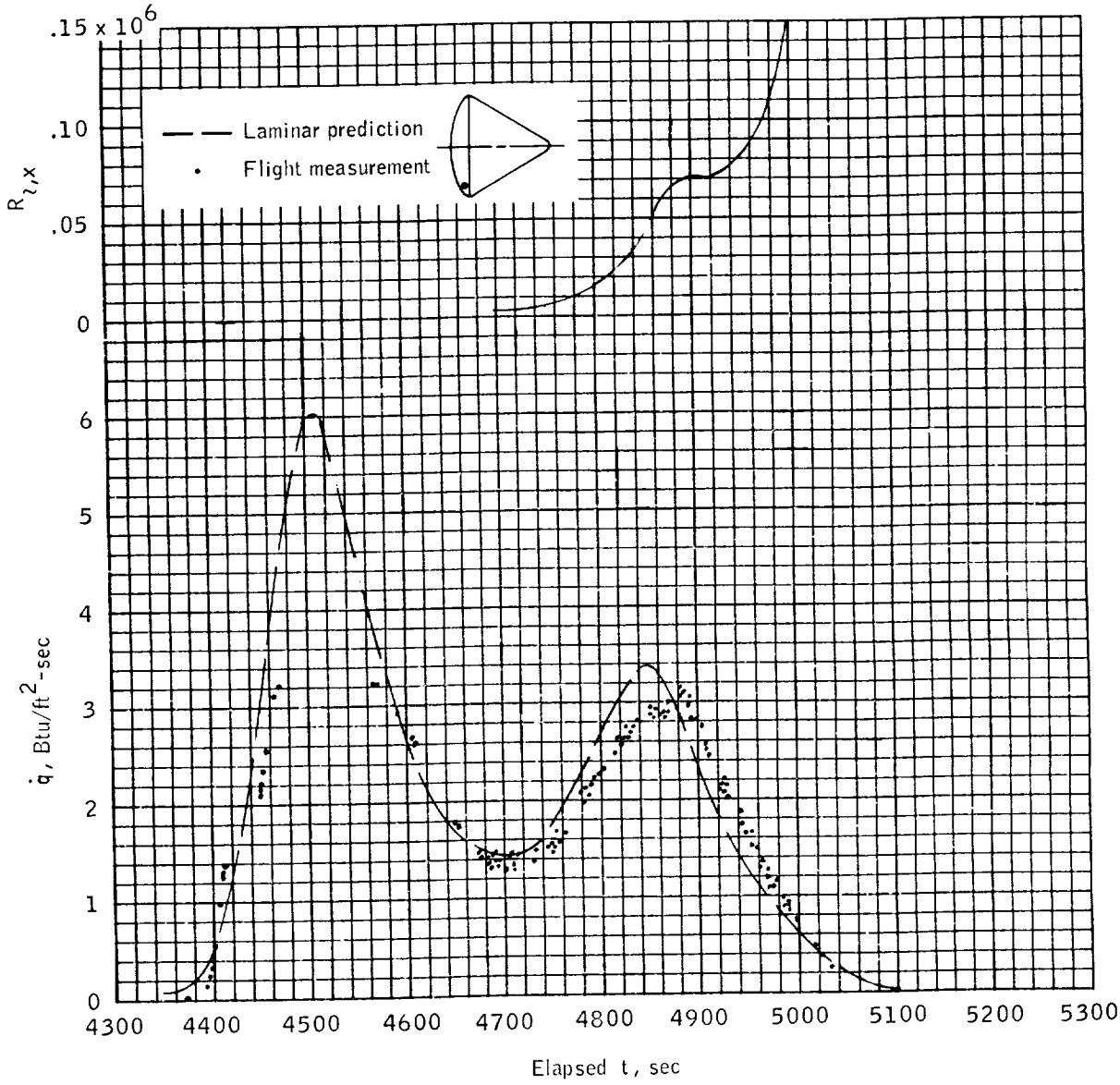

(i) $X_c = 19.4$, $\theta = 270°$, $S/R = 1.071$.

Figure 17. - Continued.

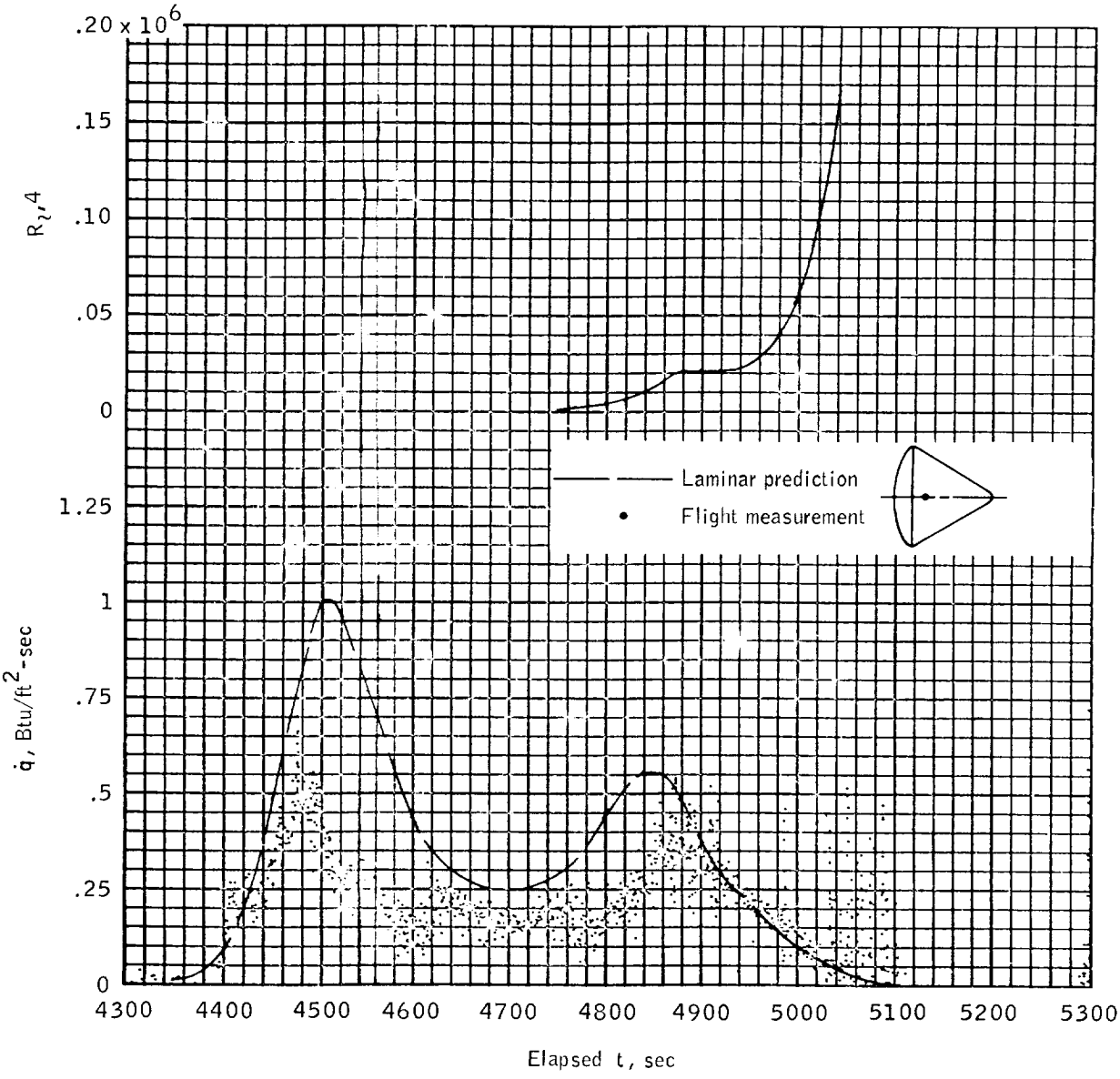

(j) $X_c = 35$, $\theta = 178.6°$, $S/R = 1.31$.

Figure 17. - Continued.

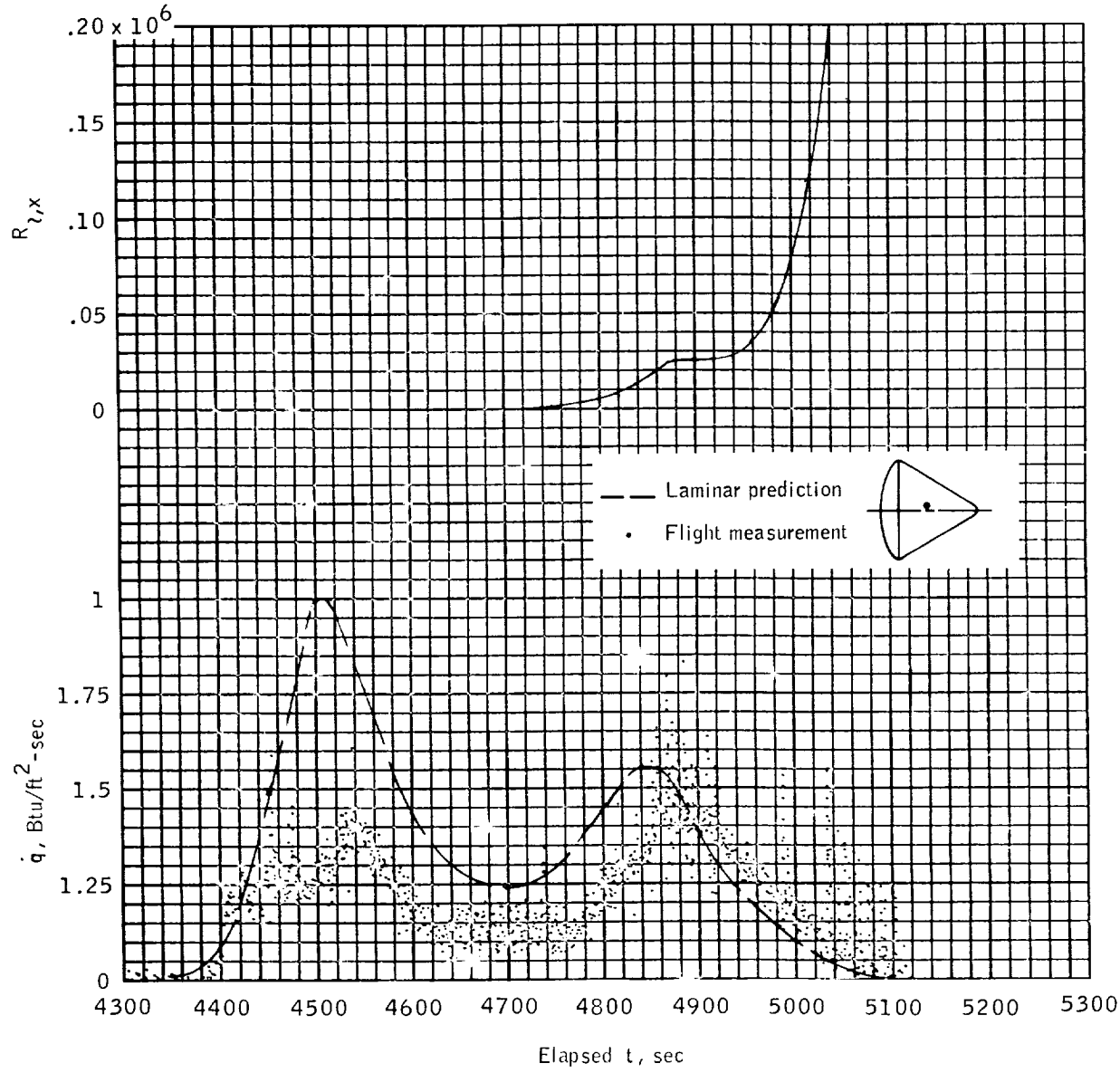

(k) $X_c = 60$, $\theta = 177.5°$, $S/R = 1.696$.

Figure 17. - Continued.

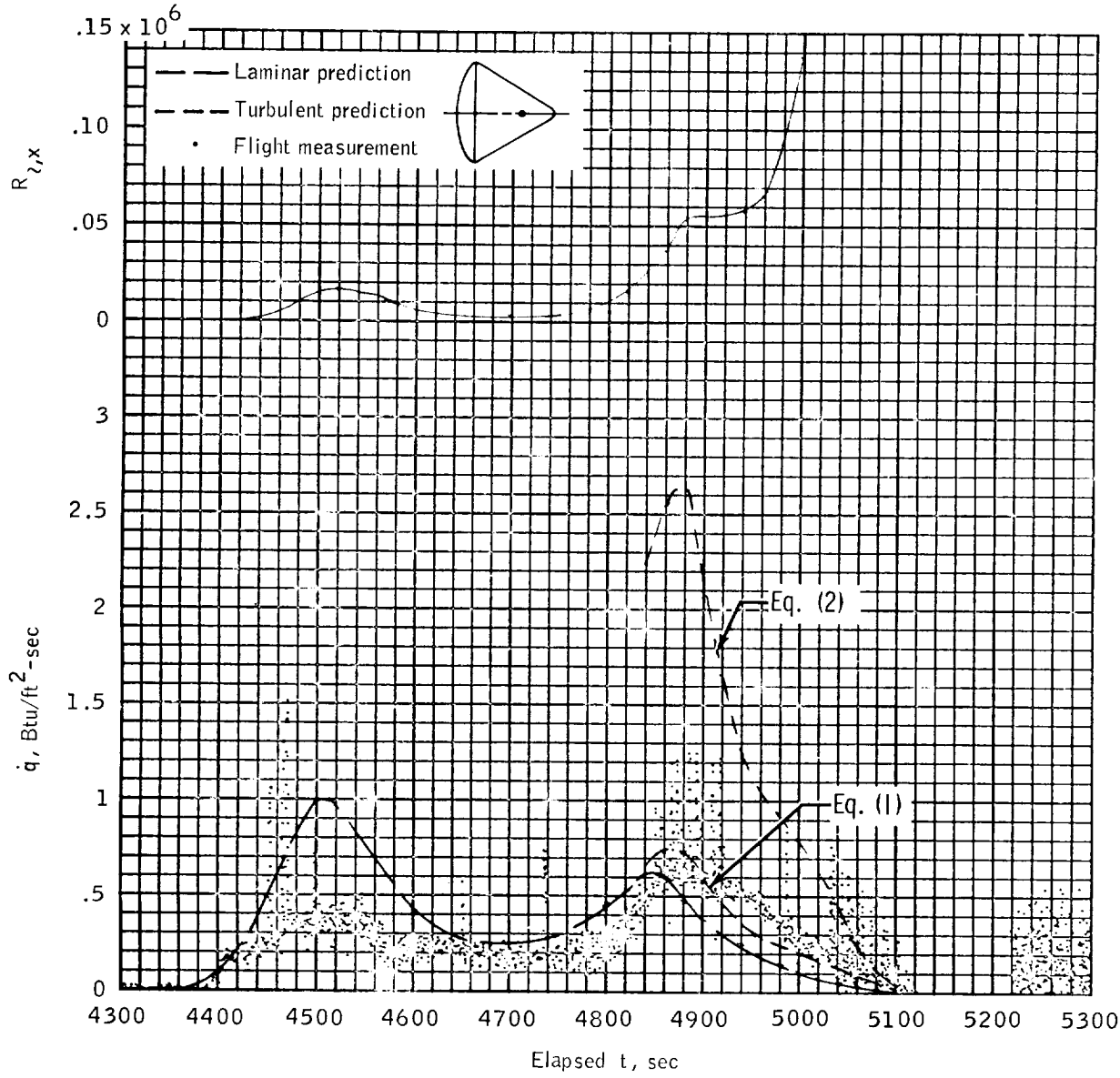

(l) $X_c = 88$, $\theta = 182.9°$, $S/R = 2.135$.

Figure 17. - Continued.

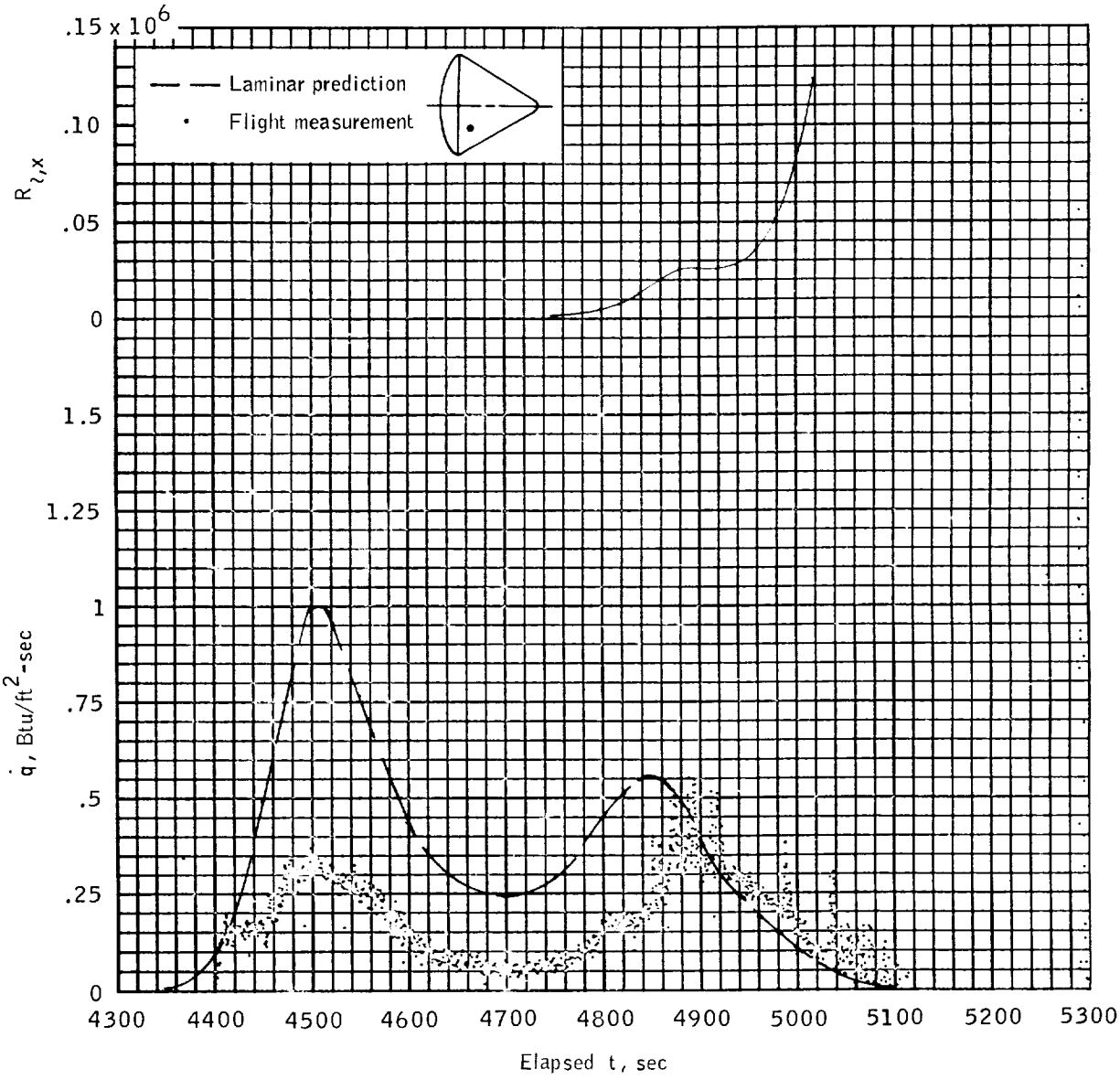

(m) $X_c = 40$, $\theta = 215.3°$, $S/R = 1.39$.

Figure 17. - Continued.

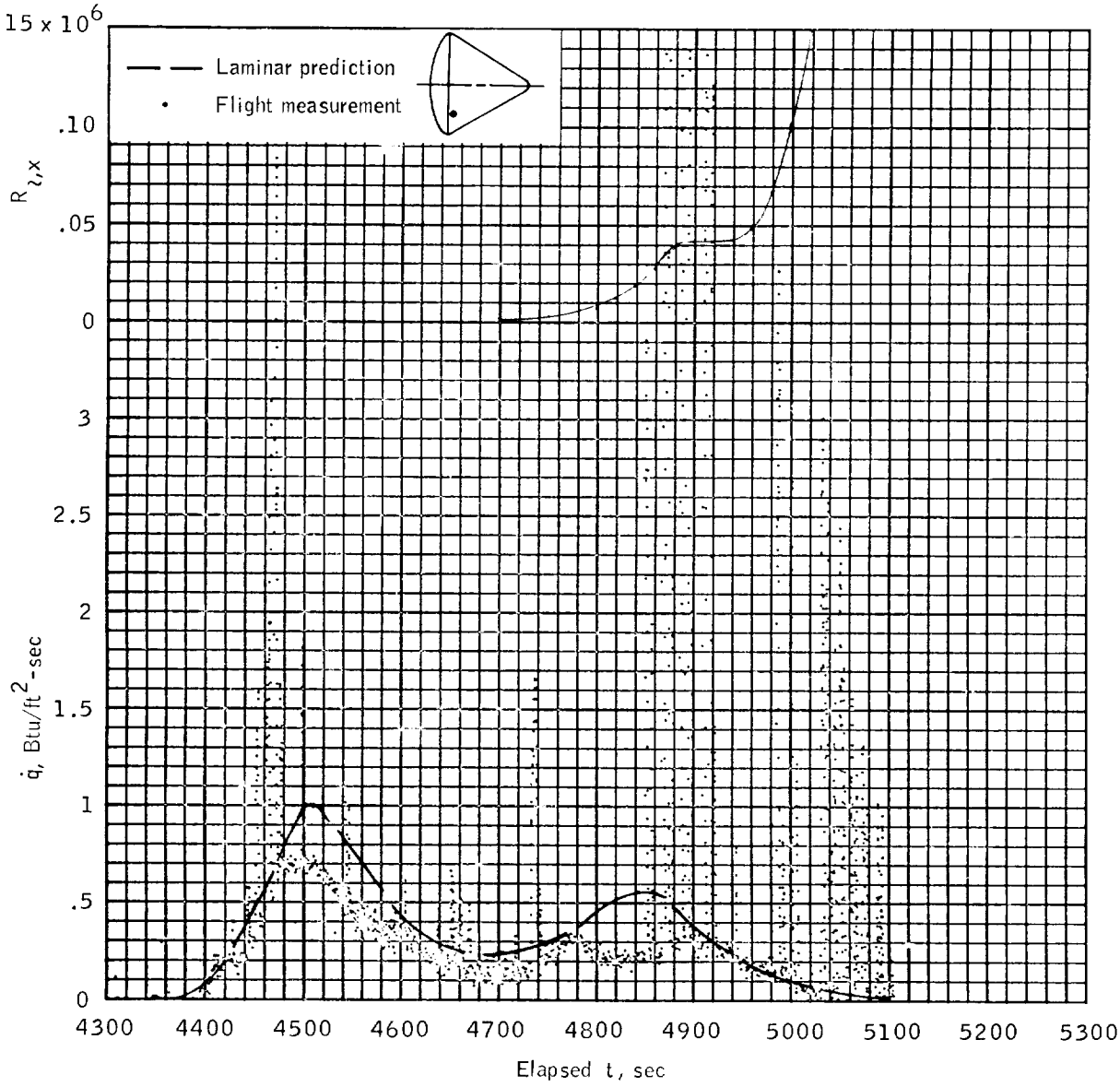

(n) $X_c = 25.3$, $\phi = 225.5°$, $S/R = 1.16$.

Figure 17. - Continued.

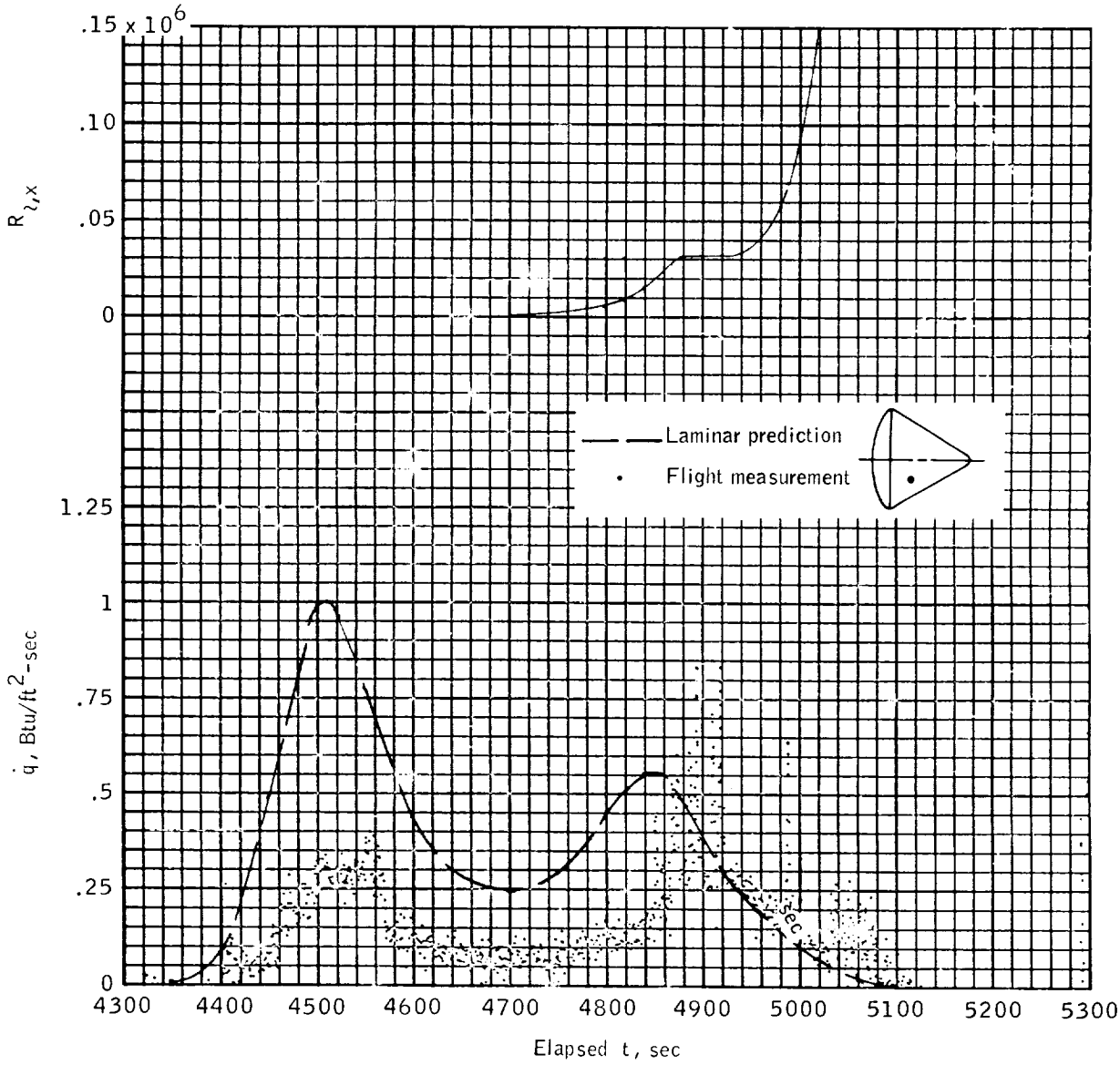

(o) $X_c = 51.7$, $\theta = 229.8°$, S/R = 1.57.

Figure 17. - Continued.

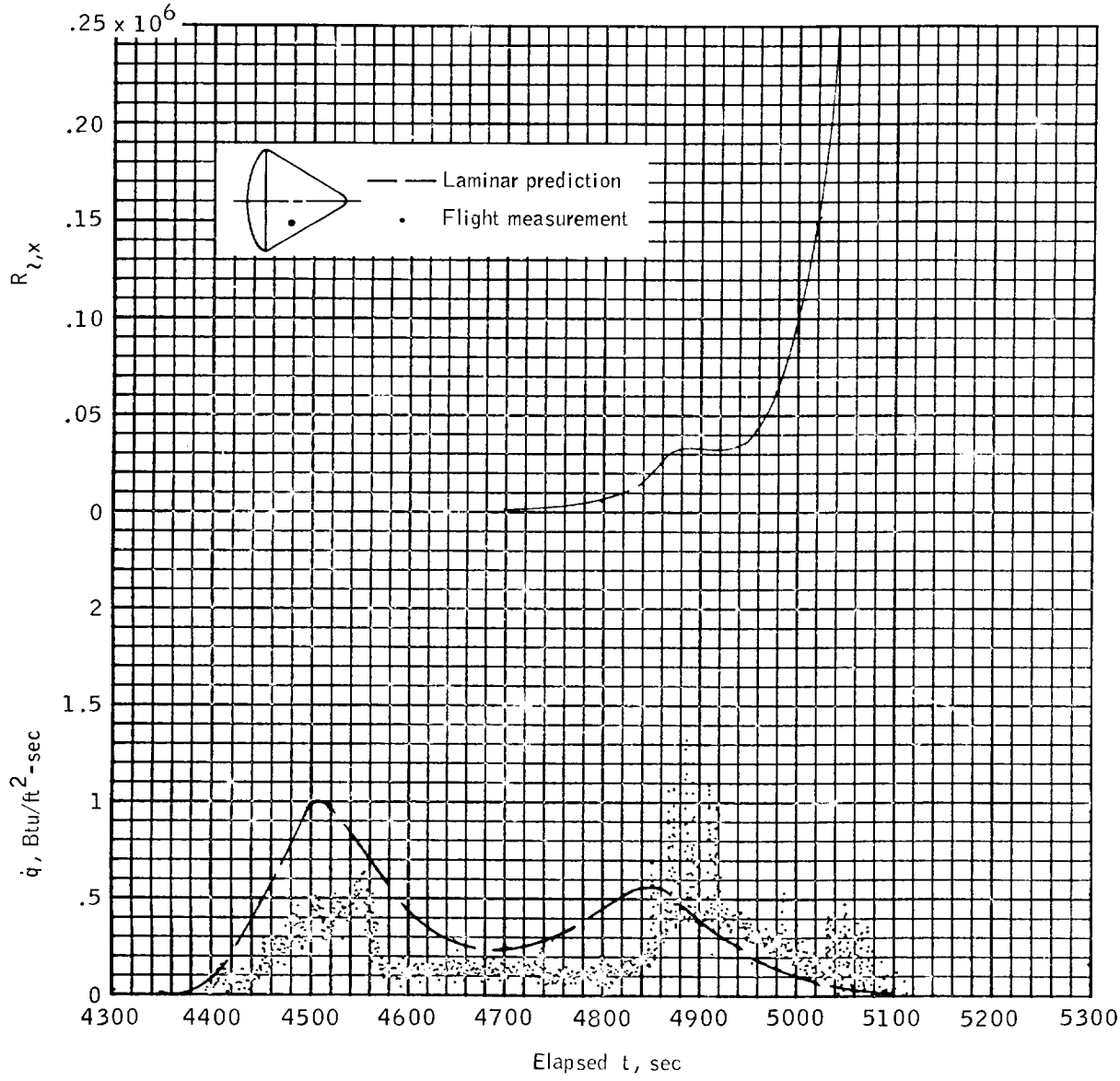

(p) $X_c = 58$, $\theta = 234°$, $S/R = 1.67$.

Figure 17. - Continued.

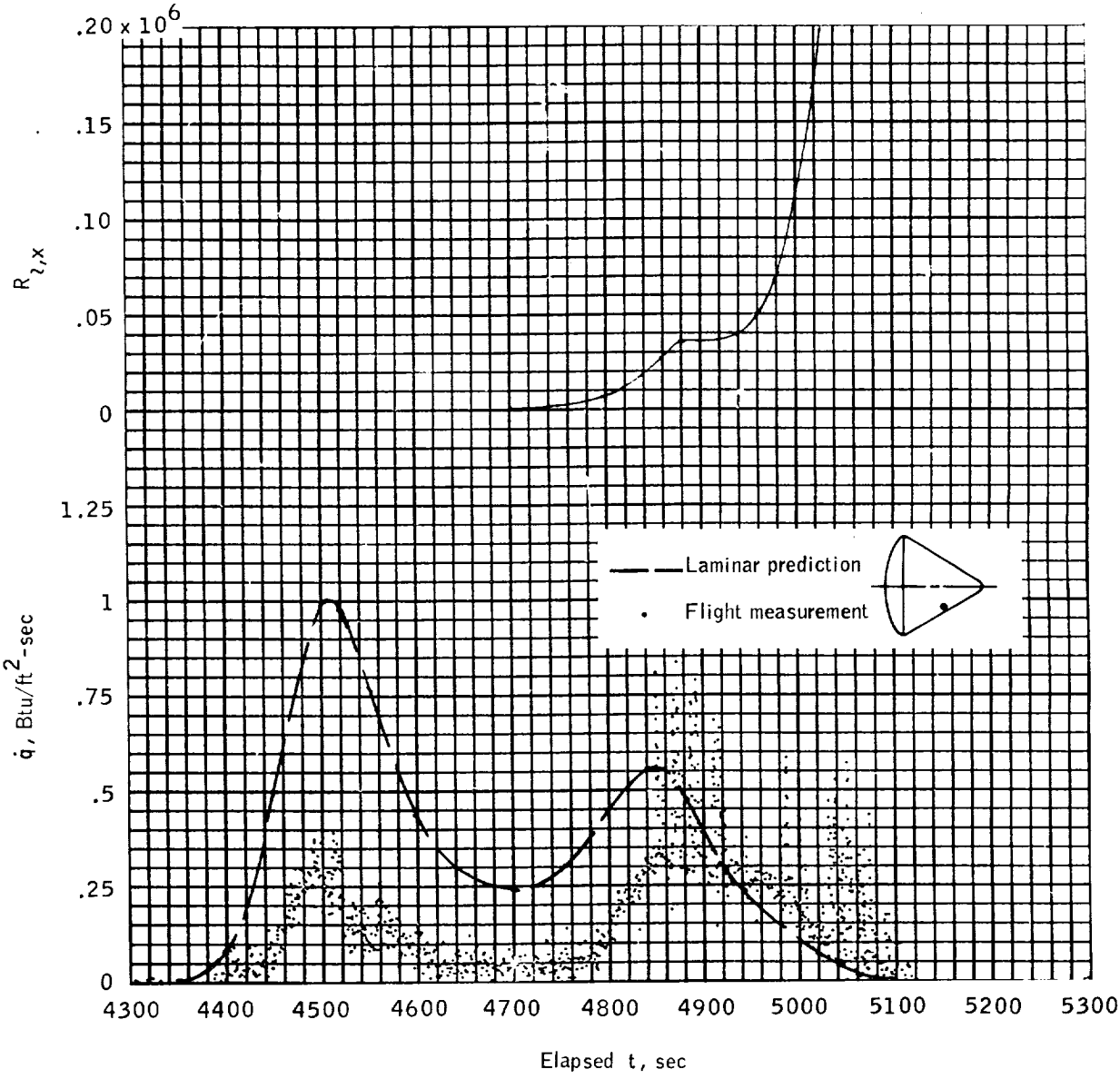

(q) $X_c = 70.5$, $\phi = 276.4°$, $S/R = 1.865$.

Figure 17. - Continued.

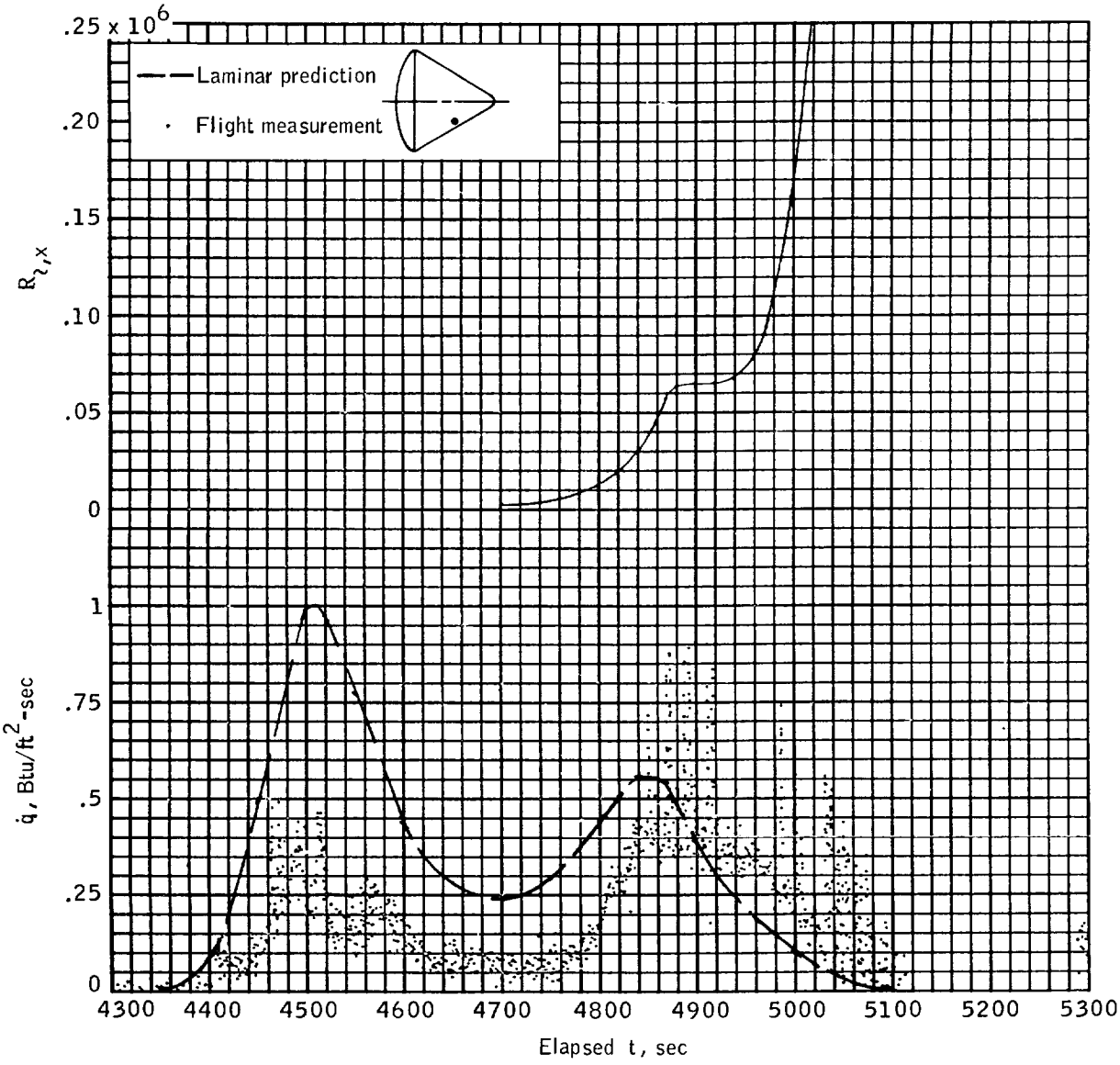

(r) $X_c = 78.9$, $\theta = 267.8°$, $S/R = 1.99$.

Figure 17. - Continued.

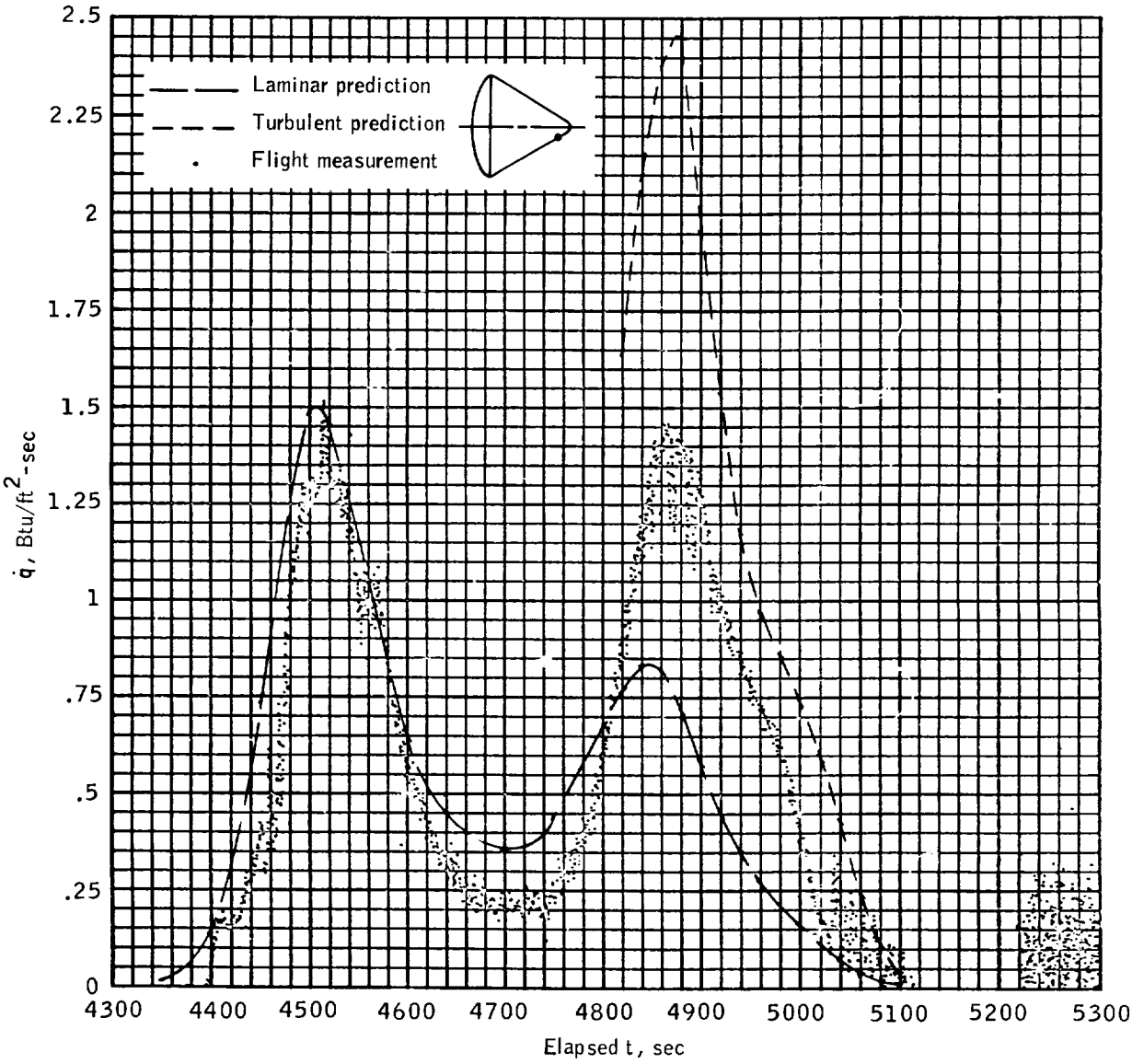

(s) $X_c = 114$, $\theta = 265°$, $S/R = 2.5$.

Figure 17. - Concluded.

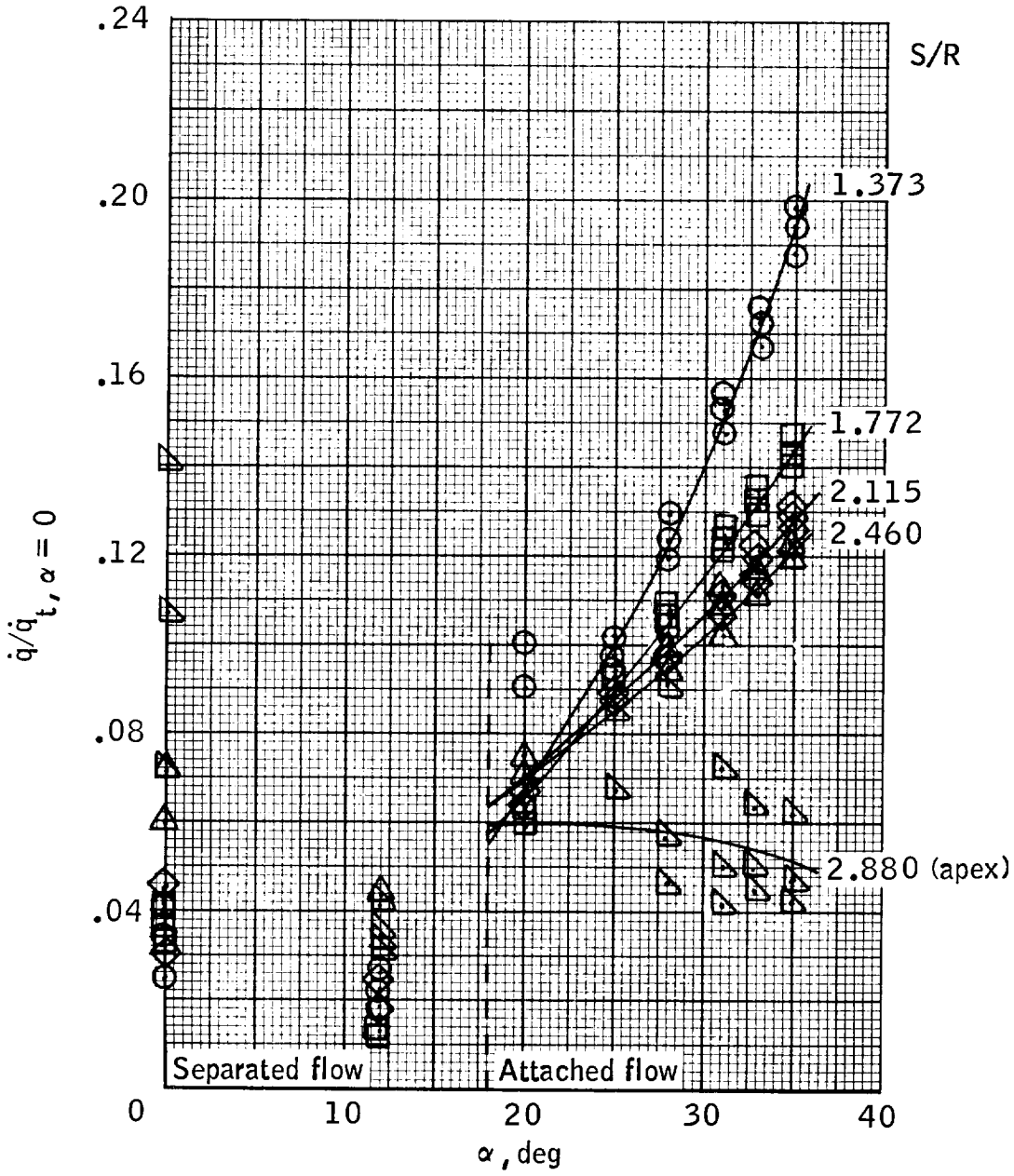

Figure 18. - Wind-tunnel heating rate measurements on windward conical section (θ = 90°) at Mach numbers from 7.42 to 10.18.

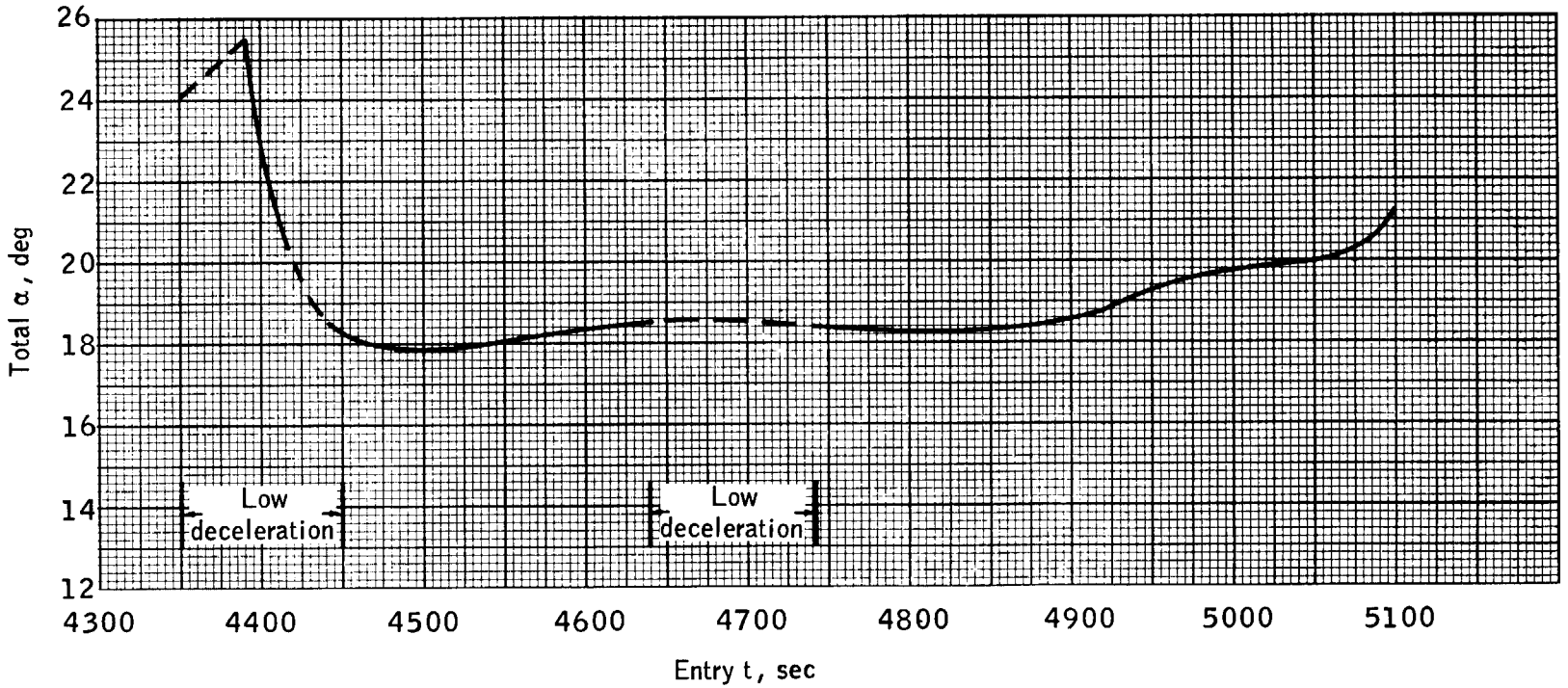

Figure 19. - History of total angle of attack measured during entry of spacecraft 011.

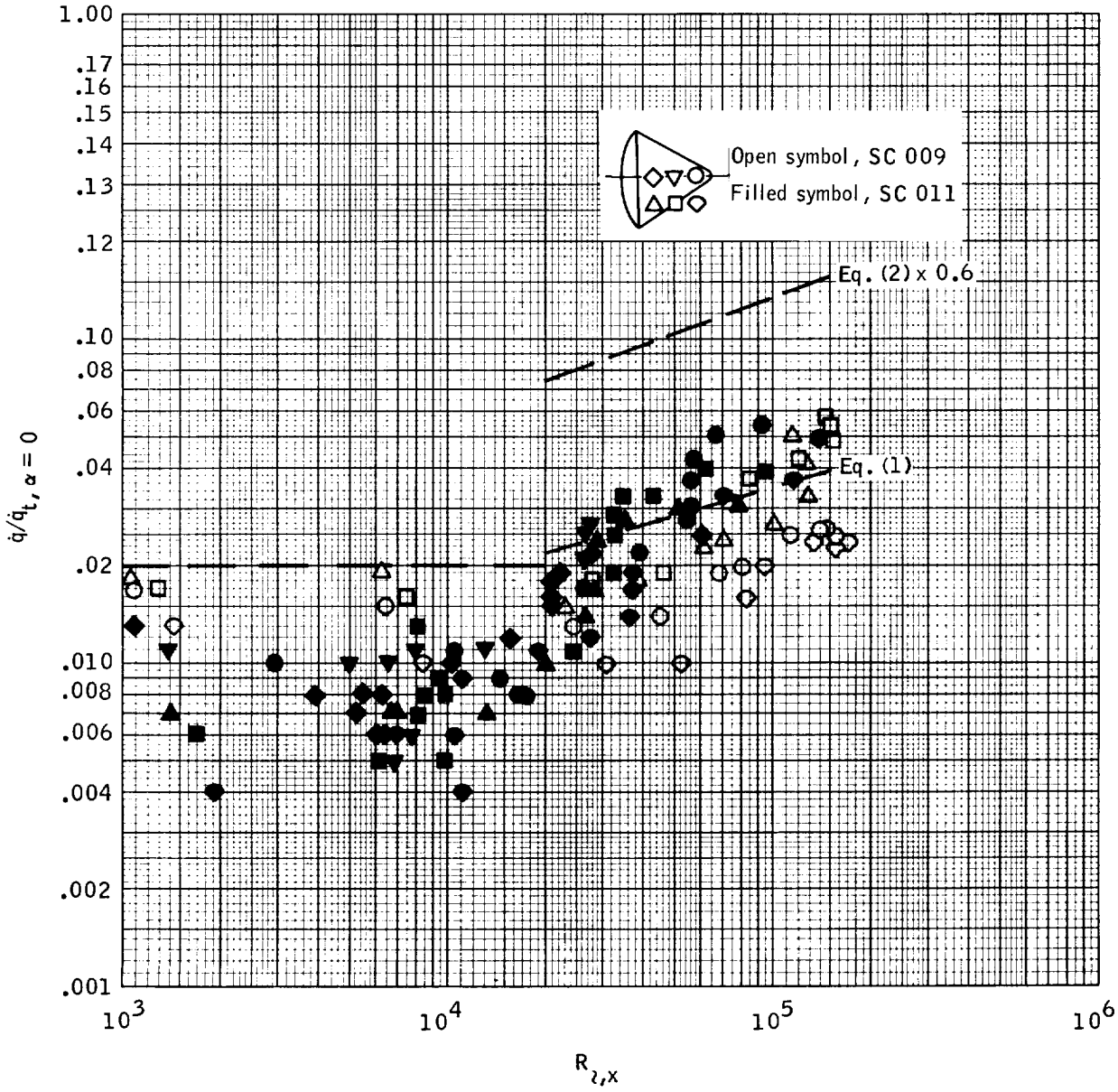

Figure 20. - Leeward heating as a function of local Reynolds number.